UNIVERSITY OF CALIFORNIA,
IRVINE

Synthesis and Characterization of Pyrite Thin Films and Single Crystals for PV Devices and Fundamental Studies

DISSERTATION

submitted in partial satisfaction of the requirements
for the degree of

DOCTOR OF PHILOSOPHY

in Materials Science and Engineering

by

Nima Farhi

Dissertation Committee:
Professor Matthew Law, Chair
Professor Allon Hochbaum
Professor Alon Gorodetsky

2016

DEDICATION

I want to dedicate this work to my parents (Niloufar Mirjalili and Fereydoon Farhi) and my sister (Nahal Farhi). Unfortunately, my dad passed away during the course of my graduate studies, but none of this would have been possible without his unconditional love and support.

TABLE OF CONTENTS

LIST OF FIGURES

LIST OF TABLES

ACKNOWLEDGMENTS

First I would like to thank Prof. Matt Law for letting me work in his lab, and guiding me during my graduate studies. He is a great scientist and taught me how to approach complicated problems systematically. I would like to acknowledge the financial support from the U.S. Department of Energy as well, which let our group work on the pyrite project (Contract No. DE-EE0005324, funded by the SunShot Next Generation Photovoltaics II (NextGenPVII) program).

Throughout these years I had the opportunity to work alongside great graduate students. I would like to thank all of them. They welcomed me with open arms and were available whenever I needed anything. I worked closely with Moritz Limpinsel, Trenton Salk, and Amanda Weber on the pyrite project and owe a special thank you to them. I owe a special thank you to Nick Berry and Sean Seefeld as well. They both trained me as I joined the group before graduating and leaving UCI. In the past couple of months, I got to collaborate with Jeongwoo Kim at Prof. Wu's lab as well. I am thankful for his availability and knowledge.

I would like to acknowledge all the facilities at UCI with their supportive staffs. Dr. Lin and Dr. Zheng (LEXI) were always available whenever I had a question about the XRD and the SEM. I was also fortunate to have access to the ICP-MS at Prof. Johnson's lab. I owe a special thank you to her as well.

I want to acknowledge John Wiley and Sons, American Chemical Society, and The Royal Chemical Society for giving me permission to include copyrighted works in this dissertation as parts of the following sections: section 3.1, section 3.4, section 4.1, and chapter 2.

Lastly, I want to thank my family and great friends. They have been available for me during the ups and downs of life. I am thankful to have them in my life. I need to send a special thank you to my girlfriend, Heather Carr. Ironically my defense date is the same date that we met each other for the first time last year; I am fortunate to have her alongside of me.

CURRICULUM VITAE

Nima Farhi

Education

Ph.D. in Materials Science and Engineering **2016**
University of California, Irvine Irvine, CA

M.S. in Materials Science and Engineering **2012**
University of California Irvine Irvine, CA

B.S. in Metallurgical Engineering **2008**
AmirKabir University of Technology (Tehran Polytechnic) Tehran, Iran

Research Experience

Graduate Research Assistant **2010-2016**
University of California, Irvine Irvine, CA

Teaching Experience

Teaching Assistant **Spring 2016**
University of California, Irvine Irvine, CA

Teaching Assistant **Spring 2015**
University of California, Irvine Irvine, CA

Journal Publications

An inversion layer at the surface of n-type iron pyrite **2014**
M. Limpinsel, N. Farhi, N. Berry, J. Lindemuth, C. L. Perkins, Q. Lin and M. Law
Energy & Environmental Science

Iron pyrite thin films synthesized from an $Fe(acac)_3$ ink **2013**
S. Seefeld, M. Limpinsel, Y. Liu, N. Farhi, Y. N. Zhang, N. Berry, J. Kwon, C. Perkins, J. C. Hemminger, R. Q. Wu and M. Law
Journal of the American Chemical Society

ABSTRACT OF THE DISSERTATION

Synthesis and Characterization of Pyrite Thin Films and Single Crystals for PV Devices and Fundamental Studies

By

Nima Farhi

Doctor of Philosophy in Materials Science and Engineering

University of California, Irvine, 2016

Professor Matthew Law, Chair

Iron pyrite is an earth-abundant, non-toxic, and inexpensive semiconductor that has the potential to produce large photocurrents in photovoltaic devices. However, the efficiency of pyrite solar cell devices has been limited by its photovoltage (< 0.2 eV). The surface layer of pyrite has been identified as the reason behind the low efficiency of pyrite devices. Highly pure single crystals of pyrite were synthesized, characterized, and studied in this work to determine ways to boost the photovoltage of pyrite. Based on a numerical modeling of Hall coefficient and conductivity data, it was found that there is a surface inversion layer on the surface of the pyrite crystals. The presence of the inversion layer, plus the ionization of deep bulk donor states at the surface, has resulted in an extreme upward band bending and a sharp triangular potential, across which charge carriers can tunnel and thereby, degrade the V_{OC}. A clear route involving the reduction of the density of the bulk donors by changing the condition of the crystal growth was demonstrated. Theoretical calculations showed that the reduction in the bulk donor density could indeed

increase the photovoltage in pyrite photovoltaic devices. Lastly, pyrite single crystals were doped to understand the effect of several elemental impurities (Co, Cr, and Ni) on the optical and electronic properties of pyrite. A combination of experimental characterization techniques along theoretical calculations was necessary to understand the effect of each dopant fully. Overall, this work demonstrates a clear path forward to overcome the problems associated with pyrite and achieve high efficient pyrite solar devices.

Chapter 1

INTRODUCTION

1.1 Renewable Energy Sources: Solar

The global energy demand is increasing, and it is expected to increase from 18 terawatts (TW) in 2012 to 27 TWs in 2040. [1] These demands should be met with energy sources that conserve the environment and doesn't enhance the climate change. Therefore, finding and utilizing a safe, sustainable, low cost, and abundant energy sources is very important and essential. Sun is an energy source that has the potential to meet the energy demand without emitting greenhouse gasses and putting the environment in danger.

The amount of energy from the sun that strikes the earth in just ninety minutes (6.45×10^{20} joules) is more than the amount of energy consumed on earth in one year (5.8×10^{20} joules). [2] There are different ways to utilize the sun energy. One of the main approaches of utilizing the solar energy is via using photovoltaic devices (PV). PV devices convert the solar energy directly into electricity and are the focus of this dissertation. Cost is the primary limitation of large use of photovoltaic devices and solar energy in general. If the cost per watt of energy produced by

solar become comparable with the cost per watt of energy produced by fossil fuels, we can expect the widespread use of PV devices.

PV panels have been used since the 1950s in certain applications (e.g. satellites), but the widespread use of them has started only in the past decade. This large growth in the use of PV panels is due to finding routes to manufacture them with lower costs. Now, the cost of energy generation by PV panels has become comparable to using fossil fuels in certain sun-rich cities. [3] Traditional silicon p-n junctions are the most widespread commercial PV devices. In these devices, silicon is used as the absorber material. The cost of silicon panels has reduced a lot in the past decade due to extensive research on them. But since silicon has a low absorption coefficient, it needs to be hundreds of microns thick to be able to absorb enough sunlight. Therefore, there is still room to reduce the cost of PV panels and to further enable the growth of them. Using thin films of cheap materials as the absorber layer can further reduce the cost for material processing. Materials such as CIGS (copper indium gallium selenide) and cadmium telluride (CdTe) due to their high absorption coefficient can be used in thin film form and absorb sunlight efficiently and potentially further reduce the cost of fabricating the PV devices. However, the scarcity of indium and tellurium in the earth's crust might limit their use in the near future and don't make them the best candidate for multi-terawatt energy production.

An ideal photovoltaic absorber material should have certain properties. Its electronic band gap should be close to the ideal range of 1.0-1.5 eV. Parameters like charge carrier mobilities and lifetimes should be high in order to have high efficient devices. A High absorption coefficient is also needed to allow utilizing thin films and reducing the total cost of devices.

A study by Wadia et al. [4] has looked at 23 potential PV absorber materials for availability and cost for terawatt scale installations. The study has determined that iron pyrite (pyrite) has the highest potential among the other semiconducting materials to lower the cost per watt of produced electricity. The high potential of pyrite arises from its low material extraction cost and its large electricity production potential. Moreover, the abundancy of pyrite in the earth's crust makes it a great candidate for terawatt scale energy production. Figure 1.1 and Figure 1.2 show the annual electricity production potential and raw material cost of studied materials, respectively. Pyrite tops the list in both criteria. [4]

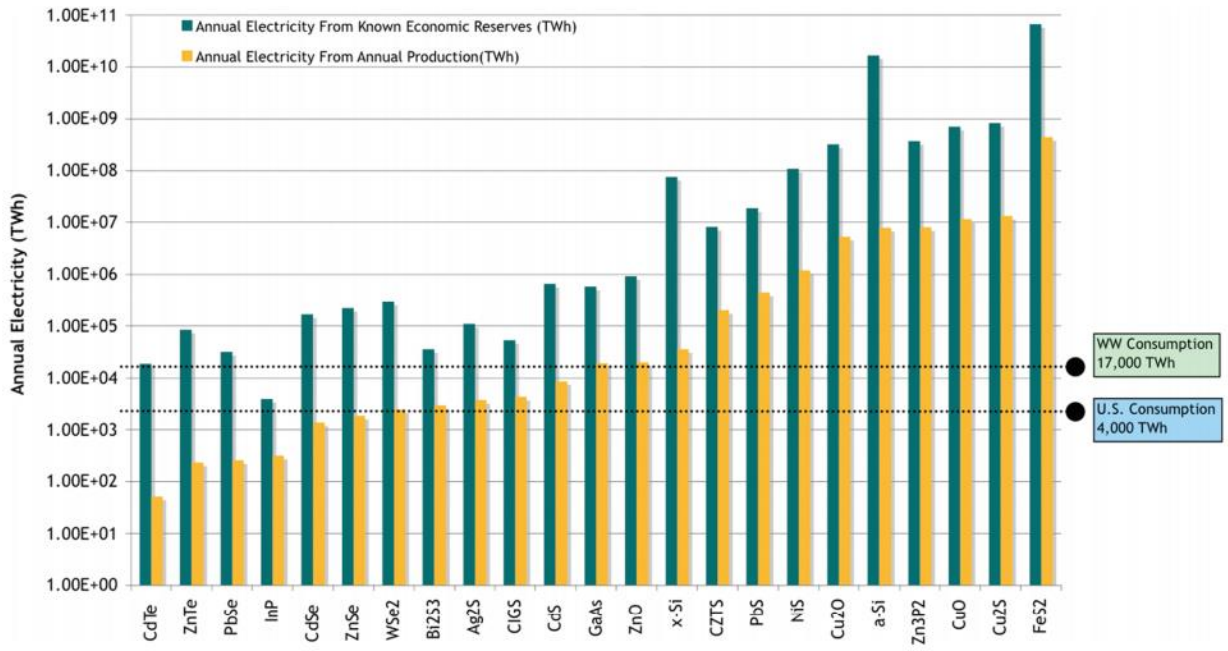

Figure 1.1: Potential for electricity production. Annual electricity from known economic reserves (green), and annual electricity from annual production (yellow) for 23 inorganic PV materials. Figure is taken from [4].

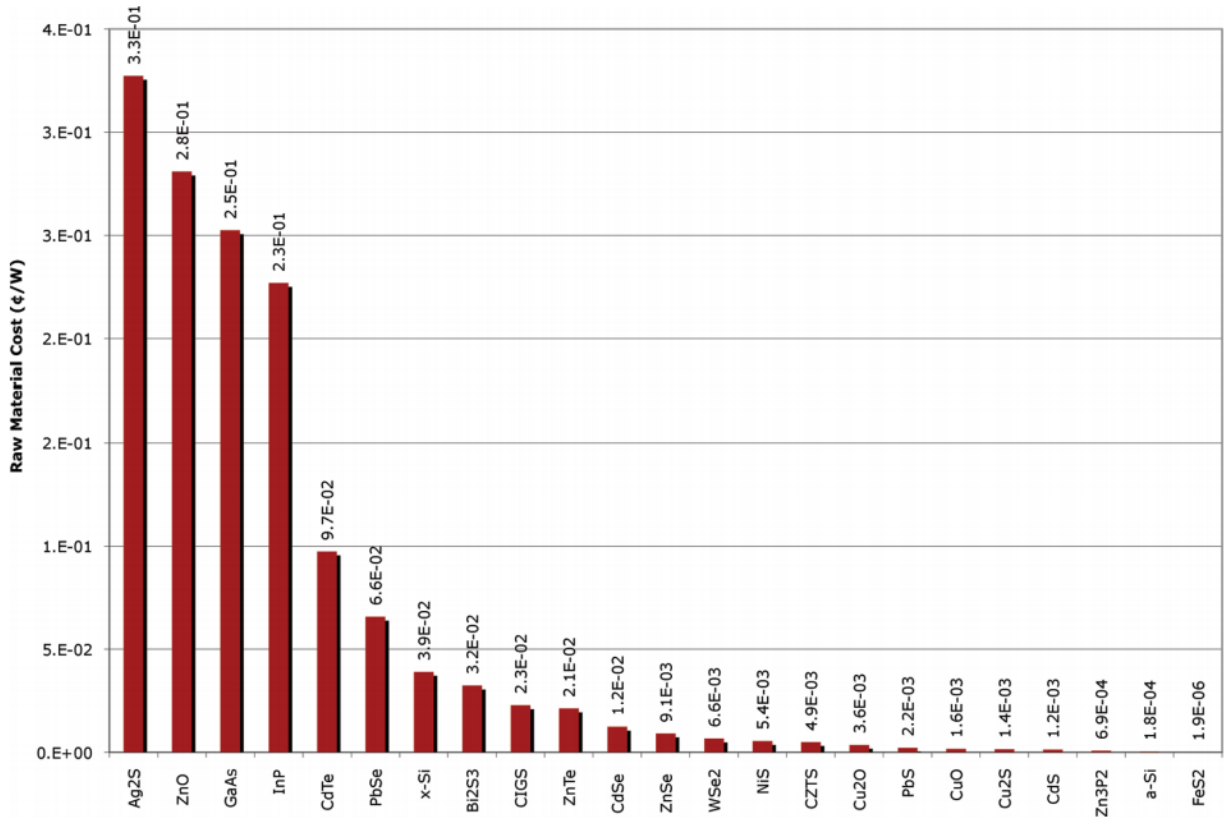

Figure 1.2: Raw material cost. Minimum cost (US cent/W) for 23 inorganic PV materials based on the raw material cost. Figure is taken from [4].

1.2 Pyrite

The most abundant sulfide in the earth's crust is pyrite (FeS_2). It is a promising material for use in thin film photovoltaic (PV) applications. Its crystal structure is similar to rock salt. It can be described as $Fe^{2+}S_2^{2-}$, in which Fe^{2+} ions are located at face-centered cubic sublattice and sulfur dimers are pointing along the <111> direction. Iron has a slightly distorted octahedral ligand field and is surrounded by six sulfur atoms. Each sulfur atom has tetrahedral coordination and is surrounded by three iron atoms and the sulfur of the dimer pair. The basic electronic structure

of pyrite has been extensively studied. The non-bonding Fe 3d t_{2g} orbitals have formed the top of the valence bands, and the bottom of the conduction band consists of Fe e_g* states with some hybridization of S 3p orbitals. Figure 1.3, shows the crystal structure and the simplified electronic structure of pyrite. [5- 15]

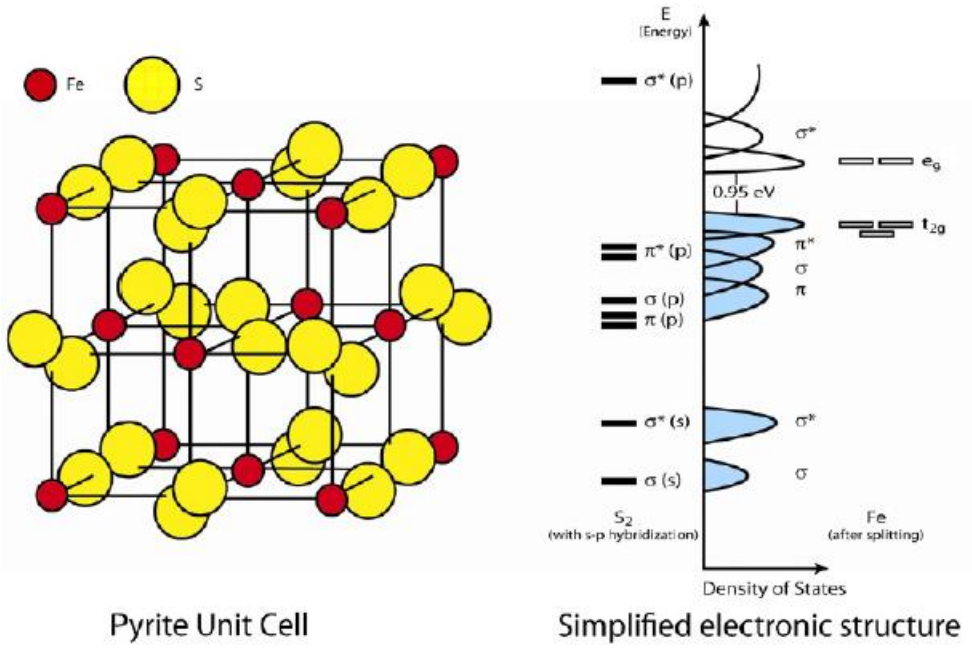

Figure 1.3: Left: unit cell of iron pyrite, image courtesy of Matt Law. Right: Simplified electronic structure of pyrite, image is adapted from [16].

Pyrite has a suitable band gap of 0.92 eV, strong light absorption ($\alpha > 10^5$ cm^{-1} for $h\upsilon > 1.3$ eV), and an adequate minority carrier diffusion length (100-1000 nm). All of these properties plus the infinite materials availability have made pyrite an extremely exciting material for multi-terawatt PV deployment. [4] [17] [18] [19] As mentioned, out of 23 inorganic PV materials studied by Wadia et al., pyrite is calculated to be the most economically attractive material. Therefore, it can reach multiple TWs of electricity generation without resource limitations. [4]

Pyrite was mainly investigated for use in photovoltaics and photoelectrochemical cells by the group of Helmut Tributsch in Germany at Hahn-Meitner Institüt in the 1980s. Pyrite thin films and synthetic pyrite crystals were made by this group via different methods. Photoelectrochemistry of natural and synthetic samples was studied by the group. [20- 23]

The first pyrite solar cell was reported in 1984 using a CVT (chemical vapor transport) grown pyrite crystal as an electrode, forming a liquid junction with an aqueous electrolyte of KI and I_2. [24] The initial devices had efficiencies of ~1% with large photocurrents and small photovoltages ($<$ 200 mV). Schottky junctions with Ni and Au were also attempted, but the liquid junctions showed more promising results. Later on using iodide/triiodide electrolyte to make pyrite photoelectrochemical cells improved the efficiencies to 2.8%. The most efficient photoelectrochemical cell of pyrite is reported by Antonucci (η=3.3%). [25] Screen printed pyrite electrodes were used in a photoelectrochemical setup with an aqueous electrolyte. Heat treatment of pyrite in hydrogen gas was the reason behind the increase of photovoltage.

Not much work after this point has been reported. Several experiments involved implementing of pyrite nanocrystals in different cell structures. Pyrite has also been used to sensitized TiO_2 photoelectrochemical cells and pyrite/polymer bulk heterojunctions. None of these works resulted in better performing cells. The reason behind the low photovoltage of pyrite remains unknown. [24, 25]

The low voltage of pyrite has been mainly attributed to the presence of defect states in the gap that arise from sulfur vacancies and other point defects. FeS-like layers on the surface can form

due to sulfur vacancies. Sulfur deficiency also may change the coordination number of iron from six to five. This change in ligand field causes iron states to relax into the band gap. In general, impurities and other defects will introduce additional traps and recombination centers which will result in the reduction of the photovoltage. Surface properties of pyrite have also been shown to be very important since pyrite has strong light absorption and most of the carriers are generated close to the surface. [26- 28] In the latest study published by our group, it is believed that the low photovoltage of pyrite devices is mainly due to the presence of a hole-rich surface inversion layer. This will be extensively discussed in Chapter 4. [29, 30]

1.2.1 Pyrite Thin Films

Pyrite films have been made by different methods such as sulfurization of iron and iron oxide thin films, [31- 35] direct and reactive sputtering, [36- 41] spray pyrolysis, [42] flash evaporation, etc. [43, 44] Since pyrite thin films in this study have been made via chemical vapor deposition (CVD), only CVD deposited pyrite films are discussed.

The Tributsch group has deposited pyrite with CVD mainly by using iron pentacarbonyl (IPC) as their iron source. Hydrogen disulfide (H_2S), sulfur (S), tert-butyl sulfide (TBS), and tert-butyl disulfide (TBDS) are the sulfur precursors that have been used by them. The deposition temperature was in the range of 130-600°C. All the reported films were p-type. At room temperature, they had low dark resistivity (0.1-1 Ω cm) and low carrier mobility. High deposition

temperatures (> 450°C) and high sulfur precursor pressures were needed to obtain phase pure pyrite films and avoid the formation of marcasite (orthorhombic FeS_2) and pyrrhotite ($Fe_{1-x}S$) crystal phases. [22, 27, 45- 49] Schoonman et al. used iron(III) acetylacetonate and TBDS as their iron and sulfur precursors. Pyrite was deposited at 300-340°C, and hydrogen was also required for a proper film growth. These pyrite films also showed p-type conductivity, and they had low dark resistivity. There are a few reported films with n-type conductivity. The Nakamura group in Japan has used $FeCl_3$ and thioacetamide to grow pyrite films. The deposition temperature was fairly high (450-550°C), and the films showed n-type conductivity. [50] [51]The n-type behavior of the films is probably due to the presence of Cl. Recent DFT modeling shows that Cl acts as a donor in pyrite. [52]

1.2.2 Pyrite Single Crystals

Single crystals are good model systems to understand fundamental properties of materials. High elemental and phase purity and the absence of grain boundaries are several advantages of single crystals over polycrystalline thin films. Most studies of pyrite single crystals are on naturally grown crystals and synthetic crystals. Synthetic pyrite crystals are mainly grown via chemical vapor transport method (CVT). CVT takes advantage of a temperature gradient. Elements of the desired compound with a transport agent are placed on the hot end of a tube. The transport agent will initially interact with precursors, and then the resulting gaseous compounds are transported to the cold end of the tube. Single crystals of the desired compound grow on the

cold end of the tube. There are a few reports on flux growth of pyrite single crystals as well. Usually, halogen based compounds are used as transport agents to grow the crystals. CVT crystals have good quality, but they are typically small in size. The risk of contamination with the transport agent is another issue with CVT crystals. Halogens as transport agents can act as possible n-type dopants in pyrite and may change the electrical properties of the crystals. [27, 53- 57]

In the flux growth method, a flux (solvent) is used to melt the precursors at high temperatures. The crystals are then grown in a slow cooling step of the mixture. In 1967, $PbCl_2$ was used as a flux to grow pyrite crystals. [53] Tellurium and alkali polysulfides have also been used as fluxes to grow binary and ternary sulfides. In all of them, the chosen flux had the ability to dissolve iron and sulfur together at low temperatures with respect to their melting points. [54, 58] Sheikh et al. used a combination of tellurium and copper sulfide to grow pyrite crystals. The crystals were n-type with a room-temperature carrier concentration of 7.5×10^{15} cm^{-3}. Kloc et al. [59] used a sodium sulfide flux in a fairly complicated system. Pyrite crystals proved to be n-type by Hall effect measurements. In general, most of the reported synthetic pyrite crystals are n-type unless they are intentionally doped. Phosphorus and arsenic have been shown to be p-type dopants, while cobalt and nickel have been shown to be n-type dopants. [55, 56, 60]

1.3 Scope of this work

This work assesses the potential of pyrite photovoltaic devices by looking at the pyrite thin films and single crystals. Experimental and computational methods are explained in chapter 2. Chapter 3 is dedicated to pyrite thin films. Thin films of pyrite have been synthesized with CVD, and have been integrated into p-n junctions. Chapter 4 demonstrates the flux growth of single pyrite crystals. It summarizes the properties of single crystals and discusses ways to improve the open circuit voltage of pyrite solar devices. The effect of doping on single pyrite crystals is presented in chapter 5. Cobalt, chromium, and nickel are the dopants that their effect has been investigated. Lastly, summary and suggestions for future works are presented in Chapter 6.

Chapter 2

Experimental methods

2.1 Synthesis of Pyrite

Pyrite single crystals and thin films have been made via different routes. In this study, thin films of pyrite have been made via atmospheric chemical vapor deposition (CVD), and single crystals of pyrite have been made via a flux growth method. The following sections have described the details of each method.

2.1.1 Chemical Vapor Deposition (CVD)

A homemade atmospheric-pressure hot wall chemical vapor deposition reactor, built by former graduate student Nick Berry, has been used to deposit pyrite thin films. Pyrite thin films were reproduced and characterized based on Nick Berry's results. [61]

The system consists of two single-zone, 1-inch quartz tube furnaces. Figure 2.1 shows an overview of the system. Iron(III) acetylacetonate (≥ 99.9%, Aldrich) and tert-butyl disulfide (97%, Aldrich) are used as the iron and the sulfur precursors, respectively, while argon is used as the

carrier gas. The iron precursor is placed on an aluminum boat and is located in the upstream furnace. The sulfur precursor is held in a stirred bubbler which is placed in a 60°C oil bath. It is introduced to the upstream of the downstream furnace (growth furnace) with the help of argon as the carrier gas. There are two other argon flows that are introduced in the downstream furnace. One is the flow for the iron precursor, while the other is a forward flow needed for good deposition. The flow of each argon line is controlled by digital mass flow controllers. The upstream furnace is set at 150°C, and the growth furnace is set at 300°C. Substrates (glass or molybdenum coated glass) are placed in the center of the growth furnace.

Deposited films are mixed phase, and contain both pyrite and marcasite. Therefore, they are required to go under a sulfur annealing step to have a pure phase pyrite and convert marcasite (orthorhombic iron disulfide) to pyrite. For the sulfur annealing, pyrite films and 50 mg of sulfur (99.999 Alfa Aesar) are sealed in evacuated quartz tubes and are heated at desired temperatures (500°C-550°C) for 2-8 hours. The sulfur annealing condition is determined by the type of substrate and the thickness of the pyrite films. Sulfur annealing not only changes the morphology of the deposited film, but also converts all the marcasite to pyrite.

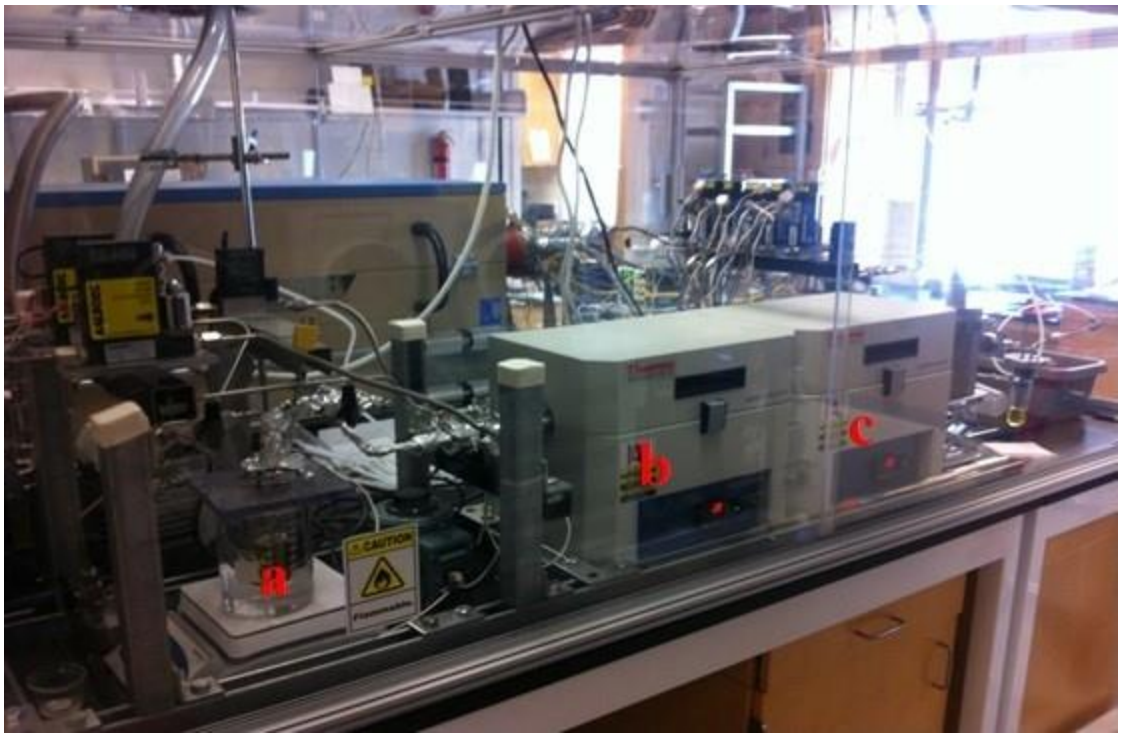

Figure 2.1: Overview of the CVD system (a) TBDS bubbler (b) Upstream furnace (c) Downstream furnace

2.1.2 Flux Growth

Pyrite single crystals are grown via a sodium polysulfide flux. Sodium sulfide is used as the flux due to the fact that is liquid over a wide range of compositions and temperatures (Figure 2.2). Nick Berry initially showed the ability of growing pyrite single crystals with this method. The process was optimized and became air-free afterward. The detailed process is published in [29], and is discussed below.

Standard pyrite single crystals were synthesized in sodium polysulfide flux [59, 62] by heating an evacuated quartz ampoule containing a crucible filled with high-purity iron, sulfur, and Na_2S to 780°C and cooling to room temperature over ~24 hours. Na_2S-sulfur is an excellent flux for pyrite

crystallization because it is liquid over a wide range of composition and temperature (Figure 2.2), shares a common anion with pyrite, and features a cation that does not incorporate into pyrite to any significant degree (< 200 ppb according to secondary ion mass spectrometry measurements, see Table 4.2).

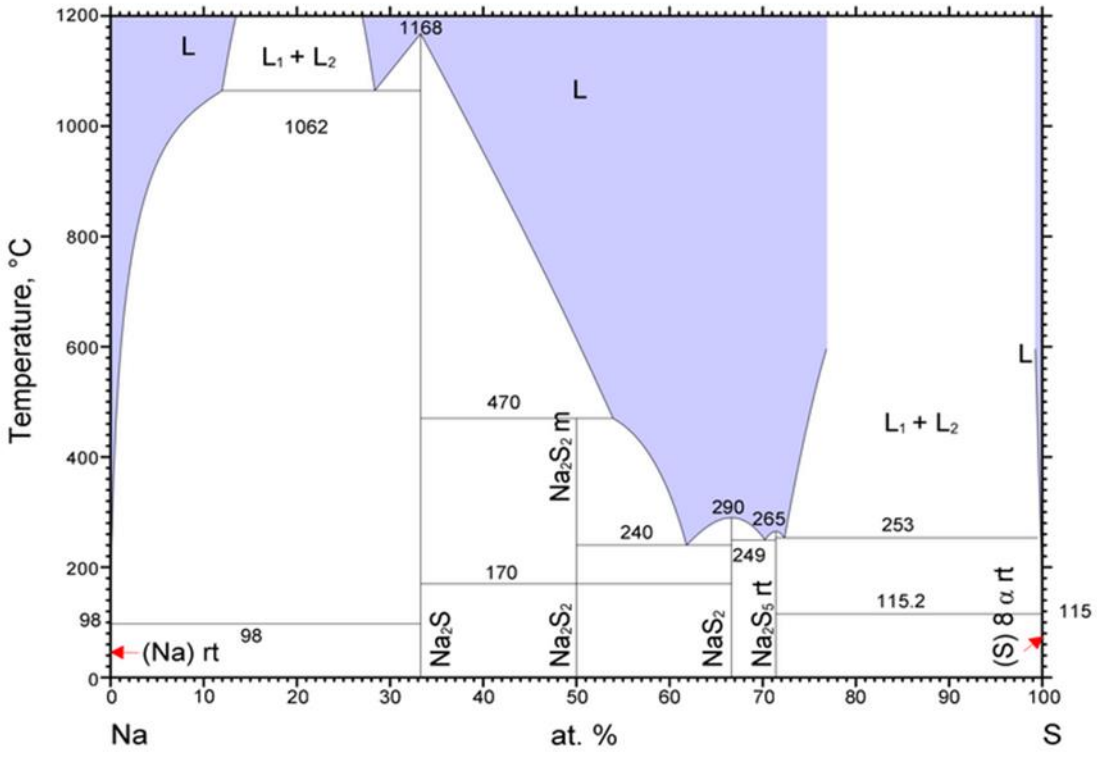

Figure 2.2: The Na-S binary phase diagram (data from [63]). Mixtures of Na_2S and S have eutectics as low as 240°C. There is also a region of binary liquid immiscibility above 253°C near the sulfur-rich end of the system.

Starting materials of the highest available purity (metals basis) were used and further purified to remove possible nonmetal impurities, such as water and oxygen. Iron powder (99.998%, 22 mesh, Alfa Aesar) was loaded into a pyrolytic boron nitride (pBN) crucible and reduced in a quartz

tube furnace in a flow of 5% H_2/95% Ar at 300°C for 15 hours to remove water and surface oxides. Higher temperatures (> 450°C) led to undesirable agglomeration of the iron powder. Sulfur powder (99.9995%, Alfa Aesar) was degassed and dried in a quartz flask under a dynamic vacuum of ~30 mTorr at 130°C for 3 hours. $Na_2S{\cdot}9H_2O$ (> 99.99%, Aldrich) was crushed, then dried and degassed in a quartz flask under a dynamic ~30 mTorr vacuum at 300°C for 5 hours, resulting in a mixture of fine colorless and yellow powder (Na_2S and polysulfides, respectively). After purification, all three starting materials were immediately transferred to an N_2-filled glovebox (< 0.1 ppm O_2, LC Technologies) without exposure to air. [29]

Pyrite crystals were grown in alumina crucibles (99.5%, LSP Ceramics) or pBN crucibles (99.999%, Morgan Technical Ceramics) sealed in evacuated quartz ampoules. All procedures were performed rigorously air free. 0.50 grams of iron (8.9 mmol) was placed in the bottom of the crucible, followed by 0.71 grams of Na_2S (9.1 mmol) and 1.29 grams of sulfur (40.2 mmol). The crucible was then loaded in a quartz tube, which was then connected to a vacuum hose with a closed isolation valve. This apparatus was removed from the glovebox, attached to a vacuum manifold, purged with 99.999% Ar, pump/purged to < 20 mTorr three times, and sealed at < 20 mTorr with a hydrogen/oxygen torch. The quartz ampoule was held vertically the entire time to avoid mixing or spilling the contents of the crucible. The ampoule was placed in the center of a vertical tube furnace, heated at a rate of 13 °C min^{-1} to 780°C, held at 780°C for 6 hours, cooled to 625°C over 24 hours, and finally cooled naturally to room temperature over 5 hours (36 hours total). The slow-cooled (slow-grown) crystals received the same heat treatment, but the cooling time from 780°C to 625°C was extended to 2-7 days instead of 24 hours The crucible was then

removed from the ampoule and placed into a beaker of Millipore water for several hours to dissolve the flux. 80% of the time this procedure results in one large pyrite crystal, while several smaller crystals are produced 20% of the time. The crystals are sonicated in Millipore water to remove flux residue, rinsed many times with Millipore water, dried, and stored in the glovebox.

2.2 Thin Film Depositions

In order to make solar devices with pyrite thin films or pyrite single crystals, and for the evaluation of different passivation treatments, materials other than pyrite is needed to be deposited. In this section, each method is briefly discussed.

2.2.1 Sputtering

Sputtering is a physical vapor deposition technique used to deposit thin films of a variety of materials. Ionic gas atoms (usually argon) are directed to a target of desired material. Due to the bombardment of the target, the sputtering material is ejected and can get deposited on the substrate of choice. [64]

A seven source magnetron sputter tool (AJA International Inc.) was used for this work. Molybdenum (Mo), zinc sulfide (ZnS), zinc oxide (ZnO) and aluminum-doped zinc oxide were the main materials being deposited. Most of the main depositions were made by Moritz Limpinsel. The exact experimental details are reported here [65].

2.2.2 Thermal Evaporation

Thermal evaporation is another common method to deposit thin films of metals. A source material is evaporated in a vacuum environment by resistive heating. The evaporated particles are then deposited on a substrate of choice. A thermal evaporator inside a nitrogen-filled glovebox was used mostly to deposit gold in this work.

2.2.3 Atomic Layer Deposition (ALD)

Atomic layer deposition is a layer by layer deposition technique with a highly conformal coating. It involves sequential gas phase reactions on the face of the substrate. In this work, it was used to deposit oxides for passivating the surface of pyrite samples. Alumina (Al_2O_3) and zinc oxide (ZnO) were the primary materials deposited.

2.3 Preparation of Single Crystals

Pyrite crystals grown by flux method need to undergo certain procedures for characterization and solar device making. In this section, the main preparation methods are discussed.

2.3.1 Sectioning and Polishing

In order to use the single crystals for solar cell devices or for most of the characterization techniques, they need to undergo a sectioning and polishing procedure. Single crystals were mounted in epoxy (Buehler EpoxyCure) for sectioning. A slow-speed diamond saw (Model 650, South Bay Technology) was used to cut 500–1000 μm thick slabs from the flux crystals parallel to their largest surface facet (usually a {111} plane). The slabs were then released from the epoxy by soaking in dichloromethane for 2 hours. To obtain fine-polished surfaces with ∼2 nm RMS roughness, as-cut slabs were first polished sequentially with SiC paper of grit size 600, 800, and 1000, followed by sequential lapping with 3 μm and 1 μm diamond slurries and, finally, 20 minutes of lapping with 50 nm Al_2O_3 slurry (Buehler MasterPrep). Residual slurry particles were removed by sonication in Millipore water. The polished slabs were then transferred and stored in the glovebox. [29]

2.3.2 Acid Etching

In order to clean the polished surfaces completely from polishing residues and at the same time have the surface of different polished slabs with a similar condition, fine polished slabs were etched either in 1% hydrofluoric acid (HF) or in HNO_3: HF: CH_3COOH =2:1:1 (HNA solution) for 1 minute.

2.3.3 Electrical contact

In order to measure the electrical properties of pyrite thin films and pyrite single crystals ohmic, contacts were needed. An ohmic electrical contact is a non-rectifying electrical junction in which the whole voltage drop is across the sample. To make an ohmic contact to pyrite thin films, colloidal silver paint was applied to the corner of the films. Making ohmic contacts with the single crystals however, proved more of a challenge. Applying colloidal silver to a fine-polished surface of pyrite single crystals would not always yield ohmic contacts, and as a result, the surface of pyrite crystals had to be locally roughened prior to the application of the colloidal silver.

2.4 Structural and Morphological Characterization

2.4.1 X-ray Diffraction

X-ray diffraction (XRD) is a powerful tool for identifying phase composition and structural properties of single crystals and thin films. It relies on the constructive and destructive interference of scattered x-ray beam from the sample. In this work, we have looked at both single crystals and pyrite thin films with XRD.

A Structure determination by single crystal X-ray diffraction was performed on a Bruker SMART APEX II diffractometer at 143 K using ∼0.2 mm specimens removed from as-grown crystals. Diffraction data were collected on a CCD area detector using Mo Kα radiation (λ = 0.71073 Å). A

full sphere of data was collected for each crystal. The APEX2 software package was used for data collection and determination of unit cell parameter. Data were absorption corrected using SADABS-2008/1. The structures were solved by direct methods and refined by a full-matrix least-squares routine on F^2 with SHELXL97. The diffraction symmetry was $m\bar{3}$ and the systematic absences were consistent with the cubic space group $Pa\bar{3}$. The single crystal X-ray data was analyzed by Brandon Mercado. [29]

Thin film X-ray diffraction (including room-temperature rocking curves, 2ϑ–ω scans, and pole figures) was performed on a Rigaku SmartLab diffractometer. X-ray rocking curves and 2ϑ–ω scans were acquired on the SmartLab configured with a Ge(440) × 4 monochromator featuring an angular resolution of 5.4 arcseconds. Synchrotron XRD measurements were performed on pulverized crystals in capillary transmission mode at Beamline 11-BM of the Advanced Photon Source (λ = 0.413141 Å) at Argonne National Laboratory. [29]

2.4.2 X-ray Tomography

Tomography refers to imaging by looking at different sections. X-ray tomography (XRT) was used to look at flux-grown single crystals. The main goal was to identify the density and size of voids in the crystals. XRT measurements were performed on a Zeiss Xradia 410 Versa with a 4× objective lens.

2.4.3 Raman Spectroscopy

Raman spectroscopy is a spectroscopic technique to identify different phases by looking at vibrational and rotational modes in a system. Raman spectroscopy was used in conjunction with XRD to probe for marcasite phases (a polymorph of pyrite). It's been shown that Raman is more sensitive than XRD to probe for marcasite phases. In this work, a Renishaw inVia confocal Raman microscope with a 50× objective lens and a 523 nm laser operating at less than 5 mW was used.

2.4.4 Scanning Electron Microscopy (SEM)

Scanning electron microscope (SEM) images were acquired on an FEI Magellan 400 XHR SEM.

2.4.5 Atomic Force Microscopy

Surface topography was measured using an Asylum MFP-3D atomic force microscope (AFM).

2.5 Elemental Analysis

Different elemental analysis techniques have been used to look at the elemental purity of both thin films and single crystals. In this section, the experimental parameters of each method are discussed.

2.5.1 Glow Discharge Mass Spectrometry (GDMS)

Elemental composition of the crystals was determined by Evans Analytical Group using glow discharge mass spectrometry (GDMS). GDMS measurements were performed on a VG 9000 GDMS instrument (Thermo Scientific). Powdered pyrite specimens were pressed into high-purity In foil (99.99999%) previously cleaned with acid to remove surface impurities. Impurities in the In foil were analyzed prior to elemental analysis of each sample. Glow discharge conditions of 1.0 kV, 2.0 mA, and 100 Pa of 99.9999% Ar were used for all measurements. Samples were pre-sputtered for five minutes prior to data acquisition. The intensities of the ion beams were measured with a Faraday cup for iron, sulfur and indium isotopes and a Daly conversion detector for all analytes in the samples. The efficiency of the detectors was calibrated using ^{180}Ta (relative isotopic abundance of 0.012%) measured on the Daly detector and ^{181}Ta (relative isotopic abundance of 99.99%) measured on the Faraday cup during analysis of pure Ta metal. Scan points per peak were 70 channels, DAC steps of 7 with integration times of 100 and 160 ms for the Daly detector and Faraday cup, respectively. [29]

2.5.2 Instrumental Gas Analysis (IGA)

IGA measurements were performed by Evans Analytical Group to look at the gas forming elements. Measurements were performed on a Leco TC 600 oxygen/nitrogen analyzer, a Horiba EMIA-820V carbon/sulfur analyzer, and a Horiba EMGA-621W hydrogen analyzer. Samples were

prepared in a glovebox by loading small crystal pieces into Sn capsules for the inert gas fusion measurements. [29]

2.5.3 Inductively Coupled Plasma Mass Spectrometry (ICP-MS)

Nu AttoM High-Resolution ICP-MS system was used to inspect the elemental purity of single crystals. Crystals needed to be dissolved in distilled trace metal basis nitric acid. Thus, an acid digestion vessel was used, and the vessel was heated to 170°C and kept at that temperature for 4 hours. After the heat treatment, pyrite crystals were completely dissolved in the nitric acid and were ready for measurements. In order to quantify elements, standard solutions were measured by the instrument as well. The results were finally analyzed by the Nu Quant software (version 1.1135.1).

2.5.4 Secondary Ion Mass Spectrometry (SIMS)

Evans Analytical Group performed SIMS. It was performed on a PerkinElmer Physical Electronics Model 6600 dynamic SIMS instrument using 4 keV Cs ions for anions (S, O, H, C, F, and Cl) and 5 keV O_2 ions for cations (Na, K, Mg, Ca, Cr, and Al). Estimated detection limits were 1×10^{15} atoms cm^{-3} for Na, K, Al, Mg, Cr, and Ca, 5×10^{17} atoms cm^{-3} for C, 2×10^{18} atoms cm^{-3} for O and H, and 5×10^{16} atoms cm^{-3} for F and Cl. Atomic concentrations are accurate to within a factor of two for

oxygen and a factor of five for all other elements. The depth scale was quantified by measuring the analysis craters with a stylus profilometer. [29]

2.5.5 Inductively Coupled Plasma Optical Emission Spectrometry (ICO-OES)

ICP-OES measurements were done by Evans Analytical Group using a PerkinElmer Optima 7300V spectrometer operating at 1300 W. 0.1 g samples were digested in a closed vessel containing 2 mL HNO_3 and 6 mL HCl in 5 mL H_2O in an Anton Paar multiwave 3000 microwave (HF100 rotor).

2.6 Optical Characterization

To measure the optical absorption of both pyrite thin films and single crystals, Fourier Transform Infrared Spectroscopy (FTIR), and Ultraviolet-Visible Spectroscopy (UV-Vis) were used. FTIR enabled measuring optical extinction in mid-IR and far-IR, while UV-Vis enabled the measurement of optical transmission and optical reflection at higher energies ($E > 0.6$ eV).

2.6.1 Fourier Transform Infrared Spectroscopy (FTIR)

A Nicolet 6700 instrument in transmission mode was used to measure the optical extinction spectra of single crystals. A Janis ST-100 cryostat was used to measure the temperature

dependent optical extinction. Small pyrite crystals (~3 mm × 3 mm) were mounted on a copper disk with 2 mm diameter circular aperture.

2.6.2 Ultraviolet-Visible Spectroscopy (UV-Vis)

A PerkinElmer Lambda 950 spectrophotometer equipped with a 65 mm integrating sphere was used to measure optical transmission and optical reflection spectra of both thin films and single crystals. The Janis ST-100 cryostat was used with the UV-Vis whenever temperature dependent data was needed.

2.7 Electrical and Magnetic Characterization

2.7.1 Temperature dependent Conductivity and Hall effect

Hall effect data were acquired from 80 to 350 K on an Ecopia HMS-5000 instrument (0.55 T magnet) inside an N_2-filled glovebox using the van der Pauw method. Samples were mounted with thermal grease (Apiezon Type N) to a glass slide bonded to the sample stage. Ohmic contacts were made with colloidal silver paste. The Hall coefficient was calculated as $R_H = \frac{V_H d}{IB}$, where V_H is the measured Hall voltage, d the crystal thickness, I the applied current, and B the magnetic field strength. The applied current was adjusted from 1 μA at 80 K to 1–2 mA at 350 K.

Hall effect data were also acquired at Lake Shore Cryotronics on a Model 9709A Hall Measurement System using a DC field strength of 2 T from 40–350 K and a 8404 AC/DC HMS using an AC field strength of 0.63 T RMS from 350–700 K. Ohmic contacts were made with colloidal silver paste. The applied current was adjusted from 50–100 nA at 40 K to 8–10 mA at 700 K. Conductivity values from the different measurement setups showed excellent agreement across the range of overlapping temperatures. Magnetoresistance measurements were performed in the 9709A system using a DC field strength of up to 90 kOe. The current at 300 K and 70 K was 10 mA and 100 nA, respectively. The resistivity at each magnetic field was calculated using the standard van der Pauw method. [29]

2.7.2 Magnetic Properties Measurement System (MPMS)

A Quantum design Magnetic Properties Measurement System (MPMS 5XL) in Molecular Instrumentation Center (MIC) at UCLA was used. The MPMS uses a Superconductivity Quantum Interference Device (SQUID) magnetometer to track small changes in magnetic flux and discover the magnetic moment of a sample. Single crystals of pyrite were measured by the instrument from room temperatures down to 2 K. Magnetic moment was measured at a range of DC fields from 0 to ±5 T.

2.8 Data Modelling

Data modeling was used to interpret the electrical data (mostly from Hall effect measurements) obtained from single crystals, as detailed in the section below.

2.8.1 Hall Effect Model

Electrical conductivity and Hall coefficient data were modeled using the multilayer conduction model of Petritz. [66] Our implementation of the model assumes that electrical transport occurs in parallel through three layers – the crystal bulk and identical surface inversion layers on the top and bottom of the single-crystal slab – while neglecting currents across their interfaces. Calculation of the Fermi level (E_F), carrier concentrations (n and p), conductivity (σ), and Hall coefficient (R_H) of the bulk and surface layers utilizes the charge neutrality condition:

$$N_D^+ + p = N_A^- + n \quad (1)$$

where N_D^+ and N_A^- are the concentrations of ionized donors and acceptors, given by [67]

$$N_D^+ = \frac{N_D}{1+\exp\left[\frac{(E_F(T)-E_D)}{(kT)}\right]} \quad (2)$$

$$N_A^- = \frac{N_A}{1+\exp\left[\frac{(E_A - E_F(T))}{(kT)}\right]} \quad (3)$$

Here, N_D and N_A are the concentrations of donors and acceptors and E_D and E_A are their respective energy levels. The carrier concentrations are given by

$$n(T) = \int_{E_C}^{\infty} \mathrm{DOS}(E)\left(\frac{1}{e^{\left[\frac{E-E_F(T)}{kT}\right]}+1}\right)\mathrm{d}E \quad (4)$$

$$p(T) = \int_{-\infty}^{E_V} \mathrm{DOS}(E)\left(1-\frac{1}{e^{\left[\frac{E-E_F(T)}{kT}\right]}+1}\right)\mathrm{d}E \quad (5)$$

Because the valence and conduction bands of pyrite are probably not parabolic, we compare in most calculations the parabolic DOS(E) against an explicit numerical DOS(E) obtained from our recent density functional theory (DFT) calculations of the pyrite band structure. [52] In accord with literature, we use a temperature-dependent band gap, $E_g(T) = E_g(0) - \frac{T^2 \times 0.00189\,\mathrm{eV\,K^{-1}}}{T+1915\,\mathrm{K}}$, and assume equal shifting of the conduction and valence band edges with temperature. [68, 69]

The calculation is performed by substituting eqs. (4) to (7) into eq. (1) to give a self-consistent expression for $E_F(T)$ that is numerically solved for E_F at each temperature. After calculating $n(T)$ and $p(T)$ from $E_F(T)$, the conductivity $\sigma(T)$ and Hall coefficient R_H(T) are obtained from the general expressions:

$$\sigma(T) = e(n\mu_e + p\mu_h) \quad (6)$$

$$R_H(T) = \frac{E_y}{J_x B} = \frac{p\mu_h^2 - n\mu_e^2}{e(p\mu_h + n\mu_e)^2} \quad (7)$$

where the temperature-dependent carrier mobilities μ_e and μ_h are extrapolated from unipolar regions of the Hall data. The electron mobility follows a $T^{-2.5}$ law at temperatures above ~150 K, as expected for phonon scattering. Finally, the contributions of the bulk and surface layers are combined to determine the total σ(T) and $R_H(T)$:

$$\sigma_{total} = \sigma_b \frac{d_b}{d} + 2\sigma_s \frac{d_s}{d} \quad (8)$$

$$R_{H,total} = R_{H,b}\left(\frac{\sigma_b}{\sigma_{total}}\right)^2 \frac{d_b}{d} + 2R_{H,s}\left(\frac{\sigma_s}{\sigma_{total}}\right)^2 \frac{d_s}{d} \quad (9)$$

where d_b and d_s are the thicknesses of the bulk and the surface layers, respectively, and $d = d_b + 2d_s$ is the total slab thickness. Overall, there are five free parameters used for modeling the Hall data (N_D, N_A, E_D, E_A, and μ_h) as well as four quantities parameterized from experimental data or theory (DOS(E), $E_g(0)$, μ_e, d_s). Some calculations also included compensation in the bulk by adding a bulk acceptor with concentration $N_{A,bulk}$ and ionization energy $E_A - E_V$ = 50 meV. The calculation

routine was implemented in Igor Pro 6.12. It has to be noted that the code was written and developed by Moritz Limpinsel and was used for all the Hall modeling in this work. [29, 65]

2.8.2 Band Diagram

The software program 1D Poisson (http://www3.nd.edu/~demand/) by G. Snider was used to calculate band edge energies and carrier concentrations as a function of distance from the crystal surface. The inversion layer was modeled by assuming a Schottky barrier at the surface of n-type pyrite (with N_D and E_D taken from Hall effect results) with a barrier height chosen so that the Fermi level was located ~100 meV above the valence band edge, in agreement with UPS results.

2.9 Solar Cell Fabrication

2.9.1 Thin film p-n Junctions

Pyrite thin films are p-type. Therefore solar cells were fabricated based on commercially available CIGS solar cells. Figure 2.3, illustrates the general layout that was utilized. Molybdenum (Mo) was sputtered on glass to serve as a metal back contact. Next, the pyrite layer was deposited via CVD on the Mo-coated substrates. Mixed phase pyrite and marcasite films needed to undergo sulfurization to obtain phase pure pyrite. Therefore, pyrite films and a specific amount of sulfur were sealed in an evacuated quartz tube. The evacuated quartz tubes were then annealed at

elevated temperatures (500°C- 600°C) for certain hours (2- 8 hours). The annealing method and the annealing parameters are discussed in details in Section 3.5. Sealed tubes were opened in a glovebox, and the rest of fabrication steps were all completed in an air-free environment. Zinc sulfide (ZnS) was the n-type window layer that was deposited next by reactive sputter coating to form a p-n junction with the pyrite layer. Zinc oxide (ZnO), aluminum-doped zinc oxide (AZO) were the consequent layers that were all deposited via sputtering afterward. During this work, different device structures were used to improve reproducibility and device performance. Therefore, masks were used to deposit the layers. The two main device structures are discussed in Section 3.5. Lastly, it should be noted that all layers deposited by sputtering were done by Moritz Limpinsel.

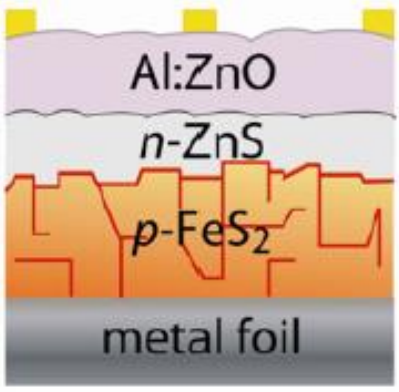

Figure 2.3: The general device stack of pyrite thin film solar devices. The figure is taken from the original proposal by Prof. Matt Law.

2.9.2 Single Crystal Junctions

Flux-grown pyrite single crystals were used in solid state Schottky junctions and wet junctions. In both junctions, single crystals were first cut into slabs. The bottom facets of the slabs were polished rough (600 SiC paper) in order to be able to make ohmic contacts to them. The top facets were fine polished, however. The slabs were then etched in the HNA solution.

For the wet junctions, a conductive wire was connected to the bottom facet by using colloidal silver, and the whole slab and the contact were covered in epoxy with only the top facet left free. The made pyrite electrode was used in a three neck electrochemical cell along with platinum (Pt) as the counter electrode, and Ag/AgCl as the reference electrode. The aqueous electrolyte was chosen based on previous pyrite wet junctions. [16] It consisted 0.7 M HI, 0.15 M CaI_2, and 0.03 M I_2. The junction was measured under dark and under AM 1.5G light via a potentiometer.

In order to make the solid-state Schottky junctions, the slabs were mounted on a glass slide with a colloidal silver line contacting the bottom facet. Then, gold or platinum was deposited through a mask by thermal evaporation as the Schottky metal. The top facet was contacted with a small dot of colloidal silver. The current-voltage curves were measured inside a glovebox by using tungsten needle probes and Keithley 2636 source-measure unit (SMU). It should be noted that the solar cell fabrication and testing were done by Moritz Limpinsel or Trenton Salk (graduate students).

Chapter 3

Pyrite thin films

3.1 General properties

Pyrite thin films were deposited by CVD. The CVD system was made by a former graduate student at Law lab, Nick Berry. Films were fully characterized by Nick Berry. [61] In this work, the CVD films were used in making pyrite solar devices, to understand the effect of marcasite on pyrite films, to understand the effect of sodium on sulfur annealing, and to understand the effect of wet passivation treatments on the electrical properties of films. The current section summarizes the general properties of the films.

SEM images along with XRD spectra of the films on molybdenum coated glass before and after sulfur annealing are shown in Figure 3.1. Sulfur annealing not only changes the morphology of the deposited film but also converts all the marcasite to pyrite. As it is shown in Figure 3.1c, the marcasite peak at ~26 degrees disappears after the proper sulfur annealing. Also, due to the sulfur annealing, the molybdenum layer is partially sulfurized. The formed MoS_2 layer is apparent in Figure 3.1b. It should be noted that all the characterization of the pyrite thin film was carried

out by Nick Berry and reproduced in this work. Necessary changes to the deposition and processing conditions were done based on the used substrate.

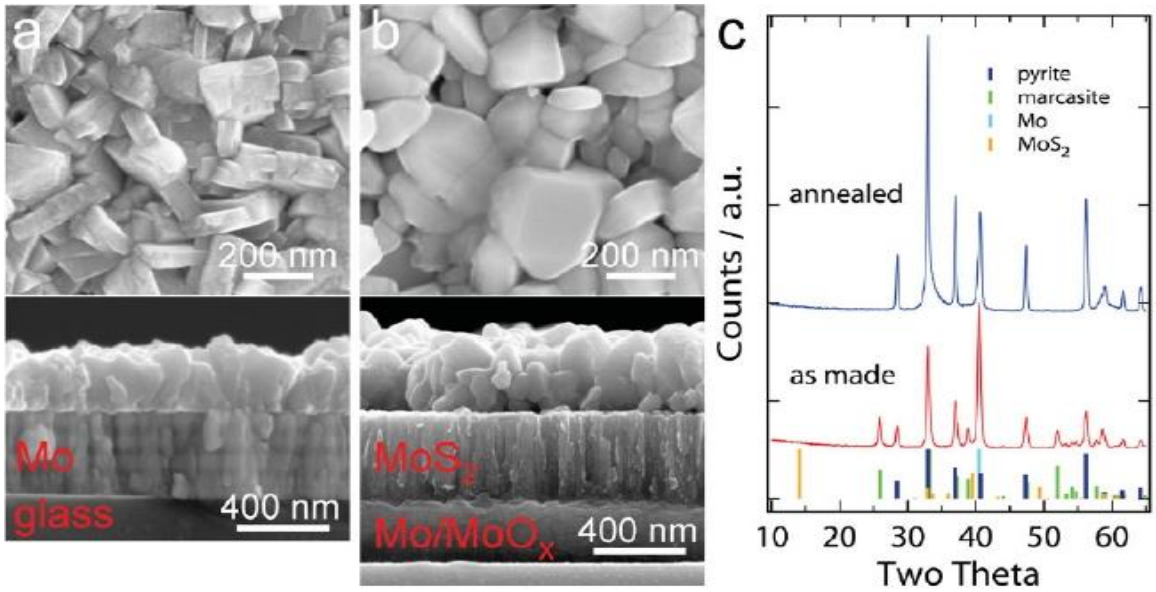

Figure 3.1: Typical Fe_{S2} thin films on Mo-coated glass, plan view and cross-sectional SEM image of a film (obtained by Nick Berry) (a) before and (b) after sulfur annealing (c) XRD pattern of the films along with pyrite, marcasite, molybdenum, and MoS_2 reference patterns. Figure is reproduced from [61].

To measure optical properties of the films, thin pyrite films (100-150 nm) were grown on glass substrates. The transmittance and reflectance of the films were measured by a Perkin Elmer Lambada 950 spectrophotometer equipped with a 65 mm integrating sphere. The optical absorption coefficient and the band gap of the sulfur annealed pyrite films are calculated based on these measurements (Figure 3.2). The best band gap fit shows an indirect gap of 0.97 ± 0.05 eV, and the absorption coefficient is bigger than 3×10^{-5} cm^{-1} for energies above 1.7 eV.

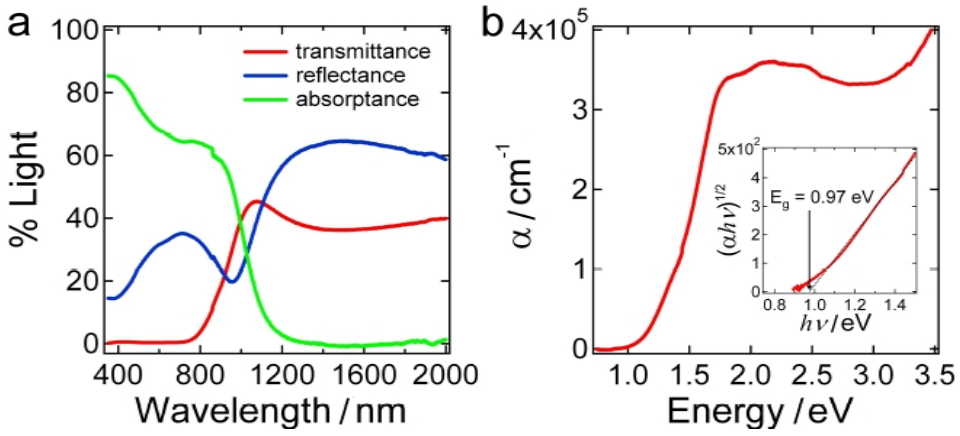

Figure 3.2: Optical properties of 150 nm grown pyrite films on glass (obtained by Nick Berry) (a) transmittance, reflectance, and absorptance of the film (b) calculated absorption coefficient of the pyrite film. The onset is the Tauc plot used to estimate the optical band gap of the film. Figure is reproduced from [61].

Van der Pauw Hall effect measurements were carried out to understand the electrical properties of the films. Resistivity, majority carrier type, majority carrier concentration, and mobility of the samples were measured by this method. The electrical behavior of the films before and after annealing is about the same (Figure 3.3). They have a low resistivity at room temperature with a small activation energy of 28.8 $\pm$ 1.8 meV. Temperature dependent resistivity of the films indicates that they are highly doped non-degenerate semiconductors (Carrier concentration = 10^{18}-10^{20} cm^{-3}, mobility < 2 $cm^2\,V^{-1}\,S^{-1}$). Since the in-plane hall mobility of the films is too small, the carrier type of the films is determined by qualitative thermopower measurements, and it's believed to be always p-type. [61]

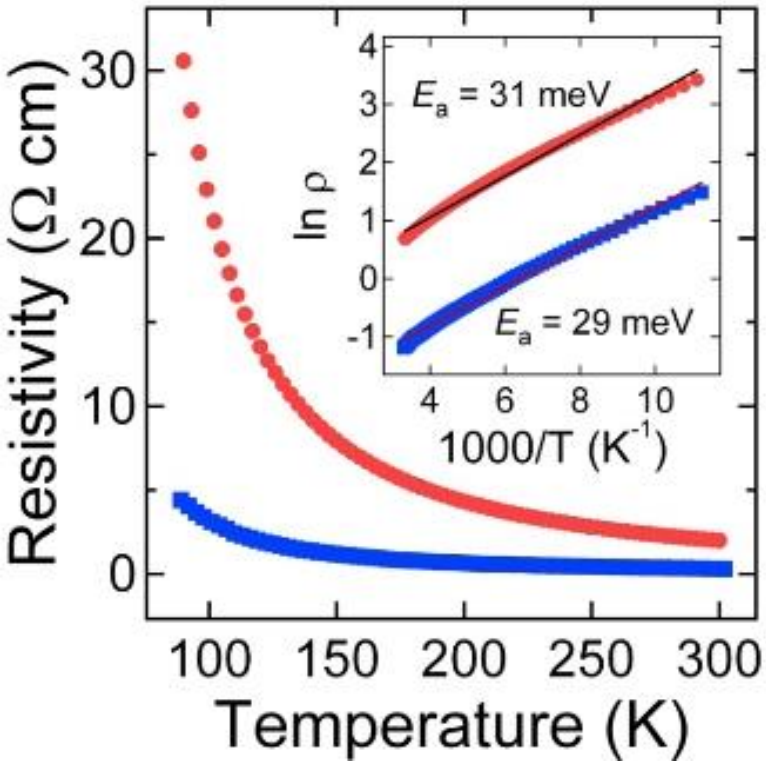

Figure 3.3: Temperature dependent resistivity before (blue) and after (red) sulfur annealing (obtained by Nick Berry). Figure is reproduced from [61].

3.2 Effect of alkali metals on annealing

Alkali metals have been observed to have an impact on the conversion rate of marcasite to pyrite, and the grain growth of pyrite. It has been shown that the presence of sodium (Na) favors nucleation and growth of pyrite. [61] At the same time, it has been observed that better pyrite morphology was obtained on Na-free glass substrates (borosilicate glass). The molybdenum deposited on these glasses was smoother. Hence the CVD deposited pyrite layer would end up with better morphology and more homogenous thickness (less roughness). Consequently,

sodium free substrates were chosen as the substrate of choice for all solid-state thin film pyrite devices. However, not having Na present during the deposition and the sulfur annealing steps makes obtaining phase pure pyrite very difficult. Figure 3.4, shows the Raman spectra of two pyrite films deposited on two different types of glass. One substrate contained Na and the other did not contain Na. After the same sulfur annealing conditions (50 mg of sulfur, 500°C, 2hrs), the film deposited on the Na-free glass substrate contained a substantial amount of marcasite (the peak at 320 cm^{-1} in Raman), and the other film was phase pure pyrite. In order to achieve phase pure pyrite films, pyrite films on the Na-free substrates need to undergo harsher sulfur annealing conditions (T > 550°C, t > 4hrs). Harsh sulfur annealing conditions have also proven not to be favorable for pyrite thin film devices. Sulfur annealing causes Mo to convert to MoS_2. Therefore, long hours of sulfur annealing at high temperatures (T > 550°C) will result in a complete conversion of Mo to MoS_2 that causes mechanical instability for devices. Consequently, in order to achieve phase pure pyrite films with good morphology and mechanical stability, sodium was chosen to be controllably delivered to our films. In this section, the different routes of introduction of Na are discussed and compared together. Raman spectroscopy was used to look for traces of marcasite (Raman has shown to be more sensitive than XRD in finding marcasite), XRD was used to search for any additional Na-containing phases on pyrite films, and SEM was used for analyzing the morphology of the films.

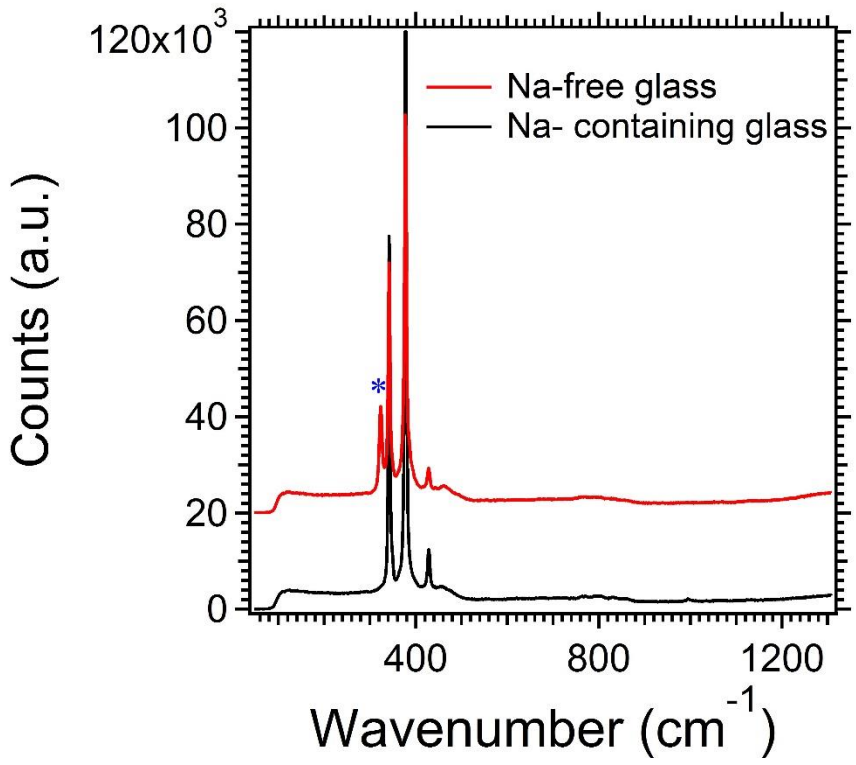

Figure 3.4: Raman spectra of sulfur annealed (500°C for 2hr) pyrite films deposited on soda lime glass (contains Na), and borosilicate glass (Na free). The peak due to marcasite is present at ~320 cm^{-1} and it is labeled by the asterisk. All the other peaks are known Raman bands for pyrite. The presence of Na has caused the complete conversion of marcasite to pyrite.

Sodium can be introduced controllably at different stages of pyrite film fabrication. It can be added to the glass substrate, it can be added to the molybdenum coated glass, it can be added during the CVD deposition of pyrite, or it can be added during the sulfur annealing process. Sodium fluoride (NaF), sodium sulfide (Na_2S), and sodium acetylacetonate were the three sources of Na that were examined in this work. Evaporating a thin (2 nm) layer of NaF on the Mo-coated glass showed to be effective in converting all the marcasite to pyrite, but it caused a very rough deposition of pyrite on the Mo substrate. The addition of sodium acetylacetonate during the CVD process to the iron boat also showed promising results, but that also degraded the quality of

deposition. Na_2S sodium addition was the most promising route out of the other ones. In order to conserve the good morphology of the film, Na_2S had to be introduced during the sulfur annealing step. To introduce Na, Na_2S was dissolved in methanol, and the solution was drop cast on the backside of substrates before the sulfur annealing step. The solution was evaporated by pumping on the substrates, and then the films were sulfur annealed. It was found, the presence of more sodium will lead to the faster conversion of marcasite to pyrite, but at the same time excess sodium will result in the formation of sodium containing particles on the surface of pyrite. Figure 3.5, shows the XRD pattern, Raman spectra, and the SEM images of the pyrite films after sulfur annealing (500°C for 4 hours) when there was enough, excess, and lack of sodium. The optimum condition was achieved by the addition of 9 μgr of Na_2S to the pyrite films. The optimum sodium addition results in obtaining phase pure (no marcasite based on Raman, and no Na-containing phases based on XRD) pyrite films on molybdenum substrates with good morphology and mechanical stability.

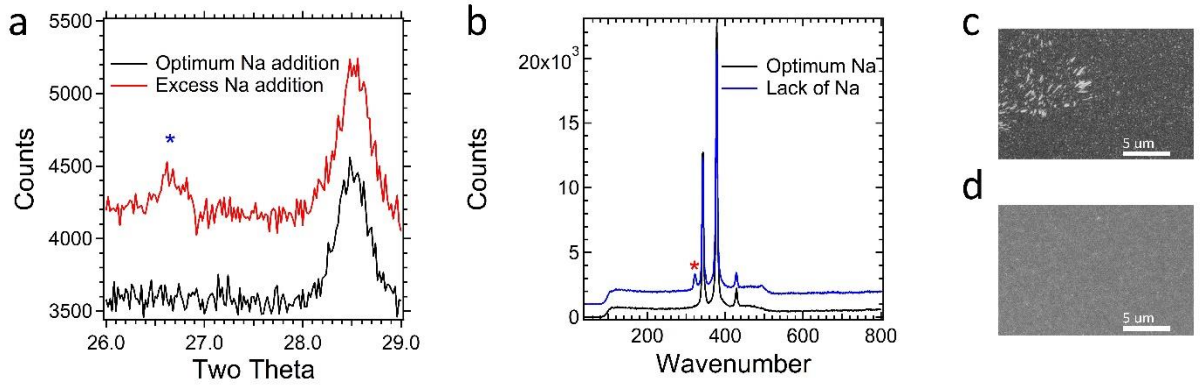

Figure 3.5: Addition of Na_2S to pyrite films on molybdenum substrates. a) XRD pattern of the optimum condition (9 μgr of Na_2S), and excess amount of Na_2S (15 μgr of Na_2S), extra sodium introduces deposition of sodium containing phases at ~26.6° (labeled by the asterisk). b) Raman spectra of the optimum condition, and not sufficient amount of Na_2S condition. Lack of sodium results in the partial conversion of marcasite to pyrite. c, d) SEM images of two films with excess amount of sodium and the optimum amount of sodium, respectively. When there is too much sodium present, sodium containing particles are present on top of pyrite.

3.3 Effect of marcasite

Marcasite is a polymorph of pyrite with an orthorhombic crystal structure. It has been believed to have a low band gap for a long time, and its presence will cause the reduction of the band gap of the pyrite. [70] A more recent density functional theory (DFT) argues that marcasite has a larger band gap than pyrite. [71] In order to understand the effect of marcasite on FeS_2 films, the band gap of marcasite was calculated with DFT, and measured optically. The theoretical part was done by Prof. Wu's lab at UCI (details at [72]), and the experimental part was done at Prof. Law's lab. Hundred nm thick FeS_2 films were grown on quartz substrates. Since quartz doesn't have any sodium, films growing on it have significantly larger marcasite content (~50 vol% marcasite,

phase quantification was done by XRD pattern analysis using the PDXL software package (Rigaku)). By careful sulfur annealing of the samples, phase pure pyrite films were obtained, and the optical properties of the films before and after annealing were compared. The comparison shows only subtle differences in absorptivity spectra and estimated optical band gap (Figure 3.6c-d). The band gap of the mixed-phase films is only slightly smaller than the band gap of the phase pure films (0.92 eV versus 0.96 eV), and there is a small shoulder at ~1.25 eV which is only present in mixed-phase films. Also, there is a more gradual increase in the absorption coefficient of mixed-phase films. Finally, phase-pure films show a more pronounced dip in absorptivity at ~3 eV. These data provide strong evidence that the optical band gap of marcasite is at least as large as that of pyrite, contrary to previous belief and in agreement with recent DFT calculations. Figure 3.6, shows XRD, Raman and optical properties of the FeS2 films on quartz before and after annealing. [9, 10, 72]

In conclusion, the optical band gap of marcasite is larger or equal to the bandgap of pyrite. However, due to complexities that mixed phase films might have, we chose to work with only phase pure pyrite films.

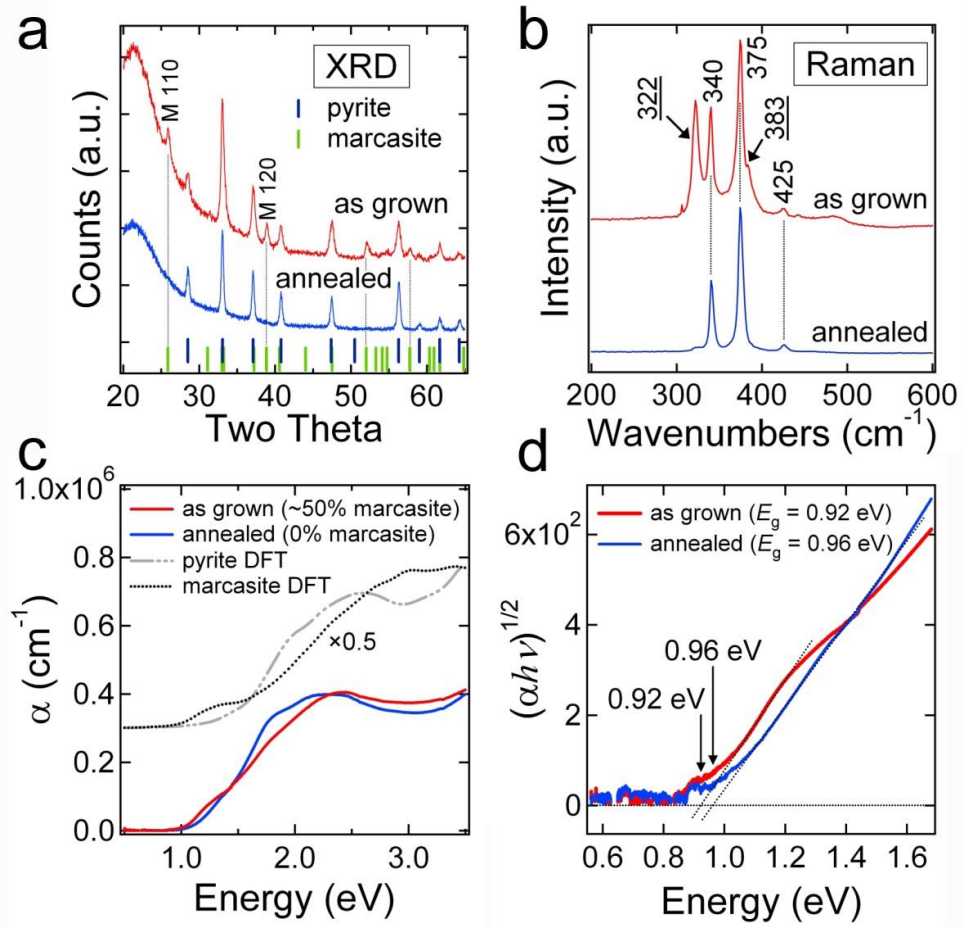

Figure 3.6: (a) XRD patterns and (b) Raman spectra of CVD-grown FeS_2 films before and after sulfur annealing (322 cm^{-1} peak is the marcasite peak). (c) Absorptivity spectra of the as-grown film (red) and annealed film (blue), as well as calculated spectra for pyrite (gray hashes) and marcasite (black dots). The marcasite spectrum is the average of the optical functions along the [100], [010], and [001] directions of the orthorhombic crystal. The calculated spectra are multiplied by a factor of 0.5 and offset for clarity. (d) Plot of $(\alpha h\nu)^{1/2}$ versus energy used to estimate the band gap of the two films. Figure is adapted from [72].

3.4 Surface modification

Thin films inherently have a high surface to bulk ratio. It is believed that the surface states in pyrite thin films have dominated the transport mechanism at all temperatures (80- 350 K). [65] In

this section, the effect of chemical etching, thermal annealing in an inert and a reactive atmosphere, and overcoating with oxides on pyrite thin films was analyzed. Temperature-dependent Hall effect measurement was used to observe the effect of treatments on the electrical properties of thin films.

Pyrite thin films were deposited via CVD. The deposition time was 7 hours, and the thickness of all studied films was ~300 nm. Films were annealed in the sulfur atmosphere to make sure all the marcasite is converted to pyrite. Wet chemical passivation treatment was tested first to understand its effect on the surface states of thin films. Since halides are believed to have the ability to passivate the un-coordinated iron on the surface of pyrite (possible origin of surface states), 0.1 M solutions of cadmium chloride ($CdCl_2$), iron chloride ($FeCl_2$), and potassium iodide (K_I) were made in methanol. Phase pure pyrite films were soaked in the halide solutions for 24 hours. Then, the in-plane resistivity of the films was measured by the Hall effect system. Figure 3.7, shows the resistivity of each identical film after their respective wet chemical treatment. The electrical properties of the films remained unchanged irrespective of the treatment. It has to be noted that the treatment was done at elevated temperatures (~80°C) as well, and no effect was seen either (data not shown). Through-plane resistivity of the films after the treatment remained unchanged as well.

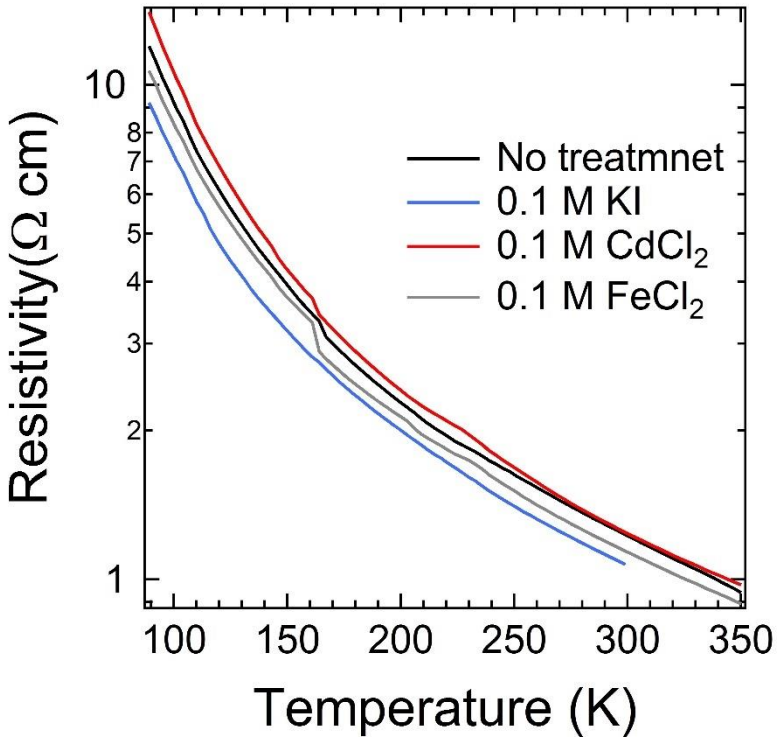

Figure 3.7: The in-plane resistivity of phase pure pyrite films after wet chemical treatment. CVD deposited films were annealed under a sulfur atmosphere (50 mg of sulfur) at 500°C for 2 hours. Then they were immersed in halide solutions for 24 hours, after blow drying the films, their resistivity was measured by the Hall effect system.

Other methods to influence the surface properties of the films were also examined. Thin oxide films were deposited on the phase pure pyrite films, and the changes in the electrical properties of the films were examined by the Hall effect system. Aluminum oxide (Al_2O_3) and zinc oxide (ZnO) were deposited by atomic layer deposition (ALD). ALD deposition is a very slow deposition technique, but it has the potential of depositing through the thickness of the sample and infilling all the pores. 20 nanometers of alumina and ZnO were deposited on the films over 15 hours (300 cycles). Alumina and ZnO were chosen due to availability, and also the potential effect of oxygen on the electrical properties of pyrite. [52] After ALD deposition, films were undergone heat

treatments in an inert (N_2) atmosphere, and a reactive H_2S atmosphere. Figure 3.8, shows the in-plane resistivity of pyrite films coated with alumina after different heat treatment conditions. No apparent changes in the resistivity of the films and the activation energy of the transport process are observed. A wide range of heat treatments in both inert and reactive atmospheres was tried. (350°C < T < 450°C between 10 minutes to 4 hours), but none of the conditions shows any significant change. The same result was true for the films coated with ZnO (data not shown).

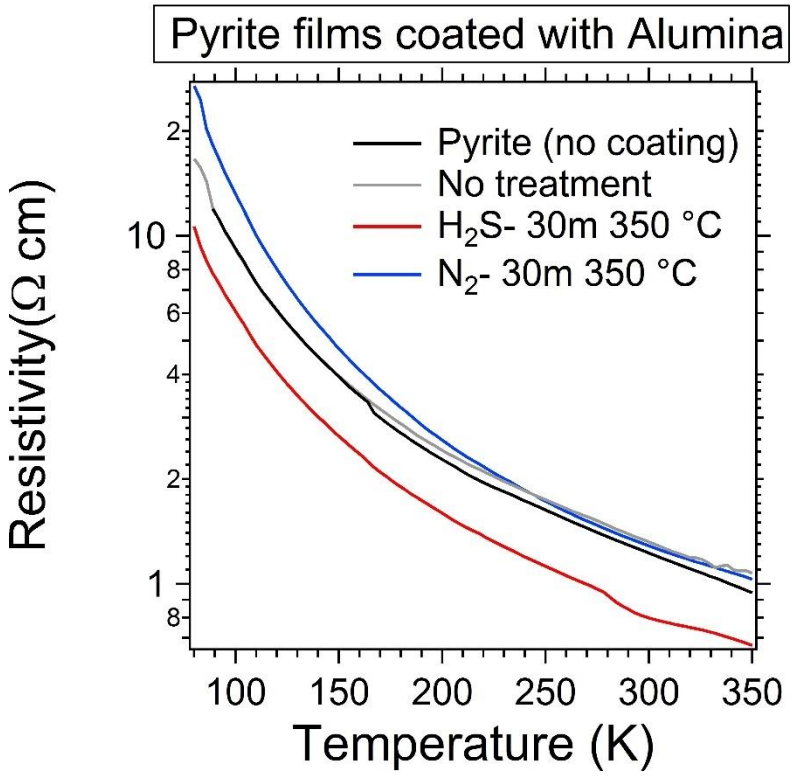

Figure 3.8: Temperature-dependent resistivity of pyrite films coated with Al_2O_3. Only a selective heat treatment conditions are shown. There were no significant changes in films after alumina deposition either with or without heat treatment.

Almost across all reported literature, pyrite polycrystalline thin films have a ubiquitous p-type electrical conduction with low activation energy and low resistivity. The fact that no significant change was observed in all our surface treatment conditions (wet solution, oxide coating, and heat treatment), suggests that none of the methods have been able to modify the reason of the p-type conduction of pyrite films. Probably, all these methods were ineffective to reach all the surfaces of the films and passivate them. To better understand the effect of the treatments, and the mechanism of the charge transport, a better system was needed. Thin films of pyrite proved to be a very complex system to study. Therefore pyrite single crystals were made and studied. Next chapter discusses the electrical properties of pyrite single crystals.

3.5 Thin film devices

Making devices was collaboratively done with Moritz Limpinsel (sputtering and device testing). As mentioned in section 2.9.1, n-type semiconductors were chosen to make p-n junctions with p-type CVD deposited pyrite layers. Several junction partners were studied, including ZnS, ZnO, CdS. Since only FeS_2/ ZnS junctions showed rectifying behavior, only the summary of ZnS junctions is reported here. For the complete summary on all junctions see [65]. The studied devices consist of the following layers:

Mo-coated glass/ MoS_2/ Pyrite (CVD)/ ZnS/ ZnO/ AZO

Sulfur annealing is needed to obtain phase pure pyrite. But at the same time, it also causes the formation of MoS_2 layer. Figure 3.9, shows a representative cross-sectional SEM of the typical devices.

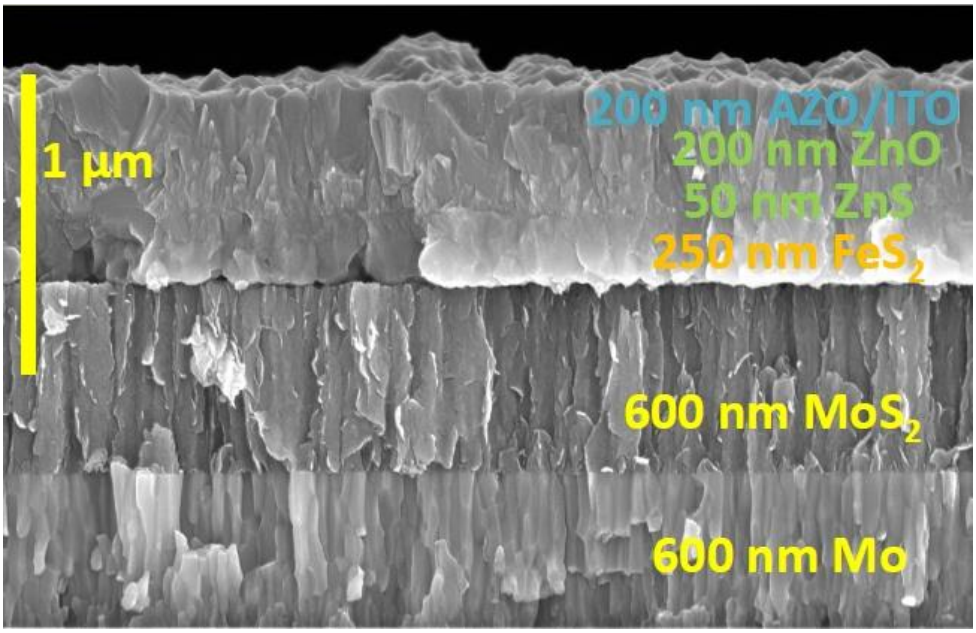

Figure 3.9- Cross-sectional SEM images of the device stack, pyrite layer is deposited via CVD, and other layers are deposited by sputtering. Image is courtesy of Moritz Limpinsel.

Device making and device testing showed to be very challenging. Reproducibility was the main challenge. It was observed that devices with supposedly similar fabrication steps end up having different electrical properties. There were several sources responsible for the reproducibility problem. First, variation in the deposited films in different runs. Second, sulfur annealing and mechanical stability of layers. Third, the inherent problems with the device structures containing such layers. Figure 3.10 shows examples of reproducibility problem that was observed. Punching through and different electrical response from supposedly identical deposited layers in different batches are shown.

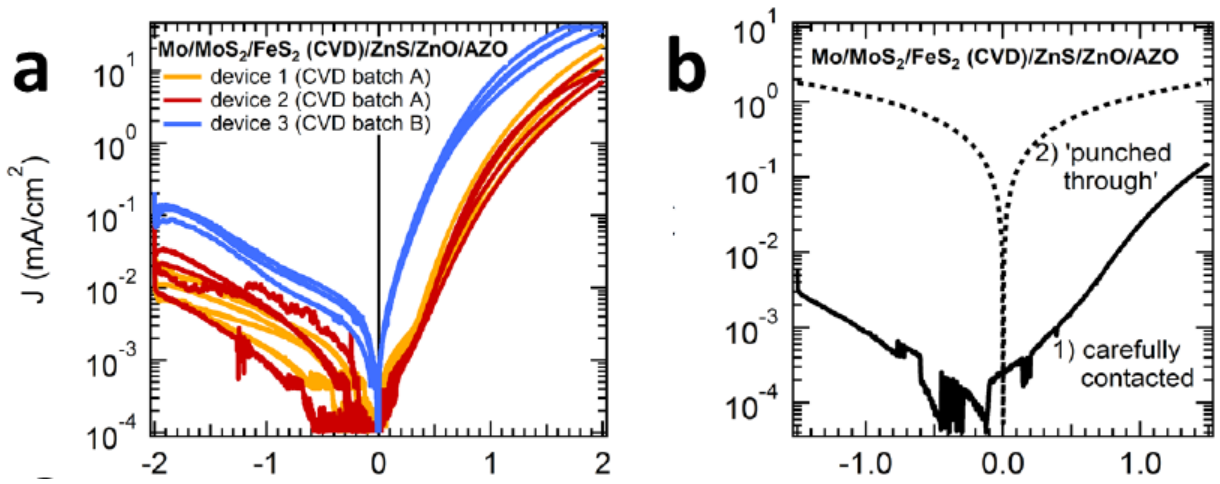

Figure 3.10: Reproducibility issues of thin film solar cells. a) Current- voltage curves for three different CVD batches (each device has 4 cells). b) Out of the two cells in the same device, one is rectifying, and the other is shorted. The cell is shorted due to punching through the layers by the contacting needle. Figure is adapted from [65].

Zinc sulfide was the layer with the most problems. Pyrite and other sputtered layers (Mo, ZnO, and AZO) didn't have any impact on the problem. It was found that even the same ZnS target from the same vendor but different batches can cause variations in results. FeS_2/ ZnS junctions with one ZnS target were rectifying and with another one not rectifying. The exact amount of H_2S present during reactive sputtering of the layer was also shown to be problematic.

Pyrite films have better quality on Na-free (borosilicate) glass. At the same time, sodium is needed to convert marcasite to pyrite at less harsh sulfur annealing conditions, and achieve good grain growth. Therefore, both sulfur annealing and sodium are needed. The problem that is associated with sulfur annealing is the formation of MoS_2 layer. This layer is mechanically unstable and acts as a lubricant. Contacting the robust AZO layer on top by the needle probes can result in shunting of the device due to the mechanically unstable underlying MoS_2 layer. The

problem with sodium addition is the uncontrollable deposition of excess sodium on some samples that can add to sources of the reproducibility problem.

Lastly, the general device structure can cause reproducibility problems. Two structures were tested in this work, the mesa structure, and the step structure. Figure 3.11 shows the structure of each design and possible areas of potential shunting. Fabrication of the mesa structure is easy. Pyrite is deposited by CVD on molybdenum coated glass. After sulfur annealing and obtaining phase pure pyrite, other layers are deposited on top of pyrite by sputtering. AZO layer is the only layer that is deposited through a shadow mask, and it serves as the top contact. Contacting such a structure with needle probes may cause punching through the layers, particularly if one of the layers (MoS_2) is very soft. To avoid such a problem, the second device structure was used. The fabrication process of the step structure is more complex due to presence of a photolithography step. The Mo layer is deposited through a shadow mask; then pyrite is deposited via CVD. After the annealing process, photolithography is needed to expose the pyrite regions that needed to be removed. The exposed pyrite regions are etched away in a solution of 10 M nitric acid for 12 seconds. Consequently, the resist is removed by soaking in acetone. The other layers (ZnO, ZnS, AZO, and metal top contact) are sputter deposited through their respective shadow masks. This approach eliminates the punching through problem, but it introduces other potential shunting sources. Sputter deposited layers through a mask have broad edges. The thickness of the layer decreases from full thickness to zero over a couple of hundreds of microns. The formation of the cliff is not inherently problematic; the problem arises when MoS_2 starts to form due to sulfur annealing. At certain areas on the edge of the deposited Mo layer, the whole thickness of the Mo

layer converts completely to MoS_2 layer. This full conversion introduces small fissures on certain parts of the structure (shown in figure 3.11b). These areas can act as potential shunting regions. Unfortunately, with Mo as the back contact, and the need for sulfur annealing, we were not able to implement a design structure without any potential problems. This problem can potentially be resolved by either eliminating the sulfurization step (finding another way of obtaining phase pure pyrite) or by finding a metal back contact that is robust during the sulfurization step.

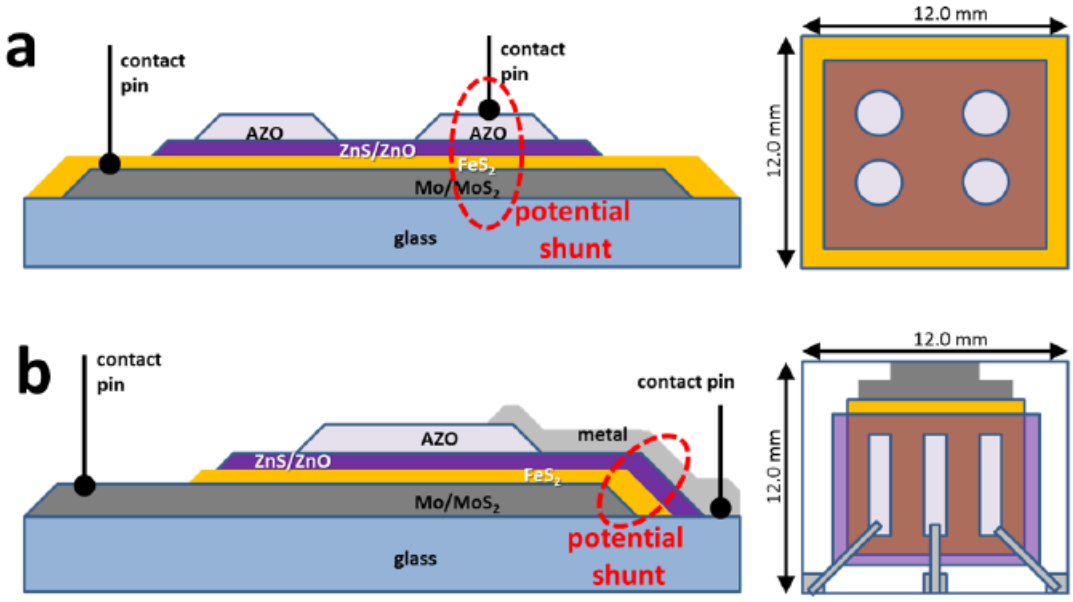

Figure 3.11: Solar cell design structures (steps). a) Mesa structure, potential route of punching through the layers due to the soft MoS_2 layer by contacting the top contact. b) Step structure, the probability of punching through the layers due to contacting is eliminated, but other shunting paths may form due to the formation of cliffs. Figure is adapted from [65].

Although these issues made performing comparative studies very hard, we were able to get well-behaved rectifying diodes reproducibly over a period of few weeks (before changes in ZnS properties). The rectification ratio (forward/ reverse current) of pyrite solid-state solar devices was around several thousand at ± 1.5 V. The best (champion) solar cell made with the CVD pyrite

film is shown in Figure 3.12. The open circuit voltage (V_{OC}) of the cell is ~240 mV, and the short circuit current (J_{SC}) is ~3 μA/cm^2 under illumination (~0.5 suns). Devices have low fill factors (< 40%), and very low power conversion efficiencies (PCE) of ~0.0002%. Although the J_{SC} is very low, it has to be noted that these devices are the first solid-state heterojunction reported with pyrite thin films. High surface recombination velocity and conduction band offset to ZnS might be the reasons behind low short circuit currents. In future, the efforts should be towards eliminating the reproducibility problems, by eliminating the sulfurization step, finding robust metal back contacts, and gaining more control over ZnS deposition. Studying the junction with X-ray Photoelectron Spectroscopy (XPS) and Time-Resolved Microwave Conductivity (TRMC) will be very beneficial in understanding the reasons behind the low short circuit currents as well.

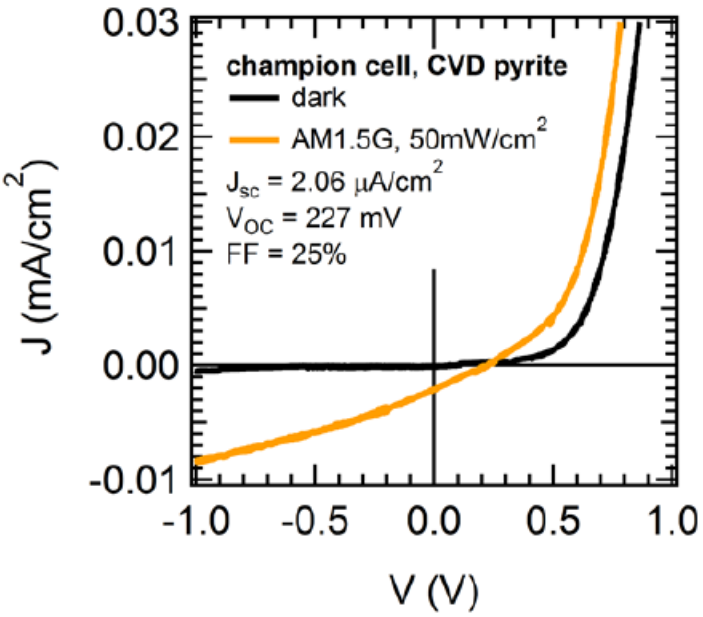

Figure 3.12: Current- voltage curve of the champion CVD pyrite device. Figure is adapted from [65].

Chapter 4

Pyrite single crystals

4.1 Characterization

In this section, the structural, elemental, electrical, optical, and magnetic characterization of flux-grown pyrite single crystal is presented (details of the growth method and characterization techniques are discussed in Chapter 2). The majority of this chapter has been part of a collaborative work with M. Limpinsel (Hall Effect and electrical modeling), N. Berry (XRD), J. Lindemuth (high-temperature Hall Effect and MR measurements), C. L. Perkins (UPS), Q. Lin (XRD), and M. Law (principle investigator). [29]

4.1.1 Structural

Basic structural characterization of the crystals is shown in figure 4.1. The flux synthesis produces highly-faceted but noncubic crystals with a typical size of 8 × 8 × 6 mm (limited by the size of our crucibles). Most of the facets are optically flat with a golden mirror finish, but some have a large density of macro-steps and small terraces. High-resolution synchrotron powder XRD patterns of

crushed crystals index to pyrite with a room-temperature lattice constant of 5.41741 ± 0.00087 Å and show no trace of other crystalline or amorphous phases (Figure 4.1b). Likewise, Raman spectra feature only sharp pyrite peaks (Figure 4.1c). Slabs were cut with a diamond saw parallel to prominent facets and polished to ∼2 nm RMS roughness using SiC paper and a series of slurries (see Section 2.3.1). Wide-angle 2ϑ–ω XRD scans show the slabs are single crystals with (111) or, less often, (210) orientation (Figure 4.1.e). (111) rocking curve peak widths of 6–9 arcseconds indicate that the pyrite slabs have a very high degree of crystalline perfection, comparable to commercial silicon wafers (Figure 4.1f). To determine whether the crystals are in fact single crystalline throughout their volume, we acquired 2ϑ–ω and pole figure data of slabs cut in several orthogonal orientations and found that nearly all specimens are indeed highly-perfect single crystals (data not shown), although a few samples showed evidence of a small number of slightly misoriented grains in pole figures. Single crystal X-ray diffraction of small crystallites (∼0.2 mm on a side) detached from the as-grown crystals showed very high-quality single crystal pyrite patterns. Crystal structure refinement yielded site occupancy factors of 1.00 ± 0.04 for both Fe and S, indicating a stoichiometry of $FeS_{2.0}$ within the error of the refinement. This agrees well with a sulfur-to-iron ratio of 1.988 ± 0.03 (*i.e.*, $FeS_{2.0}$ within experimental error) determined by closed-vessel inductively coupled plasma optical emission spectroscopy (ICP-OES) analysis of an as-grown crystal, particularly considering the tendency for sulfur to be lost to the gas phase during pyrite digestion. Overall, our results show that the flux synthesis produces large, high-quality, and stoichiometric pyrite single crystals. [29]

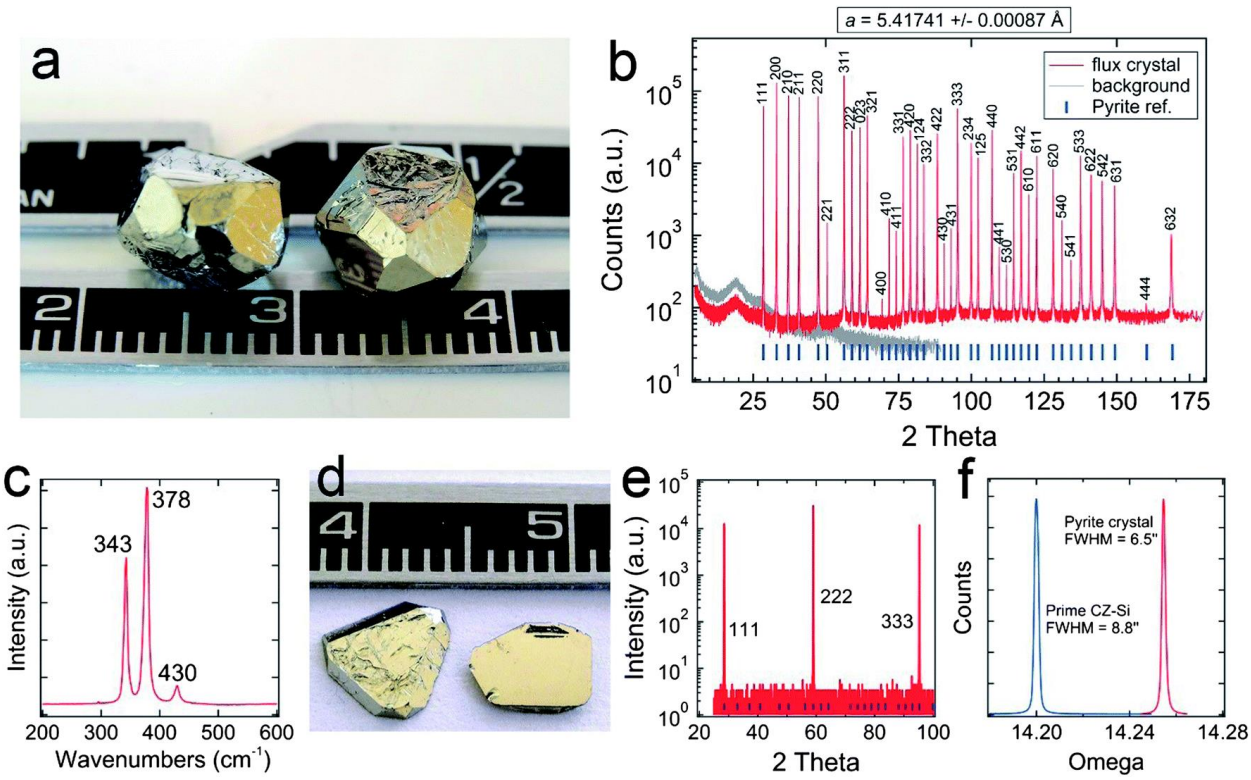

Figure 4.1: Pyrite single crystals grown in a Na_2S-sulfur flux. (a) Photograph of two as-grown crystals. Scale is in centimeters. (b) Synchrotron XRD pattern of a powdered crystal on a log scale. All 39 reflections index to pyrite and no other phases are detected. A linear least squares fit of the data gives a cubic lattice parameter of 5.41741 ± 0.00087 Å at room temperature. The background pattern is for an empty capillary tube. Small blue bars near the x-axis denote the pyrite reference peaks. (c) Typical Raman spectrum of a pyrite slab. All peaks correspond to pyrite. (d) Photograph of pyrite slabs showing a heavily stepped as-grown facet (left) and a polished facet (right). (e) 2θ–ω XRD scan on a log scale of a polished slice with (111) orientation. Small blue bars near the x-axis denote the pyrite reference peaks. (f) (111) rocking curves for a pyrite slab and a prime grade CZ-grown Si wafer. The pyrite slab shows a FWHM of 6.5 arcseconds, compared to 8.8 arcseconds for the Si wafer. Figure is reproduced from [29].

A disadvantage of the flux synthesis is that the pyrite crystals always contain macroscopic voids. These voids are clearly visible by eye upon sectioning an as-grown crystal. X-ray tomography was employed to image the voids in several as-grown crystals. 3D reconstructions show that some regions of each crystal contain localized networks of elongated and globular voids (Figure 4.2). Some of the voids open to the external surface of the crystal, while others are closed.

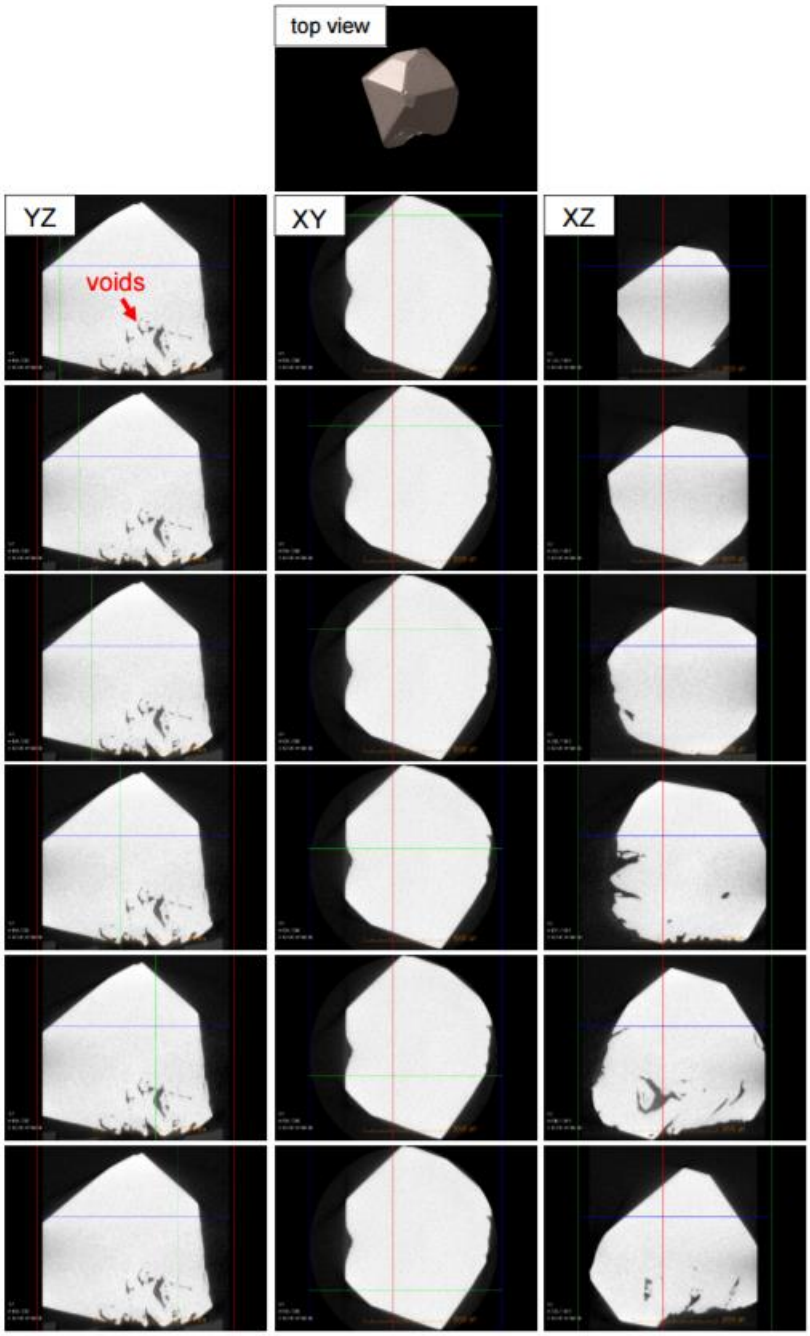

Figure 4.2: X-ray tomography images of a flux-grown pyrite crystal. (top) Top view of a 3D reconstruction. Figure is reproduced from [29].

The density of several crystals was measured by helium pycnometry. Helium pycnometry was carried out on a micro-Ultrapyc 1200e (Quantachrome Instruments). The density was measured to be 4.904(3)–4.959(3) g cm^{-3}, or 97.9–99.0% of the theoretical density of pyrite (5.011 g cm^{-3} at room temperature). Since pycnometry measures the skeletal volume (*i.e.*, the volume of the crystal plus any voids inaccessible to He), we conclude that only a relatively small fraction of the void volume is closed. Crucially, the top ∼1 mm of most crystals is completely free of voids, while the void density increases toward the bottom of the crystal (*i.e.*, where the crystal touches the crucible). All electrical and optical measurements described in this dissertation used void-free slabs to avoid potential complications from empty volume effects.

Due to the presence of the voids, a large portion of grown crystals were not usable. Hence, several methods were tried to reduce the void concentration. The summary of the tried routes is discussed here.

First, changes were made to the chemistry of growth. In normal crystals, sodium sulfide (Na_2S) is used as the flux. Attempts were made to make crystals with potassium sulfide, and also a mixture of sodium sulfide and potassium sulfide. Changes in the chemistry of the growth could potentially result in larger and void-free crystals. A mixture of K and S were chosen since they have eutectics as low as 120°C (Figure 4.3). A wide range of K and S ratios were tested. It was found that in order to obtain pyrite crystals, a high sulfur to potassium ratio is needed. When the composition of the added flux was close to K_2S_6, pyrite crystals were grown. Like the normal crystals (Na_2S as flux), a high ratio of sulfur to iron was needed as well (4.5:1); lower sulfur to iron ratios resulted in growing pyrrhotite (sulfur deficient phases). A mixture of sodium sulfide and potassium sulfide

would also yield crystals. However, neither of these alternatives routes resulted in better quality (larger and fewer voids) crystals, and thus, sodium sulfide was used as the flux for all the reported crystals in this work

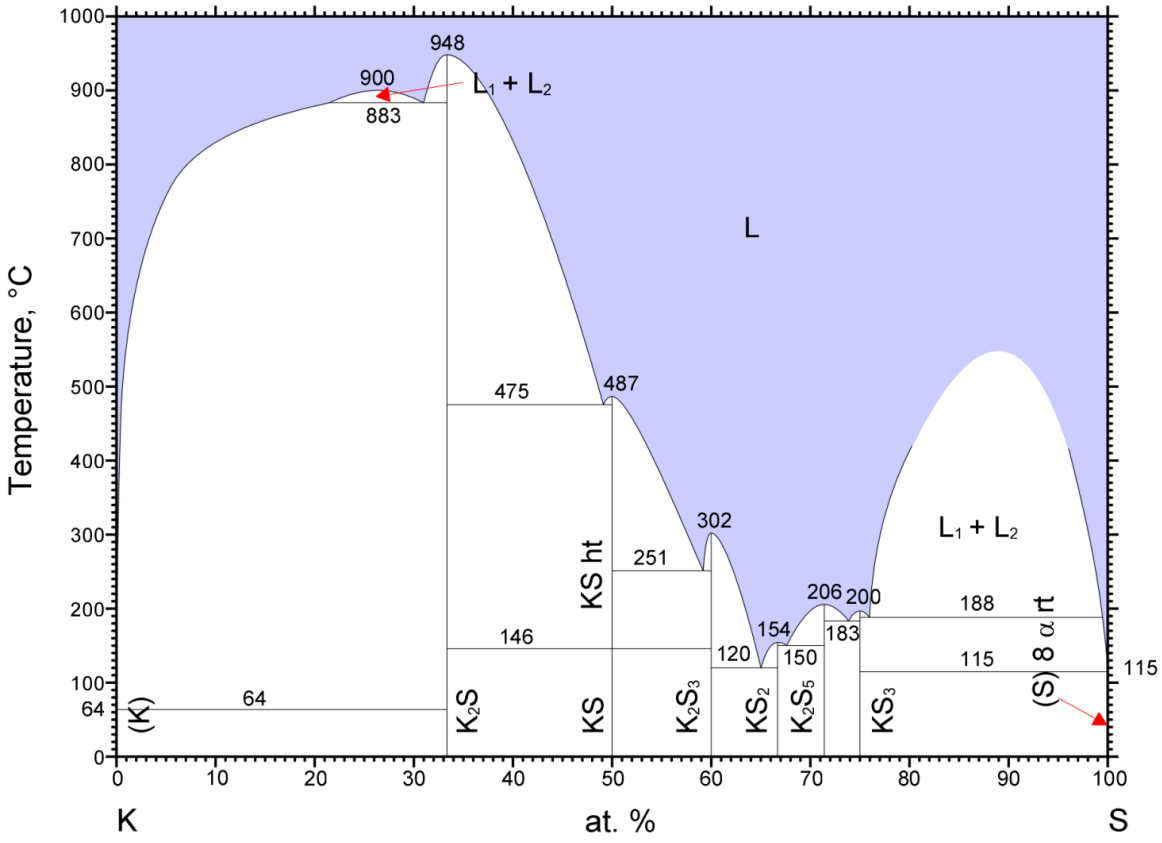

Figure 4.3: K- S phase diagram. A mixture of K and S are liquid over a wide range of compositions and have eutectics at low temperatures. Figure is adapted from [73].

Spinning the sealed quartz tubes during the growth of the crystals was the second method tested. The sealed quartz tube containing the crucible and the precursors were placed in a quartz tube that was connected to a programmable rotary motor. The setup enabled spinning of the crucible with different acceleration and deceleration speeds. Being able to spin the crucible with the

material inside it could potentially result in a more homogeneous melt, and higher quality single crystals (fewer voids). Several spinning speeds with different delay times between acceleration and deceleration were tested. Table 4.1, shows a summary of different conditions.

Table 4.1: The effect of spinning on the quality of single crystals. Acceleration and deceleration time for the reported conditions were 6 seconds. Delay time corresponds to the time between deceleration and accelerations.

	Speed (pulse/sec)	Delay	Spin Time	Outcome
1	100000	30 min	6hrs	Normal-size crystals
2	100000	30 min	36 h (whole time)	Normal-size crystals
3	100000	12 sec	36 hr (whole time)	Normal-size crystals
4	200000	12 sec	36 hr (whole time)	Very small crystals
5	150000	12 sec	36 hr (whole time)	Small + mid-size crystals
6	200000	12 sec	20 hr (till 690°C)	Small + mid-size crystals
7	200000	10 min	36 hr	Normal-size crystal
8	200000	5 min	36 hr	Small + mid-size crystals

It was concluded that the shorter the delay time, the smaller the grown crystals. Also, increasing the speed would yield smaller crystals. It was found that the small crystals (1 mm × 1 mm × 2 mm) had barely any voids, but due to their small size, they could not be used for device making

or any characterization. Other conditions that yielded normal-size crystals had the same void problem.

In conclusion, no effective route was found to decrease the fraction of voids in the crystals and increase the size of the crystals. Although spinning the melt during growth showed a great potential for reducing the fraction of voids, it could not be implemented since it reduced the size of void-free crystals substantially.

4.1.2 Elemental

The bulk elemental composition of the crystals was determined by Glow Discharge Mass Spectrometry (GDMS), Instrumental Gas Analysis (IGA), and Secondary Ion Mass Spectroscopy (SIMS), as described in section 2.5. GDMS provides a full elemental survey (Li–U) with ppb–ppm detection limits, while IGA measures gas-forming elements (O, C, N, H, S) over a wide dynamic range (ppm to percent levels). SIMS is a surface probe that samples a much smaller amount of material than either GDMS or IGA (~0.5 μg *versus* >10 mg). Table 4.2 lists all impurities detected in the crystals by the three techniques. Based on the GDMS/IGA data, the total impurity content of the crystals excluding oxygen, carbon and hydrogen is ~25 ppm, with the only elements above 1 ppm being Cr (6.4 ppm), B (6.3 ppm), Si (4.2 ppm), Na (4.2 ppm), and Cl (1.1 ppm). Chromium is a known impurity in our iron starting material, and can be eliminated by using commercial batches of iron that are free of chromium. Since the sodium was largely removed by thoroughly rinsing crushed crystals in water, we believe that sodium is present only on the surface of the

crystals (as residual flux) and not as substitutional or interstitial impurities in the pyrite lattice. SIMS data confirm this interpretation (see below). The origin of the boron, silicon, and chlorine contamination is less clear. Boron is present regardless of whether pBN or alumina crucibles are used in the syntheses, so it must originate from the Na_2S precursor or, less likely, the quartz ampoule. Silicon probably comes from the quartz. If we disregard Na, our crystals are 99.998% pure on a "metals" basis, making them the purest pyrite crystals yet reported. [55] [56] [57] [58]

Table 4.2: Elemental analysis of pyrite flux crystals by GDMS, IGA, and SIMS[a] (reproduced from [29]).

Element	GDMS/IGA concentration (ppm at.)	SIMS concentration (ppm at.)
O	1775[a]	1-4
C	533[a]	1-2
N	DL(<28)	NM
H	?[b]	(15, 52, 560)[c]
Cr	6.4	(1, 3, 82)[c]
B	6.3	NM
Si	4.2	NM
Na	4.2[a]	<0.006-0.2
Cl	1.1	0.05-0.2
Ni	0.9	NM
Ca	0.4	<0.003-0.2
Al	0.4	0.07-0.2
Mg	0.3	<0.002-0.08
P	0.1	NM
F	DL(<1)	<0.03-0.2
K	DL(<0.1)	0.0004-0.3

[a] Data for crystals grown in pBN crucibles. [b] Oxygen, carbon, and sodium are present on the crystal surface, with very little in the lattice. [c] Hydrogen could not be accurately measured by IGA. [d] Values listed for three different crystals to show variability. All unlisted elements (Li–U) were below GDMS detection limits (0.01–0.5 ppm at. for most elements). SIMS data are average bulk values (>500 nm from the crystal surface). DL = below detection limit; NM = not measured.

Although the metal levels are very low, high concentrations of oxygen (1775 ppm) and carbon (533 ppm) were detected by IGA, and we could not reliably quantify the hydrogen content by IGA

due to instrument complications from sulfur. Oxygen, carbon, and hydrogen could have important electronic effects if these elements are in the lattice rather than on the surface of the crystals. We used SIMS depth profiling to verify the concentration of oxygen, carbon, and a group of other trace elements (H, Cr, Al, F, Cl, Na, K, Mg, and Ca) in several locations on three different pyrite crystals. As seen in Figure 4.4, SIMS profiles show that the concentration of oxygen and carbon is only 1–5 ppm in the bulk of the crystals, much lower than the values determined from IGA. The higher concentration of oxygen and carbon near the surface of the crystals – which probably results mainly from surface particle contamination (unavoidable for samples prepared in non-UHV conditions) – is insufficient to reconcile the IGA and SIMS results, implying sources of oxygen/carbon that the SIMS experiments do not detect. Based on these combined data, we conclude that the oxygen and carbon contamination sits mostly on the surface of the crystals and is present in the pyrite lattice only in ppm concentrations.

SIMS also shows a substantial, sample-dependent concentration of hydrogen (15, 52, and 560 ppm in three different samples) and chromium (1, 3, and 82 ppm) in the pyrite bulk. Hydrogen is a ubiquitous impurity that may originate from our H_2-reduced iron precursor, incompletely-dried Na_2S or sulfur precursors, or several other potential sources. Hydrogen may act as an electronic dopant in pyrite. Chromium is from the iron precursor, as mentioned above. All other elements monitored by SIMS were below ~0.2 ppm, in rough agreement with GDMS results. The variation in impurity concentration from sample to sample probably reflects variations in precursor purity and sample processing, but we cannot rule out the possibility that the crystals have an inhomogeneous impurity distribution. Based on the combined GDMS, IGA, and SIMS data, we

conclude that (i) our crystals have a total lattice impurity content of ~80 ppm (assuming ~52 ppm of hydrogen on average), making them ~99.992% pure overall, (ii) hydrogen is the major extrinsic impurity, and (iii) surface particle contamination is responsible for the high levels of oxygen and carbon detected by IGA.

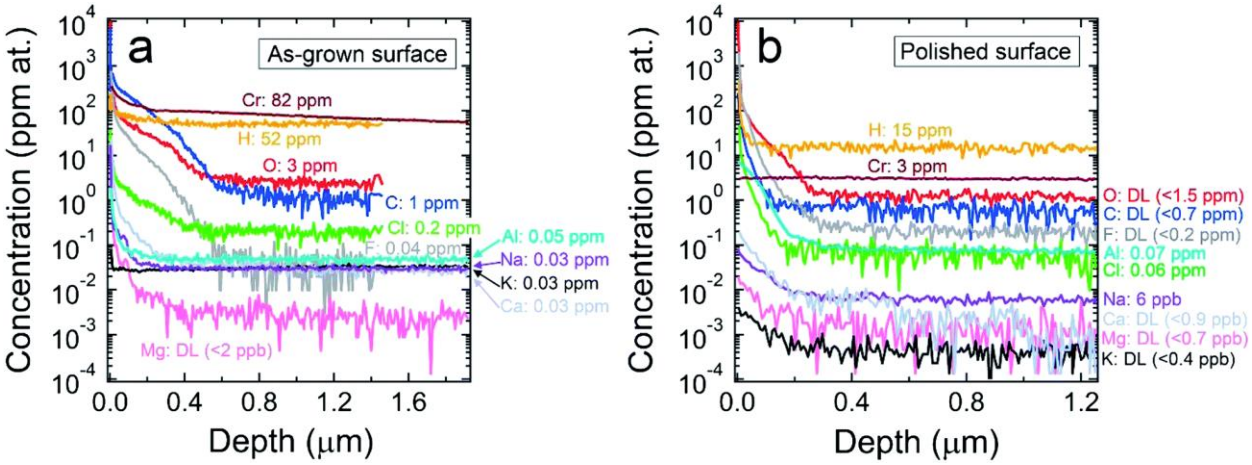

Figure 4.4: SIMS depth profiles of (a) an as-grown surface and (b) a polished surface of two different pyrite crystals. DL = below detection limit. Figure is reproduced from [29].

4.1.3 Electrical

To understand the electrical properties of the pyrite single crystals, Hall effect data were acquired, and the data was modeled by a multilayer model by Petritz. [66] Both the measurement and data modeling were carried out by Moritz Limpinsel.

Hall effect data were collected on pyrite (111) and (210) slabs in a van der Pauw geometry over a temperature range of 40–700 K. Figure 4.4 plots the conductivity σ and the absolute value of the Hall coefficient $|R_H|$ versus inverse temperature for a typical sample. The conductivity decreases by a factor of $\sim 10^8$ with decreasing temperature and shows three distinct linear

regions of progressively smaller activation energy: (I) $E_a \sim 375$ meV for $T > 500$ K; (II) $E_a \sim 163$ meV for $350\ \text{K} > T > 130$ K; (III) $E_a \sim 24$ meV for $T < 90$ K. We assign region I as the intrinsic region, where the activation energy is related to the (high-temperature) band gap of pyrite. In region II, the crystal is clearly n-type (large negative value of R_H), and transport is dominated by the ionization of donor states. Since $n \gg p$ in this extrinsic region, the Hall coefficient simplifies to $R_H = -1/ne$ and the Hall data can be used to estimate the free electron density n, mobility μ_e, donor concentration N_D, and donor energy E_D. At 300 K, $n = 5 \times 10^{15}$ cm^{-3} and $\mu_e = 245$ cm^2 V^{-1} s^{-1}. We consider two limiting cases for determining E_D and N_D from the slope of $R_H(T)$ in region II. The slope in this region corresponds to an activation energy of ∼195 meV for $n(T)$. We note that the E_a of $\sigma(T)$ is somewhat different (∼165 meV) because σ is the product of two temperature-dependent quantities, $n(T)$ and $\mu_e(T)$, while $R_H(T)$ in the unipolar region depends only on $n(T)$. If we first assume that the crystals are uncompensated ($N_A/N_D = 0$, where N_A is the concentration of acceptors), then the Fermi level is located about halfway between E_D and the conduction band edge E_C, such that $(E_C - E_D)/2 \approx 195$ meV. In this case, the donor ionization energy $E_C - E_D$ is ∼390 meV and, using the approximation $N_D \sim ne^{(E_C - E_D)/2K_BT}$, we find $N_D = 9 \times 10^{18}$ cm^{-3} (equivalent to ∼120 ppm). However, it is extremely unlikely for a compound semiconductor to be completely uncompensated. At ∼60% compensation, the Fermi level is essentially equal to the donor level, making $E_C - E_D \sim 195$ meV. In this case, the donor ionization energy determined from $R_H(T)$ is approximately 195 meV, while N_D remains unchanged. Since including compensation changes little other than the energy of the donor state, we assume zero compensation in most of the remainder of this dissertation. We believe that the donor is probably a native defect (most likely

a sulfur vacancy or vacancy cluster) since hydrogen is the only extrinsic impurity with a concentration higher than ~10^{18} cm^{-3} yet the Hall data show no clear correlation to the hydrogen concentration.

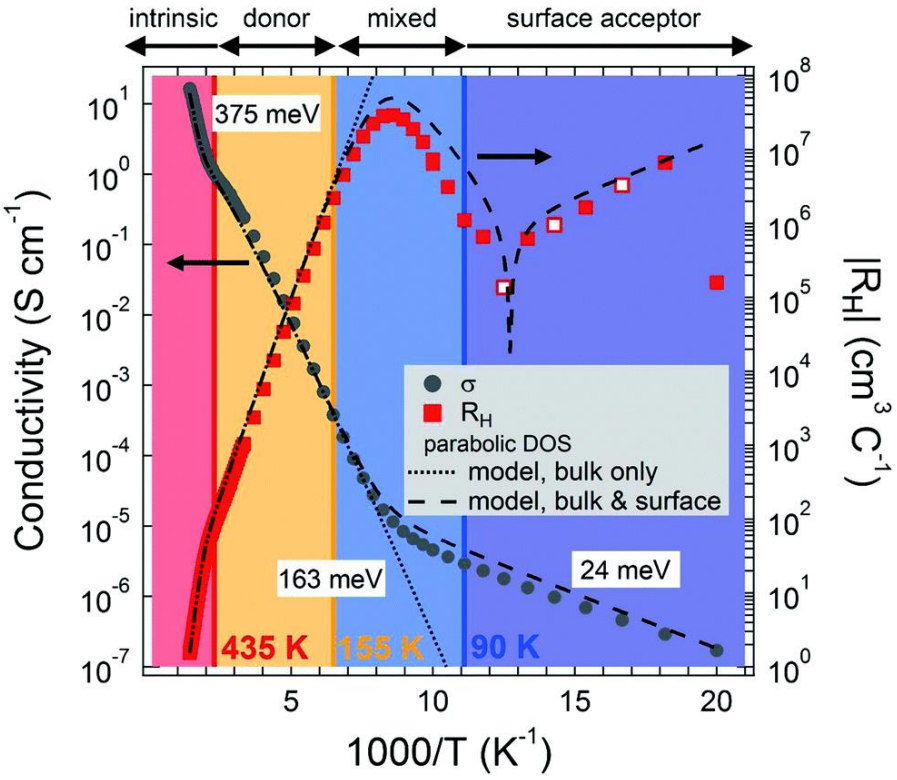

Figure 4.5: Raw Hall effect data (σ and $|R_H|$) for a pyrite (111) slab with a thickness of 1040 µm. The conductivity shows three linear regions with activation energies of 375 meV, 163 meV, and 24 meV, respectively. The Hall coefficient exhibits unusual behavior, including a minimum at ~120 K and a sign change from negative (electron dominant) to positive (hole dominant) at ~80 K. Red squares indicate negative values of R_H, while red and white squares are positive values. The sign of R_H varies at low temperature because the Hall voltage V_H is very small in this regime. The high-temperature data can be fit with a model that considers only a homogeneous crystal with a single donor (dotted traces). A three-layer model (n-type bulk plus p-type surface on each side of the crystal) is needed to fit the data over the entire temperature range (dashed traces). This fit uses the normal parabolic DOS(E) functions, the free electron approximation, and the Fermi–Dirac distribution function, assuming zero compensation of bulk and surface. Fit parameters are shown in Table 4.3. The sample is intrinsic at high temperatures (red region). With decreasing temperature, transport becomes dominated by bulk electrons (yellow), enters a transition region of mixed electron and hole conduction (blue), and then becomes dominated by surface holes as the bulk electrons are frozen out (gray). Figure is reproduced from [29].

Figure 4.6, shows the calculated mobility from the model and experimental values of mobility based on unipolar approximation. The mobility in region II varies with temperature as $T^{-2.0}$ to $T^{-2.5}$, implying that phonon scattering limits the mobility at intermediate temperatures, as it does in most high-quality single crystals. The mobility peaks at values up to 1930 $cm^2\ V^{-1}\ s^{-1}$ at ∼120 K before appearing to decrease at lower temperatures. However, as discussed below, conduction from 90–155 K is mixed between bulk electrons and surface holes, making $R_H \neq -1/ne$. As a result, the peak electron mobility in Figure 4.6 is probably underestimated, and the mobility values in this intermediate range of temperatures have no clear physical meaning.

The Hall coefficient exhibits unusual behavior at temperatures below ∼155 K. Instead of showing the expected monotonic increase in magnitude due to carrier freeze out, R_H of the pyrite samples reaches a minimum at ∼120 K, increases, and then passes through zero at ∼80 K and changes sign from negative (electron dominant) to positive (hole dominant) at lower temperatures. This sign change appears as a cusp in $|R_H(T)|$ in Figure 4.5. Such an R_H extremum and sign reversal cannot occur in a doped or compensated semiconductor away from the intrinsic region *unless* (a) the mobility of holes becomes many orders of magnitude larger than that of electrons at low temperature, (b) the mechanism of charge transport changes from band conduction to some form of hopping below ∼155 K, or (c) conduction in a p-type surface inversion layer dominates the low-temperature transport.

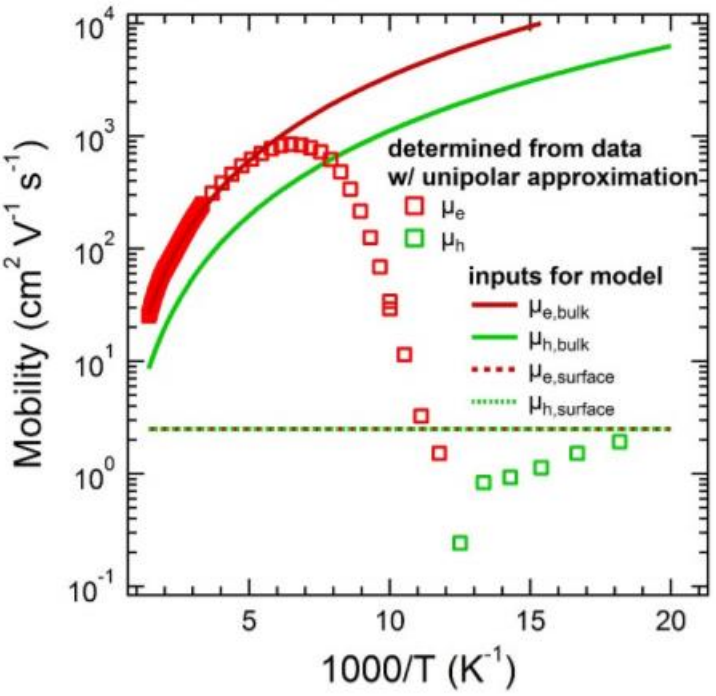

Figure 4.6: (a) Mobility as calculated from the Hall data in Figure 4.5. Assuming validity of the unipolar approximation at all temperatures [i.e., n,p = 1/|RHe|]. Note that this approximation is violated in regions of mixed electron and hole conduction (i.e., the intrinsic region and the temperature range of 80-150 K). Solid and dashed curves denote the values used to parameterize the model. These values match the data in the unipolar regions (> 150 K for electrons and < 80 K for holes). Electron mobility in the bulk, $\mu_{e,bulk}$, follows a $T^{-2.5}$ dependence at high T, as is common for phonon scattering. [74] Hole mobility in the bulk, $\mu_{h,bulk}$, is assumed to be 1/3 of $\mu_{e,bulk}$ at all T. Note that the value of $\mu_{e,bulk}$ is irrelevant at low T and $\mu_{h,bulk}$ is irrelevant at all T due to the low carrier concentrations. Thus, no assumptions about bulk mobility at low T were necessary to model the data. For example, including ionized impurity scattering at low T had no effect on the fits (as expected). Hole mobility in the surface layer, $\mu_{h,surface}$, was estimated from low T data using the unipolar approximation. We found values ranging from 0.1 to 10 cm^2 V^{-1} s^{-1} and used the best fit result of ~2 cm^2 V^{-1} s^{-1} in the model. Electron surface mobility is irrelevant due to negligible carrier concentration and was set to $\mu_{e,surface} = \mu_{h,surface}$ for simplicity. Figure is reproduced from [29]

To test premise (a), we calculated $R_H(T)$ self-consistently for widely-varying combinations of dopant density, dopant ionization energy, and carrier mobility and found that low-temperature R_H sign changes can occur only when $\mu_e(T)$ or $\mu_h(T)$ is unphysical, such as when $\mu_h(T)$ increases exponentially by many decades with decreasing temperature. We conclude that the

observed $R_H(T)$ behavior must be due to either a transition to hopping transport (premise b) or surface conduction (premise c).

We were not able to provide a firm answer to the possibility of transition to hopping (premise b) by analyzing the magnetoresistance with respect to temperature and field (see [29] for more detail). However, regardless of whether hopping occurs, the results we present below establish beyond doubt the existence of a conductive inversion layer at the surface of pyrite. The open question is then whether carriers in this surface layer move by hopping, conventional band transport, or perhaps even impurity band transport at low temperature.

We can quantitatively account for the Hall behavior of our pyrite crystals (*e.g.*, Figure 4.5) by supposing that conduction is by a p-type surface layer in parallel with the n-type bulk of the crystal. The surface layer is an inversion layer caused by large upward band bending at the surface of the crystal. The origin of this band bending is discussed below. To model the Hall data, the crystal can be thought to consist of three layers: the bulk and a surface layer on each side of the crystal. Our model follows the approach of Petritz [66], and assumes a single donor level in the bulk and a single acceptor level in the surface layer. We calculate $E_F(T)$ self-consistently from the semiconductor charge neutrality condition and then determine $n(T)$ and $p(T)$ in all layers, while the mobilities are inputs to the model parameterized from the Hall data in the unipolar regions. The dotted traces in Figure 4.5 show a simultaneous fit of the high-temperature σ and R_H data by considering only the bulk (zero compensation), without the surface layers. This fit is good at temperatures above the $|R_H|$ maximum, but of course cannot capture the unusual low-temperature behavior. Including the surface layers in the model results in a good global fit over

the entire temperature range (dashed traces). Parameters used in the fits in Figure 4.5, including estimates of the density and ionization energy of both the donor and acceptor, are listed in Table 4.3, and are physically reasonable. Using parabolic DOS(E) functions in the model results in the following typical values for the parameters: $N_{D,bulk} = 6.3 \times 10^{18}$ cm^{-3}; $E_C - E_D = 390$ meV; $E_A - E_V = 50$ meV; $d_s = 4.4$ nm; $\mu_h = 2.5$ cm^2 V^{-1} s^{-1}. The surface acceptor density $N_{A,surface}$ depends on surface preparation and varies in the range of 10^{19}–10^{21} cm^{-3}. This model provides a simple explanation for the existence of the maximum and sign reversal in $|R_H|$: bulk conduction of electrons dominates at temperatures higher than the maximum (giving $R_H < 0$), while surface conduction of holes dominates at temperatures lower than the maximum (and gives $R_H > 0$). The activation energy of σ at $T < 90$ K (*i.e.*, in region III) may correspond to the ionization of holes from a shallow surface acceptor into the valence band. At temperatures close to the $|R_H|$ maximum, bulk and surface conduction are of similar importance, giving rise to a regime of mixed transport between bulk electrons and surface holes. Spatial separation of these charge carriers is maintained by the surface electric field that defines the inversion layer. In other words, the inversion layer is to some extent electrically isolated from the n-type bulk by a depletion region. As we discuss below, the inversion layer revealed by our Hall measurements is likely the main reason that pyrite has a photovoltage much smaller than its band gap permits.

Critical additional evidence for surface conduction in an inversion layer comes from the dependence of the Hall data on sample thickness. In principle, decreasing the slab thickness should decrease the ratio of the bulk to surface layer thicknesses and change σ and R_H according to eqn. 8 and 9 in section 2.8.1. Only when surface conductivity is quite different from bulk

conductivity do we expect to affect the Hall data by changing the surface-to-volume ratio. We acquired Hall data on several pyrite slabs as a function of thickness by using mechanical polishing to progressively thin the slabs between measurements. Care was taken to prepare the surfaces in the same way for each measurement to avoid uncontrolled differences in surface morphology or chemistry that might influence the results. [29]

Table 4.3: Fit parameters used in Figure 4.5 (adapted from ref. [29])

Parameter (unit)	**Parabolic DOS**
N_D (cm^{-3})	6.3×10^{18}
$E_C - E_D$ (meV)	390
N_A (cm^{-3})	2.2×10^{20}
$E_A - E_V$ (meV)	50
$E_{gap,300\ K}$ (meV)	700
μh ($cm^2V^{-1}S^{-1}$)	2.5
d_S (nm)	4.4

Figure 4.7 presents Hall data (80–350 K) for a representative crystal at thicknesses of 820, 490, 140, and 60 μm, along with predictions from the model (dashed traces). We observe systematic changes in the low-temperature data that are in qualitative agreement with predictions from the multi-layer model. With decreasing sample thickness, the $|R_H|$ maximum shifts to higher temperatures (from 118 to 152 K in Figure 4.7) and the low-temperature σ increases by a factor of ~20 with no change in activation energy. The R_H sign reversal also occurs at progressively

higher temperatures (from 85 to 100 K). These effects are geometric: since surface layer conductance is a larger fraction of the total conductance in thinner samples, surface conduction starts to dominate R_H at higher temperatures as the crystal is thinned. Because the surface conductivity is much larger than bulk conductivity at low temperatures (for example, $\sigma_{bulk} = 6 \times 10^{-7}$ S cm^{-1} and $\sigma_{surf} = 0.53$ S cm^{-1} at 100 K), the total sample conductivity increases for thinner samples. We note that the systematic thickness dependence of $|R_H|$ and σ in Figure 4.7 is in itself sufficient evidence to prove that pyrite has a conductive surface layer. [29]

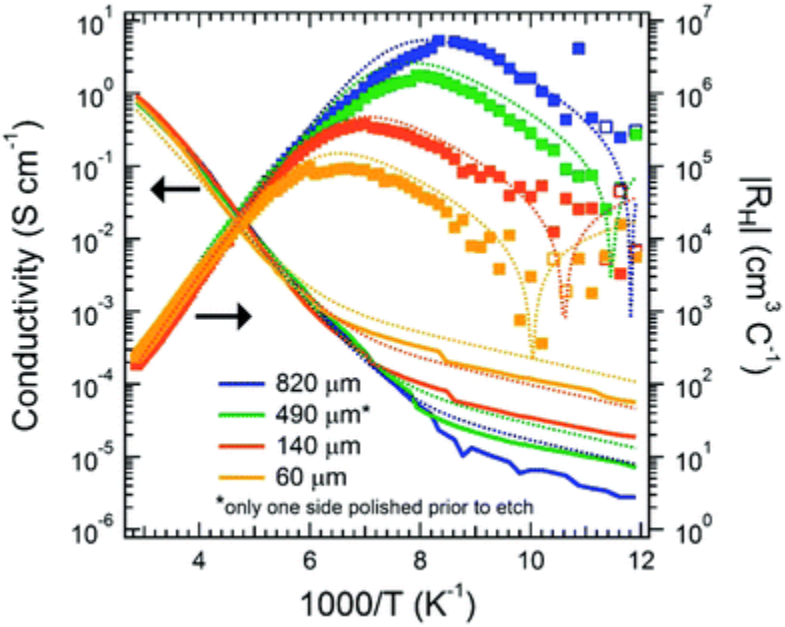

Figure 4.7: Dependence of Hall data on sample thickness. The crystal was polished on both sides and etched in piranha solution for 2 minutes prior to each measurement (except for the 490 μm data, for which only one side was freshly polished prior to piranha treatment). Dotted curves are predictions (not fits) from the multi-layer model using the sample thickness and parabolic DOS(E) functions (figure is reproduced from [29]).

The low-temperature Hall data is also sensitive to mechanical and chemical modification of the crystal surface, as expected if surface conduction dominates transport. Figure 4.8a shows how $|R_H|$ and σ change as a typical pyrite slab is cut, polished, damaged by grinding with SiC paper, and then etched in piranha solution to remove the surface damage. Polishing the as-grown slab causes a small increase in conductivity and slight shift of the $|R_H|$ maximum to higher temperature. Damaging the surface by mechanical grinding results in a much larger change of the same kind, consistent with a thicker and/or more conductive surface layer. Rocking curves show that significant lattice disorder is induced by the grinding step (Figure 4.8b). A brief piranha or nitric acid etch removes this surface damage, dramatically lowers the conductivity, and shifts the $|R_H|$ maximum to lower temperature (from 140 to 114 K), indicating a decrease in the thickness and/or conductivity of the surface layer to below that of the polished crystals. Modeling shows that the effective surface acceptor density decreases by a factor of ∼15 after piranha or nitric acid etching of polished crystals. These surface modifications have a large impact on the low-temperature data (where the surface layer dominates transport), but little impact on either σ or R_H at temperatures above ∼160 K. A chemical understanding of these changes is the goal of ongoing studies. It is possible that piranha and nitric acid treatments reduce the conductivity/thickness of the surface layer by oxidizing the surface and passivating some fraction of the surface states. The partial suppression of surface conduction by oxidizing etches raises the hope that suitable chemical treatments can be devised to control and eliminate the inversion layer at the pyrite surface. We used ultraviolet photoelectron spectroscopy (UPS) to independently confirm the existence of the inversion layer (see Experimental). Figure 4.9 shows

room-temperature He I UP spectra of a polished pyrite (111) slab acquired before and after cleaning the surface with a sequence of UV/ozone (UVO) and ammonium fluoride treatments to remove adventitious organic and oxide contamination.

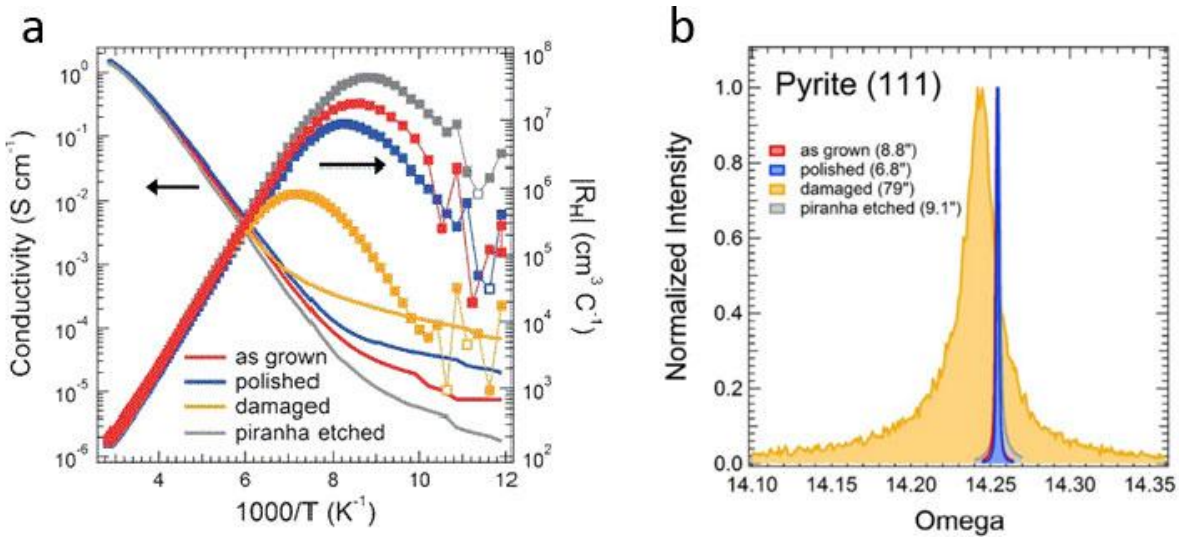

Figure 4.8: Dependence of the Hall data on gross surface modifications. (a) Data for one pyrite sample after the following sequence of surface treatments: as grown = no treatment of top surface, bottom surface rough cut with a diamond saw; polished = after polishing both sides to ∼2 nm RMS roughness; damaged = after aggressive grinding of both sides with SiC paper; piranha etched = after a 5 min etch in piranha solution. Sample thickness: 400–500 µm. (b) (111) rocking curves for a pyrite slab as a function of surface modification. FWHM values are given in the legend in units of arcseconds (figure is adapted from [29]).

Both spectra show that the Fermi level lies 0.11 ± 0.05 eV above the valence band maximum (inset Figure 4.9), *i.e.*, the surface is p-type in both cases assuming that the surface band gap is greater than ∼0.2 eV. In light of the Hall results presented in Figure 4.5, it follows that the surface must feature an inversion layer with a band diagram similar to Figure 4.10a (if the surface and bulk band gaps are the same) or similar to Figure 10b (if the surface band gap is smaller than the bulk band gap).

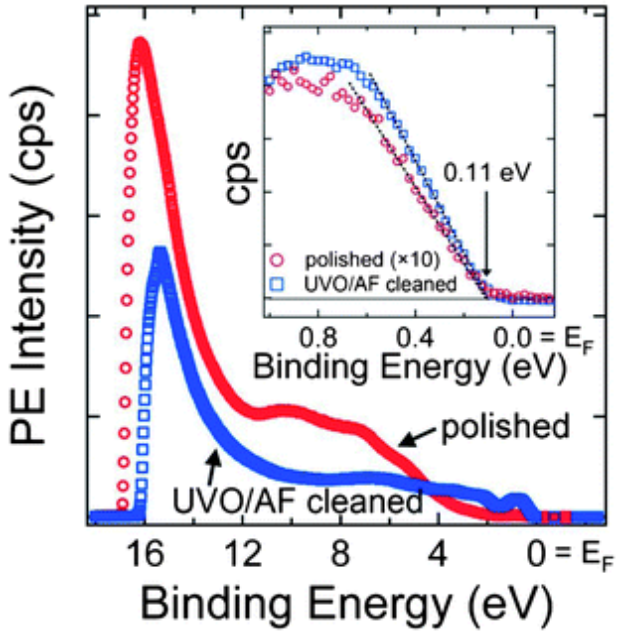

Figure 4.9: Upper valence band spectra of a polished pyrite (111) slab before and after surface cleaning by UV/ozone and aqueous NH_4F etching. Inset is a magnified view of the edge of the valence band. In both cases, $E_F - E_V \approx 0.11$ eV and the surface of the n-type crystal is p-type (figure is reproduced from [29]).

The likely existence of an inversion layer at the surface of pyrite was established twenty years ago by Bronold and co-workers using UPS measurements of vacuum-cleaved (100) single crystals. [30, 75, 76] Our UPS results reproduce this early work and, together with our Hall analysis, show that it is correct for pyrite (111), (210), and (100) surfaces. Following Bronold, we attribute the pinned Fermi level and resulting inversion layer to intrinsic surface states with energies near the valence band edge. The inversion layer probably originates from a symmetry reduction at the pyrite surface and not from contamination (*e.g.*, oxide or adsorbed organic species). Experimental evidence for the inversion layer has been overlooked in recent efforts to explain the low voltage of pyrite photocells, [71, 77] yet surface conduction in accumulation or inversion layers is quite common for semiconductors, with important examples including pyrite NiS_2, [78] and InN. [79, 80] It

has taken until now to demonstrate the importance of surface conduction in pyrite for two reasons: first, many pyrite samples are too impure to clearly see surface conduction in Hall data and, second, the few examples of unusual Hall data reported in the literature went unnoticed or were interpreted as hopping. [28]

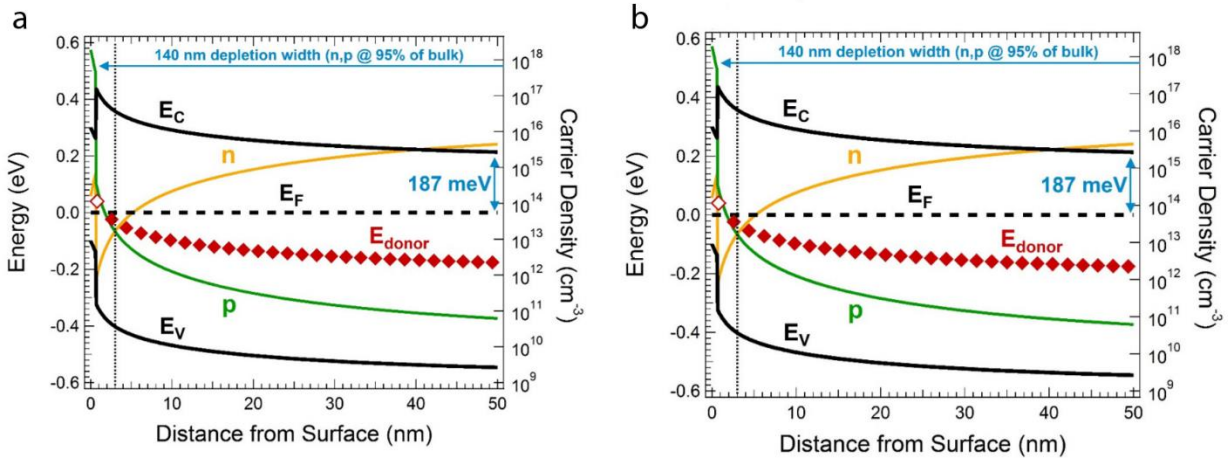

Figure 4.10: Calculated equilibrium band diagram of the pyrite surface at 300 K (see section 2.8.2) assuming zero compensation. In the bulk, E_F is located ~190 meV below the conduction band edge (consistent with $N_D = 6 \times 10^{18}$ cm^{-3} and $E_C - E_D = 390$ meV from Hall data). At the surface, E_F is pinned ~100 meV from the valence band edge (consistent with UPS data). (a) Bulk band gap and the surface bandgap are assumed to be equal ($E_g = 0.76$ eV). Equilibration of bulk with surface results in steep upward surface band bending of ~480 meV and the generation of an inversion layer ($p > n$) approximately 4.4 nm thick (denoted by the vertical dotted line). The inversion layer is separated from bulk by a depletion layer approximately 160 nm thick (defined here as $n = 0.95n_{bulk}$). Most donors in the inversion layer are ionized (open red diamonds), which augments the surface electric field and results in a narrow triangular potential barrier across which carriers can readily tunnel. Tunneling is a loss mechanism that degrades the ability of the barrier to separate charge and produce voltage. As drawn, the top ~295 mV of the barrier is lost to tunneling, leaving a maximum photovoltage of only ~178 mV for any pyrite junction. The maximum V_{OC} becomes ~340 mV if E_g is assumed to be 0.94 eV rather than 0.76 eV. (b) Assuming the presence of a narrow-gap surface layer (Eg = 0.4 eV, 0.7 nm thick). Equilibration of bulk with surface results in relatively weak band bending of ~250 meV, which represents the upper limit for the pyrite VOC. Thus, tunneling is unnecessary to explain the low VOC if a narrow-gap surface layer is present. An inversion layer (p > n) approximately 3.0 nm thick is also created (denoted by the vertical dotted line). The inversion layer is separated from bulk by a depletion layer approximately 140 nm thick (defined here as n = 0.95nbulk). Figure is adapted from [29].

The inversion layer can account for the low photovoltage of pyrite photocells. As originally argued by Bronold, the low voltage may be caused by thermionic field emission [67] through a thin triangular potential barrier at the surface of the crystal (Figure 4.10a). [30] At the pyrite surface, the iron coordination number is reduced from six to five. This symmetry reduction (distorted octahedral to square pyramidal coordination) creates iron-based surface states at energies close to the valence band edge. Fermi level equilibration of the n-type bulk with these surface states generates strong upward band bending and an inversion layer. During equilibration, donors near the surface rise above the Fermi level and are ionized, which augments the surface field and creates a thin triangular potential barrier through which majority carriers can tunnel directly or with the assistance of empty donors (Figure 4.10a). Because this leaky potential barrier is poor at separating charge, the dark current is large and the maximum V_{OC} limited to ~0.2 V (*i.e.*, the portion of the barrier not shorted by tunneling). In this picture, increasing the V_{OC} will require reducing the concentration of surface states (responsible for the inversion layer) as well as near-surface donors (responsible for the triangular tunnel barrier and, ultimately, the low V_{OC}). We estimate that reducing N_D below ~10^{17} cm^{-3} would render field emission insignificant and boost the maximum V_{OC} above 450 mV.

The inversion layer can also explain why most polycrystalline pyrite thin films show the same electrical properties – a high hole concentration, low mobility (≤1 $cm^2\ V^{-1}\ s^{-1}$), and activated transport with a small activation energy of ~25 meV – regardless of preparation method. Thin films are often dominated by surface effects due to their large surface-to-volume ratios. In the case of pyrite films, transport may be governed by surface conduction via the hole-rich

accumulation/inversion layer around each crystallite. These surface layers would form continuous networks for long-range transport through the films. Unlike pyrite single crystals, which are dominated by surface conduction only at temperatures low enough to freeze out a sufficient fraction of the bulk electrons, pyrite thin films have a large surface volume fraction and are therefore dominated by surface conduction at all temperatures. The fact that pyrite films have the same activation energy (~25 meV) and low hole mobility (≤1 $cm^2\ V^{-1}\ s^{-1}$) as single crystals in the low-temperature, surface conduction regime is strong evidence that the commonly-observed p-type electrical behavior of pyrite films is caused by conduction within a hole-rich surface layer.

Our Hall data can also be understood in terms of an inverted surface layer with a band gap that is smaller than the bulk band gap of pyrite. Several DFT studies have concluded that the low photovoltage of pyrite devices may be caused by narrowing of the "band gap" of the first three atomic layers of the pyrite surface (~0.7 nm) to less than 0.6 eV by intrinsic surface states or surface nonstoichiometry. [77, 81] Very recently, Herbert *et al.* presented scanning tunneling spectroscopy (STS) evidence that the clean pyrite (100) surface has a band gap of 0.4 ± 0.1 eV. [82] We find that a thin surface layer with a reduced band gap (E_g = 0.3–0.6 eV) has very similar electrical consequences to an inversion layer with the same band gap as bulk pyrite, namely: (i) both layers are p-type (since $E_F - E_V \approx 0.1$ eV at the surface) and responsible for the surface hole conduction we observe at low temperatures; (ii) both layers can restrict the V_{OC} to ≤200 mV, albeit by different mechanisms (compare the band diagrams in Figure 4.10a and Figure 4.10b: an inherently small built-in potential would cause the low V_{OC} in the former case, while thermionic

field emission in responsible in the latter case); (iii) the two layers have the same origin (intrinsic surface states) and so the same remedy (passivation of surface states and near-surface defects). Changing the band gap of the surface layer has a negligible effect on our Hall modeling, meaning that we cannot tell whether the band gap of the surface differs from that of the bulk on the basis of the Hall data alone. Likewise, UPS probes <1 nm into the crystal surface and the data in Figure 4.9 are consistent with any value of the surface gap greater than 0.2–0.3 eV. A combined UPS and inverse photoemission study could complement STS to definitively establish the band gap of the pyrite inversion layer.

4.1.4 Magnetic

As discussed in section 1.2, pyrite's structure can be described as $Fe^{2+}S_2^{2-}$, in which Fe^{2+} ions are located at face-centered cubic sublattice and sulfur dimers are pointing along the <111> direction. In this structure, iron has a slightly distorted octahedral ligand field, and is surrounded by six sulfur atoms, which results in diamagnetic d^6 configuration for iron. [61] However, the experimental magnetic moment associated with pyrite samples is mixed; there are reports claiming pyrite is diamagnetic, paramagnetic or even with some ferromagnetic tendencies. [83- 87] The pyrite samples that have been studied are mostly natural samples from different mines. The spread in their magnetic response has been attributed to the amount of impurities in each and the amount of surface oxidation. Iron oxide phases (e.g. hematite) or impurities (e.g. nickel) can be responsible for the observed paramagnetic or ferromagnetic behavior.

In this work, flux-grown pyrite crystals have been measured with Quantum Design MPMS 5XL system with a SQUID detector in fields up to 5 Tesla and temperatures down to 2 K. Pyrite samples (crushed powder or in the single crystal form) were placed in plastic capsules, and then placed in a plastic straw. The straw was then inserted in the SQUID. The sample holder (plastic capsule and the plastic straw) only shows very weak diamagnetic response and cannot affect the signal from the sample.

To ensure that the measurements are accurate, a standard sample was measured. Palladium (Pd) was chosen as a reference sample since its molar susceptibility is well known. Figure 4.11, shows the magnetic response and the paramagnetic susceptibility of the reference sample. The paramagnetic susceptibility of the standard matches the reported values with less than 0.5% error.

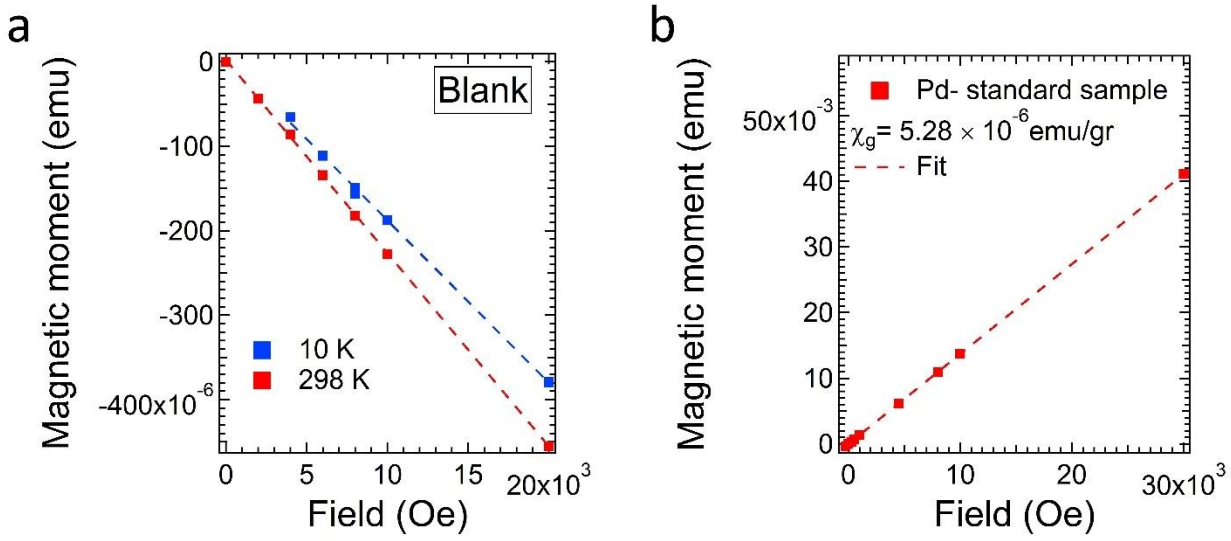

Figure 4.11: Magnetic response from the blank and the reference sample. (a) Blank (plastic sample holder without any sample) only shows a very weak diamagnetic response at all temperatures. (b) Magnetic response and the calculated mass susceptibility of the reference sample.

Figure 4.12 shows the magnetic response from a flux-grown pyrite crystal. There are three temperature regions. First, the sample shows a dominant diamagnetic response up to ~30 K (Figure 4.12). As the temperature goes below 30 K, the sample enters a mixed magnetization range. In this region, the amount of diamagnetic response and paramagnetic response becomes comparable to each other. Therefore, the SQUID response cannot be fully trusted. Lastly, the sample shows a dominant paramagnetic response at 2 K. It has to be noted that paramagnetic susceptibility increases by decreasing temperature, while diamagnetic susceptibility barely changes with temperature. This is the reason that the dominant paramagnetic region can be observed at very low temperatures.

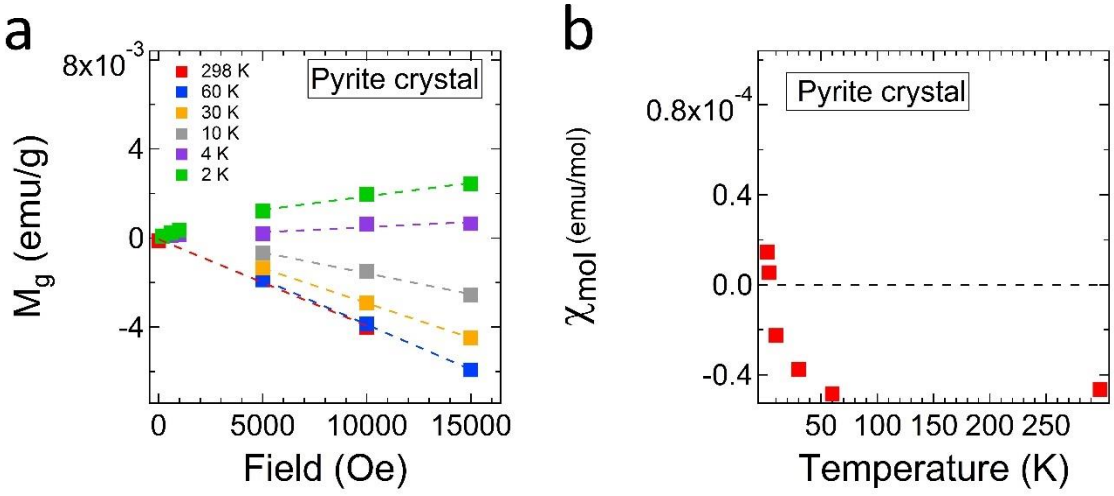

Figure 4.12: Magnetic response of a flux-grown pyrite single crystal. (a) Mass magnetization at different temperatures. As the temperature goes down, the sample enters a region of mixed magnetization (diamagnetism and paramagnetism), at 2 K sample only shows a paramagnetic response with a positive molar susceptibility (dotted line = fits). (b) Molar susceptibility vs. temperature. Molar susceptibility is calculated based on the fits to the M(H) curves in (a).

As mentioned, pyrite is supposed to be diamagnetic due to its electron configuration. Moreover, the flux-grown pyrite crystal has low amounts of impurities that cannot be responsible for the

observed paramagnetic response. Therefore, the surface of pyrite (due to termination of bonds) and surface oxidation can be responsible for the observed paramagnetism. To test this hypothesis, pyrite single crystals and crushed powders of pyrite (made from single crystals) were measured at different times after air exposure (figure 4.13).

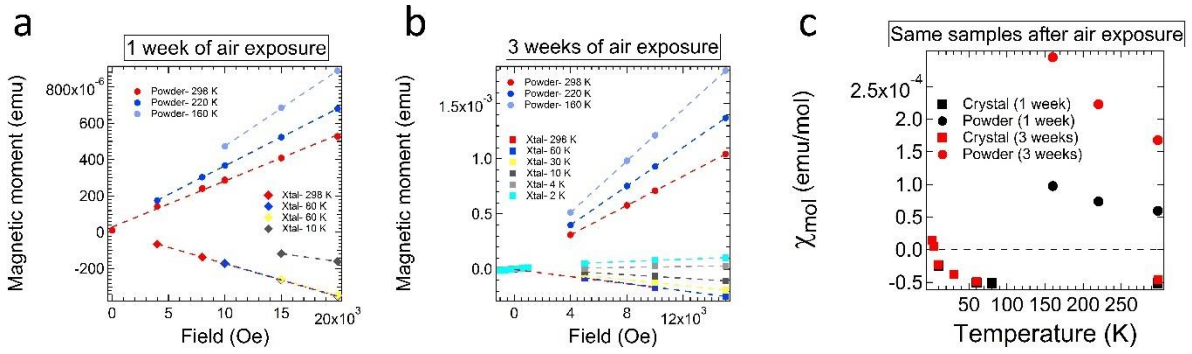

Figure 4.13: Effect of air exposure and powderization. Magnetic response of the same pyrite crystal and the same crushed powder of pyrite (from a crystal) with (a) 1 week of air exposure, (b) 3 weeks of air exposure. (c) Calculated molar susceptibility based on the fits (dotted lines) in (a) and (b).

As shown in Figure 4.13, the paramagnetic part of the magnetic response increases as the samples (crystal or powder) are exposed to air. The formation of iron oxide phases, which are known to be paramagnetic materials, is responsible for this behavior. Also, it was found that powders usually have a larger positive paramagnetic susceptibility. It is believed that a magnetic moment is associated with pyrite surfaces due to broken bonds. [81] Therefore, since powders have a larger surface to volume ratios than crystals, a higher paramagnetic response is expected for them.

In conclusion, pyrite is indeed a diamagnetic material. The reported paramagnetism or ferromagnetism is due to the type of pyrite samples that have been analyzed. [86] Natural pyrite

crystals have transition metal impurities that are paramagnetic. Moreover, surface oxidation and broken surface bonds will result in positive magnetic susceptibility as well. The need to understand the true magnetic nature of our flux-grown pyrite crystals was vital to this study. We used MPMS to look at the magnetic properties of doped pyrite crystals to understand the spin state of the doped elements (will be discussed in Chapter 5).

4.1.5 Optical

Spectroscopic Ellipsometry (SE) was used to determine the refractive index (n) and the extinction coefficient (k) for pyrite single crystals. Our group had measured the optical constants of a natural pyrite crystal before. [88] Here a flux-grown pyrite single crystal was measured. The measurements were done by Dr. Sukgeon Choi at NREL and Dr. Nina Hong at J.A. Woollam Application Laboratory. A double-side polished (DSP) silicon sample was also measured with the pyrite sample as a reference. The optical constants of two bulk samples were measured using a J.A. Woollam IR-VASE and VUV-VASE spectroscopic ellipsometer over the wavelength range of 0.14-30 μm (0.041-8.86 eV).

Figure 4.14 shows n and k measured from the natural pyrite crystal [88] and the synthetic flux-grown pyrite crystals. Both spectra are in a very good agreement with each other. The main use of the n and K values in this work was to calculate the reflectance values from the surface of pyrite. Reflectance (R) is needed to calculate the absorption coefficient (α) of the samples. Absorbance (extinction) of crystals in the transmission geometry is the parameter that we can

experimentally measure with the available instruments (FTIR and UV-Vis) in our laboratory. Due to the small size of flux-grown pyrite crystals, we were not able to use the integrating sphere of the UV-Vis to measure the reflectance separately. To calculate the absorption coefficient (α) of the samples from the measured extinction ($extinction = Log\left(\frac{1}{T}\right)$), the total transmission coefficient (T) (with multiple internal reflection) equation (below) should be solved for α. The reflection coefficient (R) needed in the transmission equation, is calculated based on the n and k values from SE. [89]

$T = \frac{(1-R)^2 \exp(-\alpha x)}{1-R^2 \exp(-2\alpha x)}$, R = reflection coefficient, x = thickness

$$R = \frac{(n-1)^2 + k^2}{(n+1)^2 + k^2}$$

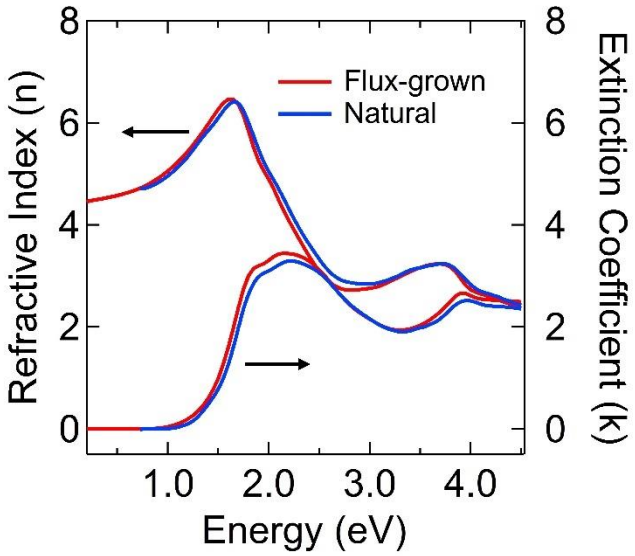

Figure 4.14: Optical constants (n and K) for natural and flux-grown pyrite crystals.

To make sure our method of calculating optical properties (transmittance, reflectance, absorptance, and extinction) from n and K is correct, a 330 μm thick DSP silicon sample was measured with both SE and UV-Vis. Then the experimental transmittance (T) and reflectance (R) spectra were compared to the calculated T and R spectra from n and k (Figure 4.14). The equations (other than T and R) that were used for calculations are listed below. (Unlike pyrite samples, the Si sample was big enough and we could use the integrating sphere in our UV-Vis system to measure R independently.)

$$\alpha = \frac{4\pi k}{\lambda}$$

$$R_t = R + \frac{(1-R)^2 \times R}{\exp(2\alpha x) - R^2}$$

$$A + T + R_t = 1$$

$$Extinction = Log\left(\frac{1}{T}\right)$$

α = absorption coefficient, k = extinction coefficient, λ = wavelength, R_t = Total reflectance (multiple internal reflections), R = reflection coefficient, x = thickness, A = total absorptance, T = total transmittance

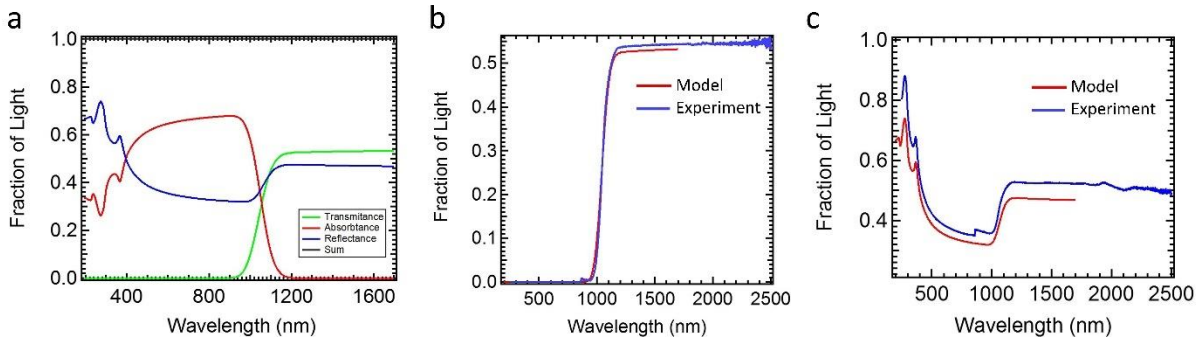

Figure 4.15: Optical properties of a 330 μm DSP Si sample. (a) Calculated transmittance, reflectance, and absorptance from n and K. (b) Comparison of calculated transmittance (model), and the measured transmittance with UV-Vis. (c) Comparison of calculated reflectance (model), and the measured reflectance with UV-Vis. Reflectance was measured by the 65 mm integrating sphere.

The experimental and calculated spectra are in good agreement for the Si sample. Figure 4.15 shows the calculated optical parameters for a pyrite crystal based on the optical constants from SE. The baseline of extinction in energies below the bandgap of pyrite is ~0.4, which is mostly due to the reflection from the surface. Since in the SE setup, the beam size was slightly bigger than the flux-grown pyrite sample, and the fact that inherently reflective SE is not very sensitive to k values, the absorbance values below the bandgap of the sample were not accurate. Therefore, throughout this work, the optical constants from the natural crystal were used to calculate R and α. Transmission SE measurement would yield better results for the small flux-grown crystal (in progress).

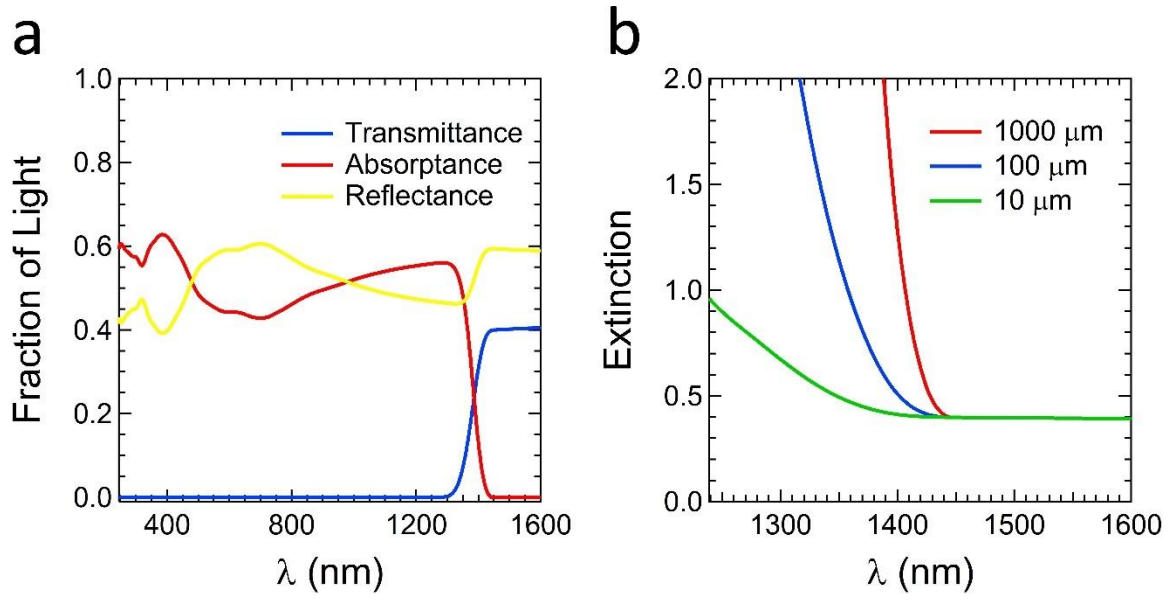

Figure 4.16: Calculated optical properties of pyrite based on measured optical constants (n and K). (a) Calculated total transmittance, reflectance, and absorptance for a 100 μm thick pyrite single crystal. (b) Calculated extinction for pyrite single crystals with different thicknesses.

Optical properties of flux-grown pyrite crystals are measured with FTIR. An XT-KBr beam splitter and a DlaTGS detector were used in the mid-IR range (0.05-1.23 eV), and a Solid-Substrate beam splitter and a Poly(ethylene) detector were used in the far-IR range (0.006-0.087 eV). A nitrogen cooled or a helium cooled cryostat were used alongside the FTIR to measure absorbance at different temperatures. The optical extinction spectra (0.01-1.0 eV) of flux-grown crystals as a function of temperature (10-340 K) and crystal thickness were measured. The goals of the measurements were to quantify the optical bandgap, quantify the amount of sub-gap absorption, and for the identification and quantification of any present gap states. Figure 4.17 shows a summary of typical absorbance spectra of un-doped pyrite crystals in the mid-IR energy range. In Figure 4.17b, the calculated absorption coefficient is presented. Pyrite crystals start to absorb

around 0.8-0.95 eV (bandgap of pyrite). The sub-bandgap absorption is very close to the calculated absorption. By correlating extinction with crystal thickness, it is apparent that the baseline of bulk sub-gap absorption coefficient is very small. No apparent thickness dependence of the sub-gap absorption was observed. The larger-than-predicted sub-gap baseline extinction that we observe (0.5-0.6) likely results from light scattering off voids present in the slabs, quality of surface polishing, and/or free carrier absorption by holes in the surface inversion layer (Figure 4.17 c and d).

Although it is possible to calculate temperature-dependent optical bandgap of pyrite based on the FTIR optical absorption spectra, we used UV-Vis measure optical absorption spectra. UV-Vis can better probe the band edge of pyrite and detect higher absorption values before its detector becomes saturated. The measurement was carried out by Jason Tolentino (graduate student at Law Lab). [29]

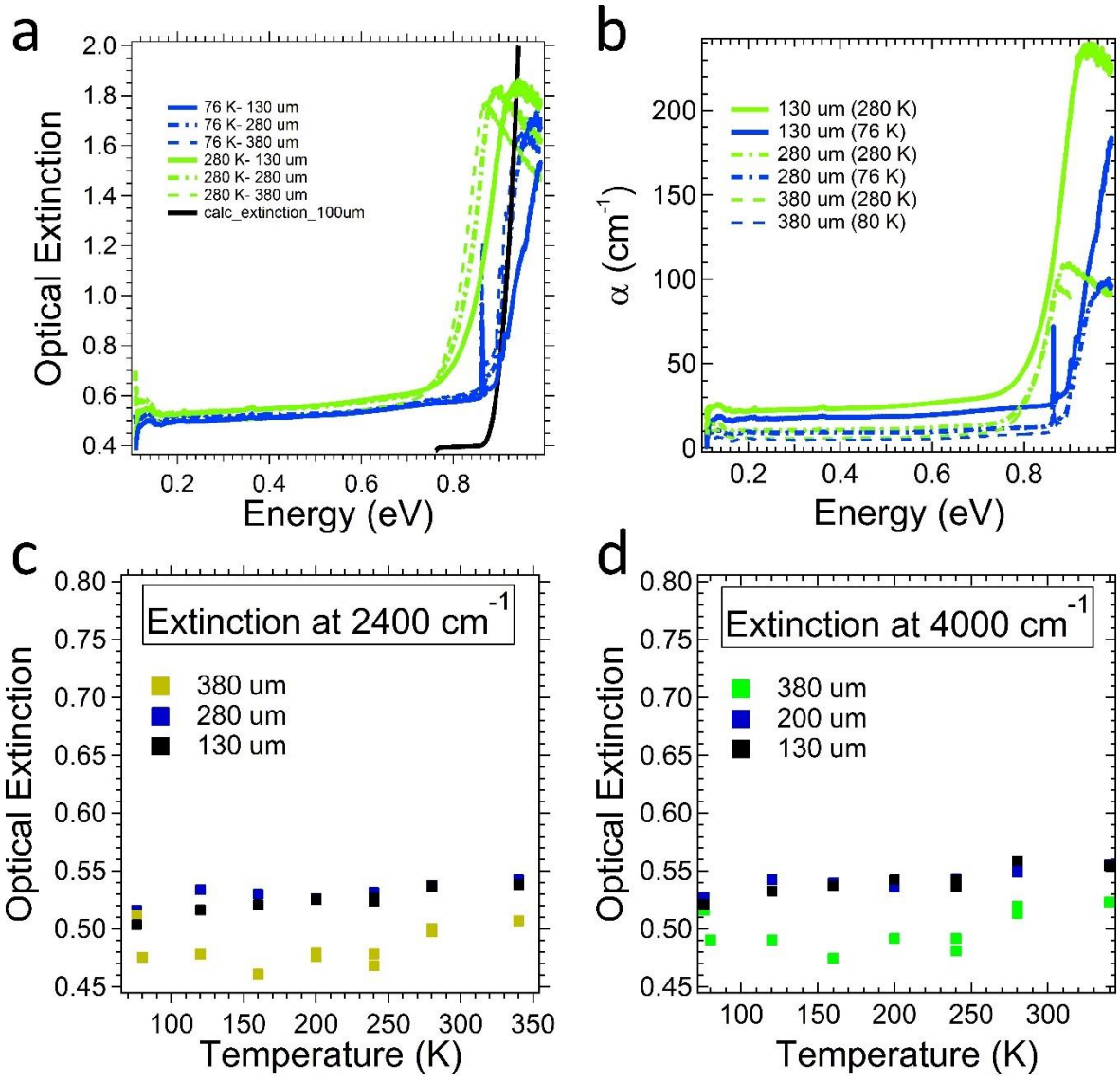

Figure 4.17: Mid-IR optical absorbance of flux-grown pyrite crystals. The measured slabs were fine polished (the same slab was measured after each round of polishing and thickness reduction). (a) Optical extinction spectra of fine polished pyrite slabs with different thicknesses at 280 K and 80 K. (b) The calculated absorption coefficient based on the extinction spectra. (c) & (d) Extinction values at 2400 cm^{-1} and 4000 cm^{-1} between 76 K to 340 K. No apparent thickness dependence of sub-gap absorption was observed.

The temperature dependence of E_g was determined by measuring the optical gap of thin polished pyrite crystals from 80 to 440 K using transmission spectroscopy. Figure 4.18 shows the

raw extinction spectra as well as the optical gap extracted by linear extrapolation of the absorption coefficient curve to its intersection with the *x*-axis. Tauc plots – which presume parabolic bands – give the same $E_g(T)$ values to within 50 meV. We find that the optical gap decreases from 1.00 eV at 80 K to 0.94 eV at 300 K and 0.86 eV at 440 K (the highest temperature possible with our equipment). Our $E_g(T)$ curve is in good agreement with several previous reports, [68, 90] particularly the work of Karguppikar and Vedeshwar. [69] Although the magnitude of E_g may be overestimated by this optical method, the temperature dependence of E_g should be reliable. [29]

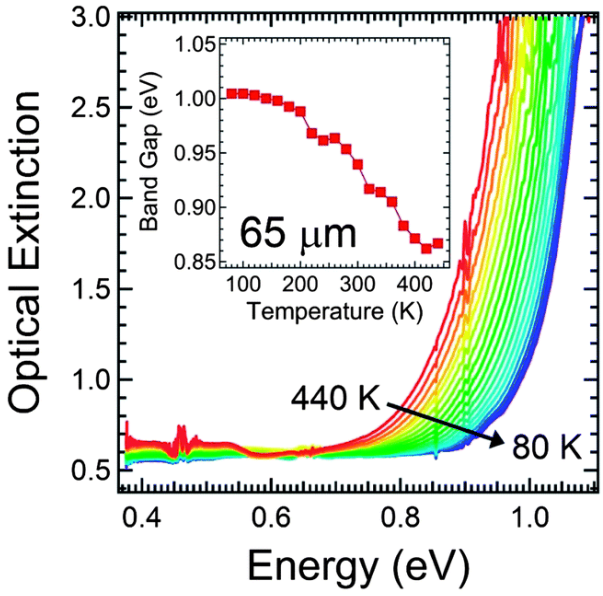

Figure 4.18: Optical extinction spectra of a 65 μm thick pyrite crystal as a function of temperature (80–440 K). Inset is a plot of Eg versus temperature as determined by linear extrapolation of the absorption coefficient data after correcting for dispersion of the refractive index. If Tauc plots are used instead, E_g is about 50 mV higher (lower) for the direct (indirect) Tauc plot, while the temperature dependence of E_g is unaffected. Figure is reproduced from [29].

Figure 4.19 shows the optical absorption spectra of fine polished pyrite crystals in the far-IR energy range (10-70 meV). Pyrite is very absorbing in this energy range since the phonon

absorption lines are all present here. Based on group theory calculation, pyrite has 5 IR phonon lines (0.0344, 0.036, 0.0425, 0.0386, 0.0534 eV). [91] Three peaks were observed in the measurements at the predicted energy range, two of the peaks were broad and included the other expected phonon lines. Pyrite slabs were extremely absorbing in this energy range, and the slabs needed to be very thin to be able to observe the peaks (< 100 μm). The lower present energy peaks (< 0.03 eV) are artifacts due to the measurement. In general, measuring slabs in the far-IR range was challenging. To maximize the signal, samples needed to be very thin and the measurement had to be carried out at very slow optical velocities which caused the formation of low energy artifacts.

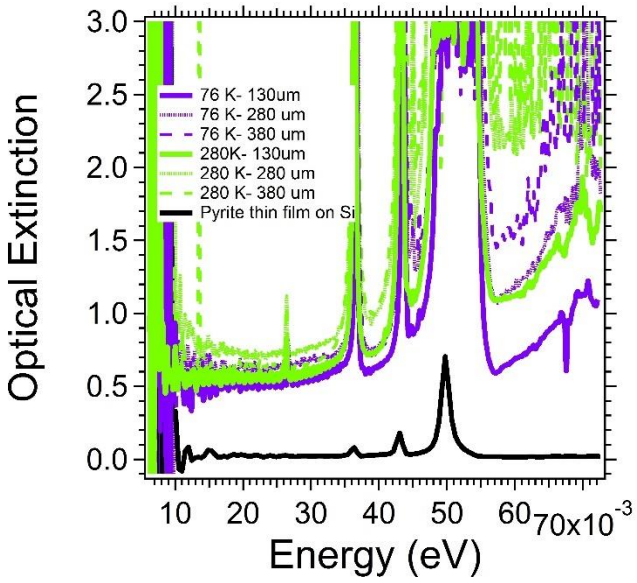

Figure 4.19: Optical extinction spectra in far-IR energy range. Fine polished pyrite crystals were measured at different thicknesses and temperatures. Optical phonon lines are observed; the same lines were observed in pyrite thin films (black spectrum).

Certain unknown features were observed in both optical extinction spectra in mid-IR and far-IR. First, four high energy absorption peaks start to appear as the temperature goes below 160°C (Figure 4.20). The peak area increases as the temperature decreases (main peak at 0.864 eV). These high energy peaks have a thickness dependence. Their peak area decreases as the thickness of the crystal decreases, suggesting that the peaks are bulk features. The formation of the peaks at high energies close to the band edge suggests that they can be excitonic features. Free excitons are mobile pairs, and they can move in the crystal. Exciton will show up near the band edge of semiconductors in absorption experiments. In indirect semiconductors, phonons will have to participate in the absorption of an exciton to conserve the momentum. Free excitons will form at photon energies based on the following equation: [89]

$h\nu = E_g - E_x \pm E_p$

E_x is the binding energy of a free exciton, and E_P is the phonon energy. More than one phonon can participate in the transition. The binding energy or the ionization of such a pair is calculated as below:

$$E_x = \frac{-m_r^* q^4}{2h^2 \varepsilon^2} \frac{1}{n^2}$$

n is the different exciton states, and m_r* is the reduced mass. Reduced mass is related to the effective masses of electron and holes ($1/ m_r^* = 1/m_e^* + 1/m_h^*$). [89] The free exciton binding energy for pyrite is around 11.3-13.6 meV. Out of the four observed high energy peaks (0.864 eV, 0.873 eV, 0.902 eV, and 0.914 eV), the last two peaks (0.902 eV and 0.914 eV) can potentially be free exciton peaks if we assume several phonons participated in the transitions. However, the first two peaks (0.864 eV and 0.873 eV) can't be due to free excitons. The ionization energy of

such features is larger than the free exciton binding energy by assuming any combination of phonon energies. However, they might be due to bound excitons. Any impurity in a crystal may cause the formation of bound excitons. Free excitons will form bound excitons by binding to shallow impurities. Isoelectronic traps can also bound excitons. Isoelectronic traps are centers in which a foreign atom with the same number of valence electrons replaces a host atom. Nitrogen in GaP is an isoelectronic trap. [92] In both cases, the exciton peaks will form at energies close to the absorption edge, and their binding energy is dependent on the impurity center. The binding energy of bound excitons is usually slightly higher than the binding energy of free excitons. The intensity of peaks from bound excitons in both cases is dependent on the density of the defect that they are bound too. This dependence plays a major factor in the identification of bound excitons. [89] These peaks can be bound excitons and have higher ionization energies than free excitons. In that case, the optical transition is dependent on the density of the centers that they are bound to. The centers can be native defects in pyrite or impurity elements. Yang et al., [90] proposed that the transitions are due to Cr. To test this theory, pyrite crystals were doped with different amounts of Cr (details of doping in Chapter 5), but no increase in the absorption peaks was observed. Doping with Co, Ni, and oxygen did not result in the increase of the optical absorption either. Nor did annealing in the sulfur atmosphere for a long time or changing the growth condition (efforts to change the density of native defects). The origin of these peaks remains unknown. Hydrogen and carbon, as two elements that can be present in the pyrite crystals, may be the centers responsible for these optical transitions and can be tested for in the future.

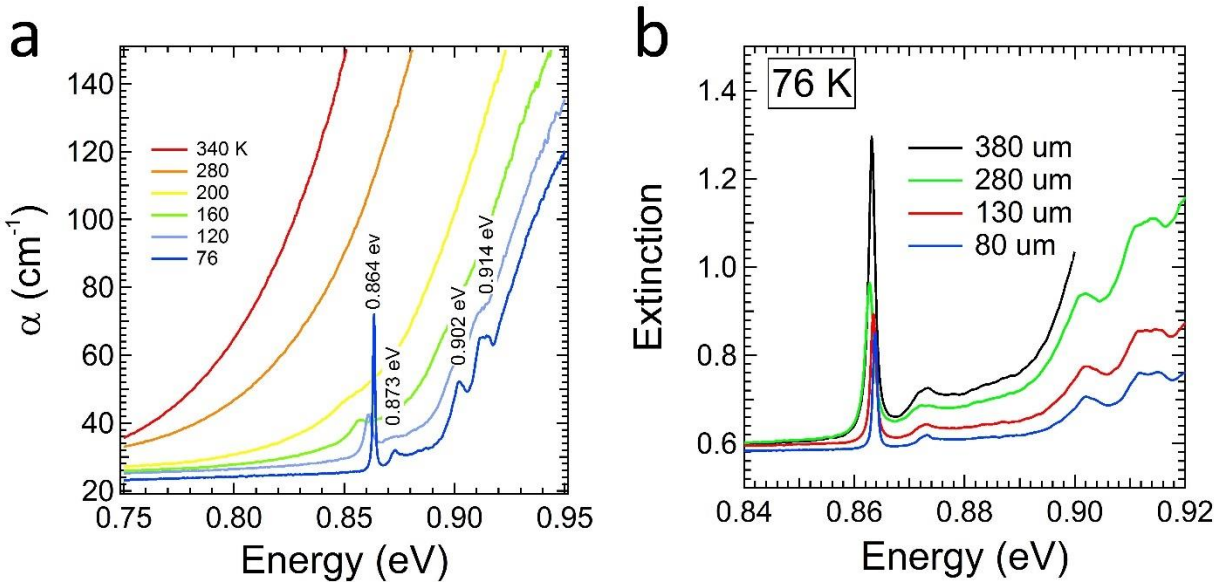

Figure 4.20: High-energy optical transitions in pyrite. (a) Calculated absorption coefficient of a fine polished pyrite slab (130 μm thick) at different temperatures. Sets of peaks start to form as the temperature goes down. The peaks track the band edge of pyrite and become sharper with the decreasing temperature. (b) Optical extinction spectra of the high energy region of a same crystal with different thicknesses at 76 K. The peak area decreases as the thickness decreases, indicating that the features are bulk features. The spectra are offset for clarity and comparison.

The second unknown optical transition features are the small peaks that are present at 0.13 eV, 0.18 eV, and 0.20 eV (Figure 4.21). The peaks were reported on the CVT-grown pyrite single crystals as well. [57] These peaks are also due to bulk features since their peak area decreases with decreasing thickness (figure 4.21b). The transition energy of the peaks does not correspond to the ionization energy of bulk donor state in pyrite either (see Section 4.1.3).

Figure 4.22 shows the last set of unknown peaks that are present in the far-IR energy range (0.6-0.9 eV). These peaks are also due to bulk features. They can only be distinguished from each other in slabs with very low thicknesses (< 100 μm), otherwise they are highly absorbing (Figure 4.19).

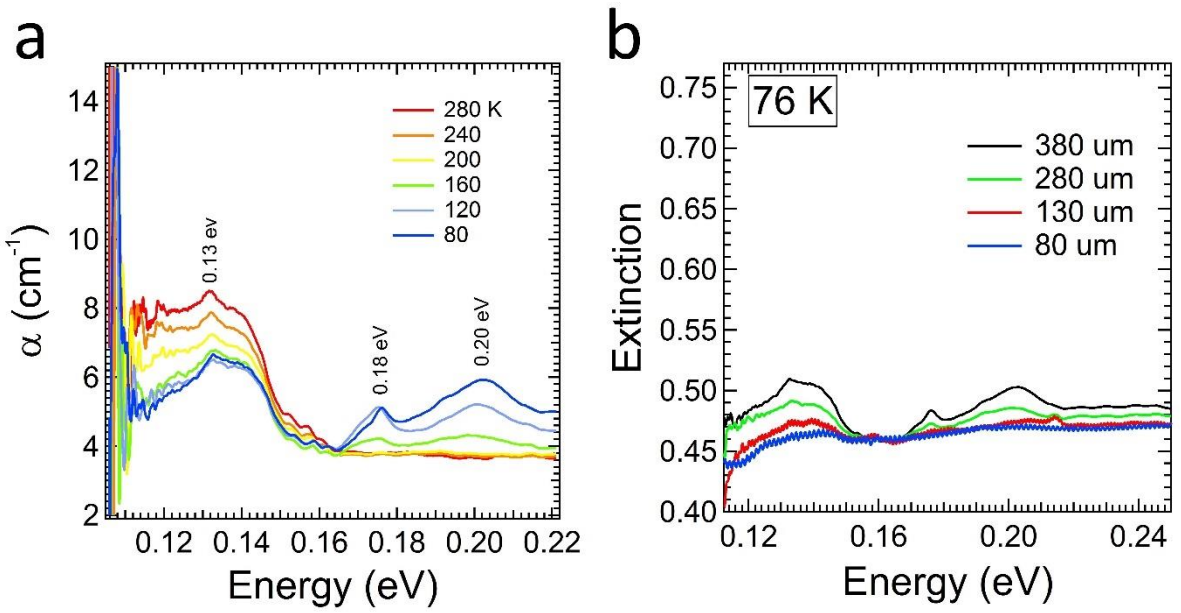

Figure 4.21: Low energy optical transitions in pyrite. (a) Calculated absorption coefficient of a fine polished pyrite slab (380 μm thick) at different temperatures. 0.18 eV and 0.20 eV peaks are barely identifiable in thin samples (< 150 μm). (b) Optical extinction spectra of the same crystal with different thicknesses at 76 K. The peak area decreases as the thickness decreases, indicating that the features are bulk features. The spectra are offset for clarity and comparison.

These features are not observed in our reflective SE measurements, nor have they been reported elsewhere. The calculated extinction spectrum of an 80 μm pyrite slab based on the optical constants from the SE measurement is shown in Figure 4.22 (dotted black line). Although the calculation captures the phonon absorption lines perfectly, it does not capture these peaks. The peaks could potentially be due to surface contamination from the present hydrocarbons in the cryostat, but systematic checks proved that not to be true as well. They may be due to optical transitions involving shallow donor or acceptors, but their origin continues to remain unknown. In the future, single crystals of pyrite with higher elemental purity are needed to be able to identify whether the peaks are due to impurity states or native defect states.

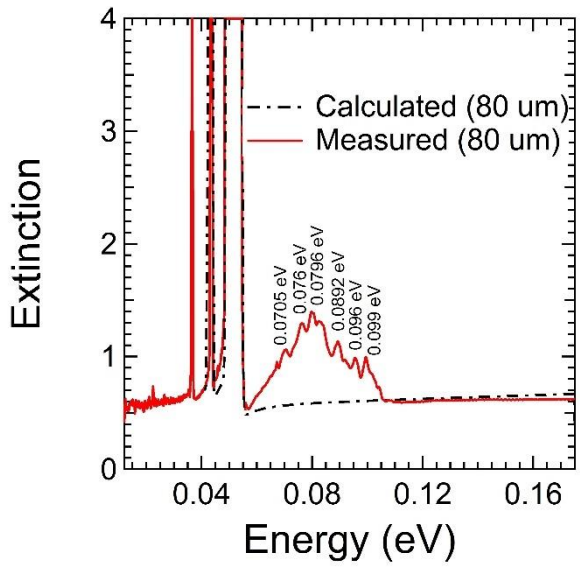

Figure 4.22: Unknown absorption peaks in far-IR energy region. The measured spectrum is from a fine polished 80 μm thick pyrite slab at 80 K. The peaks were only distinguishable in thin slabs. The calculated spectrum is based on the reflective SE measurement, which captures the IR phonon modes in pyrite but fails to capture these peaks.

4.2 Changing the donor density

It was discussed in Section 4.1.3 how the thermionic field emission at the surface of pyrite could limit the V_{OC} in pyrite devices, and increasing the V_{OC} would require reducing the concentration of near-surface donors (responsible for the triangular tunnel barrier and, ultimately, the low V_{OC}). Therefore, different ways to potentially change the donor density were tested. The importance of the purity of the precursors was discovered in the early stages of crystal growth. Using 99% (2N) pure iron and sulfur precursors instead of 99.999% (5N) pure precursors will result in doping of the single crystals and differences in electrical properties (see figure 4.23).

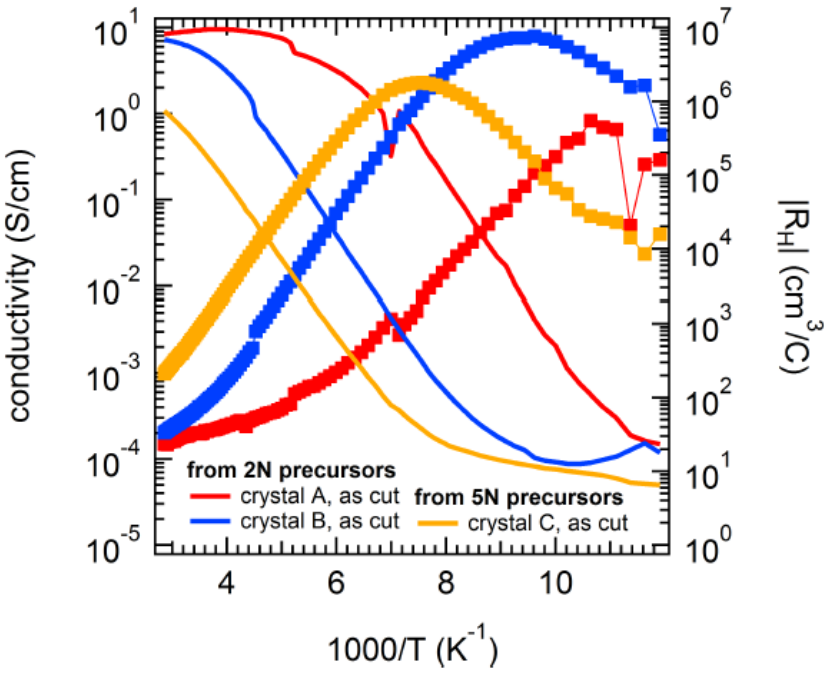

Figure 4.23: The effect of the precursor's purity on the electrical properties of flux-grown single crystals. Low purity (2N) precursors result in unintentional doping and increase the bulk donor density of the crystals. Figure is adapted from [65].

Throughout this work, the highest available pure precursors have been used, and it is believed that the observed bulk donor density is not related to impurities present in the crystals. Native defects (e.g., sulfur vacancies) can be responsible for the high concentration of the bulk donors (~10^{19} cm^{-3}). The high bulk donor concentration was calculated based on numerical modeling of Hall coefficient and conductivity data, and is enough to cause extreme upward surface band bending and a sharp triangular potential barrier across which electrons can readily tunnel, thereby degrading V_{OC}. The responsible (native) donor concentration could be substantially reduced by growing the crystals more slowly and closer to equilibrium conditions.

To test this hypothesis, we grew crystals by slowly cooling Fe-S-Na melts over ten days (instead of 1 as explained in Section 2.1.2). The "slow-cooled (slow-grown)" and standard crystals are

indistinguishable by X-ray diffraction, magnetic measurements, and elemental analysis, with both types of crystals seemingly phase pure, elementally pure, and of high structural perfection.

The phase purity of the crystals was checked with synchrotron XRD (Figure 4.24). Both crystals are phase pure pyrite with identical XRD pattern.

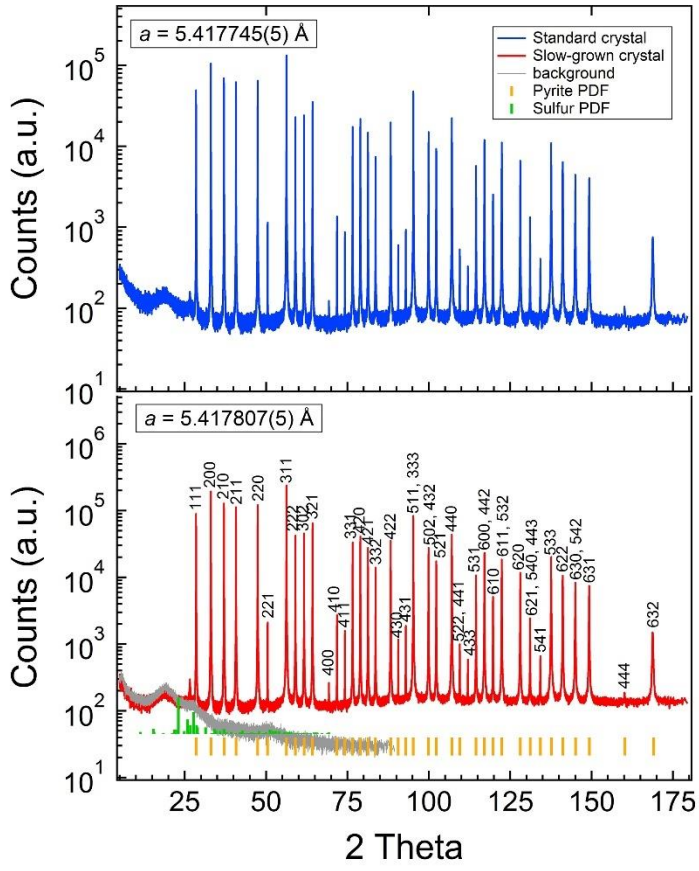

Figure 4.24: Synchrotron XRD pattern of powdered standard and slow-grown crystals. All peaks are indexed to pyrite. The unindexed peak at 26.6° present in both patterns is a sodium containing phase that comes from the flux and hasn't been completely washed away.

Rocking curve measurement was used to check for structural quality. All the measured slabs had (111) orientation with very narrow FWHM, indicating high crystalline quality (Figure 4.25).

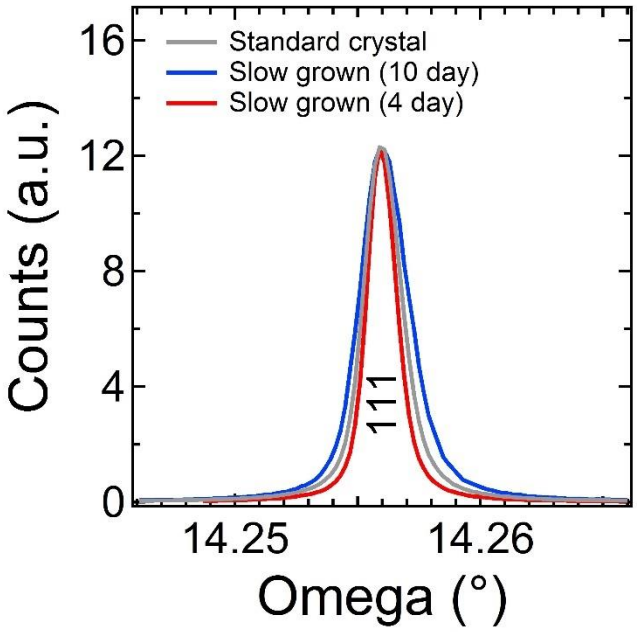

Figure 4.25: (111) rocking curves for standard and slow-grown pyrite crystals. All crystals are grown in highly pure pBN crucibles with highest purity precursors to avoid unintentional doping. The slow-grown crystals were grown in a period of 4 (labeled "4 day") and 10 (labeled "10 day") days. All the reported crystals have very narrow FWHM (< 8 arcseconds). The position of the peak was normalized based on the peak position of the (111) plane in the synchrotron XRD pattern (Figure 4.24).

Magnetic and optical properties of the crystals are also compared with each other. Figure 4.26 and Figure 4.257 illustrate this comparison, respectively. The Induced magnetic moment in both types of crystals was the same and showed the same behavior as it was discussed in Section 4.1.4. Minor differences are due to the extent of surface oxidation and surface damages. Like the standard crystals, the slow-grown crystals exhibited the same optical features, with the same thickness and temperature dependence (see Section 4.1.5 for details).

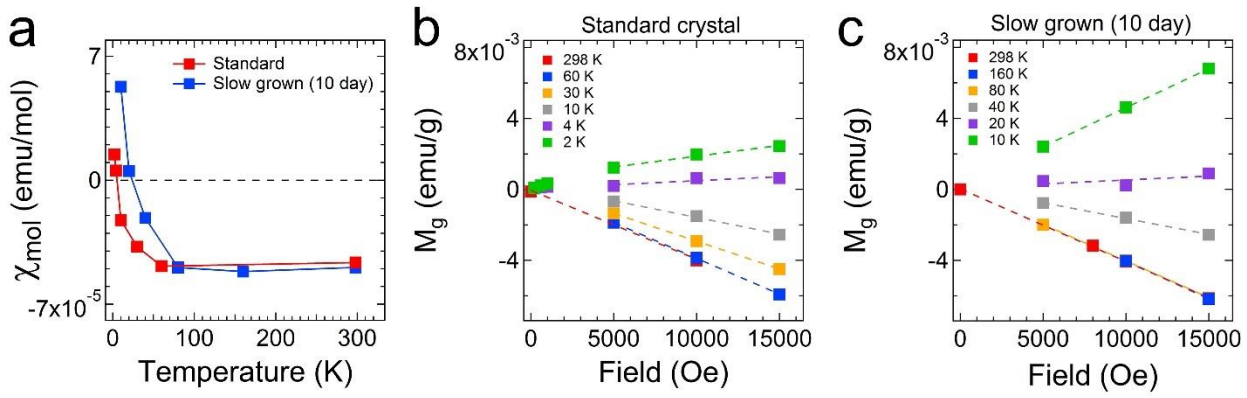

Figure 4.26: Magnetic properties of standard and slow-grown crystals. (a) Molar susceptibility with respect to temperature. Both crystals show diamagnetic behavior at high temperatures, and then become paramagnetic at low temperatures due to mostly surface oxides and broken surface bonds. (b) and (c) Induced mass magnetization (M_g) at different fields, showing negative diamagnetic behavior at high temperatures, and positive paramagnetic behavior at low temperatures. Molar susceptibility in (a) was calculated based on the fits to these plots.

The elemental purity of the crystals has been looked at with ICP-MS. Nu AttoM High-Resolution ICP-MS system (explained in Section 2.5.3) was used. Twenty-eight elements were measured quantitatively, and twenty-two elements were measured semi-quantitatively by the Nu Quant software (version 1.1135.1) based on the quantitatively measured elements. Standard solutions were used to measure the elements quantitatively. Table 4.4 shows the result of elemental analysis for a slow-cooled and a standard crystal. Both crystals have the same elemental purity. It has to be noted that due to limitations of ICP-MS and our technique, only the reported elements were able to be measured successfully. Elements with low atomic masses, halides, and elements with atomic masses that are prone to polyatomic interferences were not able to be measured accurately.

Table 4.4: Elemental analysis of a slow-grown and a standard crystal.

Slow growth			
element	ppm at	element	ppm at
Na	116.3078	Ba	0.1200
Mg	2.2000	La	<0.0003
V	0.2911	Ce	<0.0003
Cr	0.7751	Pr	0.0001
Mn	0.7197	Nd	0.0001
Co	0.5548	Sm	0.0002
Ni	0.8292	Eu	<0.0001
Cu	1.9146	Gd	<0.006
Ga	0.0218	Dy	<0.0002
As	0.0087	Ho	0.0001
Se	0.1156	Er	<0.0001
Rb	<0.009	Tm	<0.0001
Sr	0.0017	Yb	0.0001
Y	0.0006	Hf	0.0002
Zr	0.0058	Ta	<0.0003
Nb	0.0001	W	<0.0012
Mo	0.0159	Re	0.0002
Ru	0.0731	Os	<0.0002
Rh	0.0170	Ir	<0.0002
Pd	0.0136	Pt	0.0007
Cd	0.0068	Au	0.0772
Sn	0.0115	Hg	<0.06
Sb	0.0001	Tl	0.0060
Te	0.0536	Pb	0.1468
Cs	<0.004	U	<0.002

Standard			
element	ppm at	element	ppm at
Na	411.3223	Ba	<0.1
Mg	1.1300	La	<0.0003
V	0.2876	Ce	<0.0003
Cr	4.5788	Pr	0.00002
Mn	0.8001	Nd	0.00002
Co	0.5438	Sm	0.0002
Ni	1.3417	Eu	<0.0001
CU	3.0261	Gd	<0.0001
Ga	<0.026	Dy	<0.0002
As	0.0049	Ho	0.0002
Se	0.3827	Er	<0.0002
Rb	<0.01	Tm	<0.0001
Sr	0.1359	Yb	0.0002
Y	0.0007	Hf	0.0000
Zr	0.0030	Ta	<0.0003
Nb	0.0042	W	<0.0015
Mo	0.0096	Re	0.0197
Ru	0.1235	Os	<0.0002
Rh	0.0205	Ir	<0.0005
Pd	0.0129	Pt	0.0047
Cd	<0.008	Au	0.0009
Sn	<.006	Hg	<0.07
Sb	<0.006	Tl	0.0116
Te	0.0682	Pb	0.0429
Cs	<0.005	U	<0.002

* Blue= semi-quantitatively measured

While the cooling rate of the melt had little effect on the structure, magnetic properties, optical properties, and elemental composition of the pyrite crystals, it had a significant impact on their electrical properties.

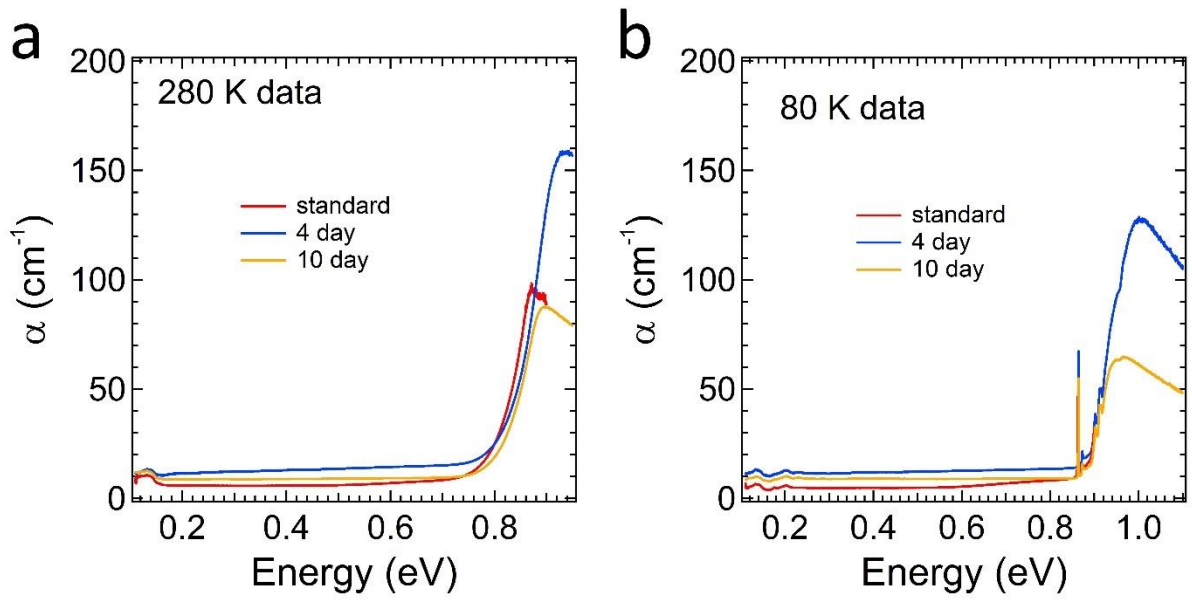

Figure 4.27: Optical absorption of standard and slow-grown crystals. Absorption coefficient spectra of DSP fine polished slow-grown (grown in 4 and 10 days) and standard crystals at (a) 280 K, and (b) 80 K. The absorption spectra are identical. Minor differences in sub-gap absorption are due to the quality of the surface polish.

Figure 4.28 shows conductivity and Hall coefficient data for typical slow-cooled (10 day, 230 μm thick) and standard (1 day, 90 μm thick) crystals prepared as polished (111)-oriented slabs. As reported previously, [29] the conductivity and Hall coefficient plots show three regions for the standard crystals. At high temperatures (T > ~450 K), the crystal is intrinsic. In the second region (180 < T < 400 K), the transport is dominated by the bulk donors. In this region the Hall coefficient has large negative values. Moreover, since the conduction is dominated by one charge carrier in this region, the full Hall coefficient equation (below) can be simplified to $R_H = -1/ne$.

$R_H = \frac{p\mu_h^2 - n\mu_e^2}{e(p\mu_h + n\mu_e)^2}$ p, n= hole and electron concentration, μ_h, μ_e = hole and electron mobility

Therefore, the Hall coefficient and the conductivity ($\sigma = n\mu e$) values can be used to calculate the charge carrier density (n) and the carrier mobility (μ). As the temperature further decreases, the transport becomes mixed between electron and surface holes before it becomes dominated by the holes at temperatures below 120 K. It should be noted that in the mixed conduction region, the Hall coefficient exhibits an unusual behavior. It reaches a minimum, and the sign of it changes from negative to positive (electron dominant to hole dominant) at 120 K. The slow-cooled crystal behaves the same way at low temperatures (T < 200K). Like the standard crystal, the transport is dominated by surface holes and the Hall data is noisy due to small Hall voltages (V_H). However, the surface dominant transport region of the slow-cooled crystals has shifted to the higher temperatures. The mixed transport region and the electron bulk transport region have also shifted to higher temperatures (200 < T < 400 K). The major difference of the slow-cooled crystal is the lower conductivity of the crystals in the bulk dominant transport region. The conductivity of the crystal is around two orders of magnitudes lower than the standard crystal. The lower conductivity ($\sigma=n\mu e$) can be either due to the lower density of charged carriers (bulk donor density) or lower mobility of charged carriers (electron mobility). As explained before, the charge carrier density and mobility can only be correctly calculated from Hall data when the equation for the Hall coefficient ($R_H = \frac{p\mu_h^2 - n\mu_e^2}{e(p\mu_h + n\mu_e)^2}$) and the equation for conductivity ($\sigma = e(n\mu_e + p\mu_h)$) can be written in their simplified form ($R_H = -1/ne$ and $\sigma = n\mu e$,respectively). In order to understand the actual reason behind the lower conductivity, we have looked at the mobility values in the bulk electron transport region at higher temperatures. (Figure 4.28c). The behavior of bulk electron mobility and surface hole mobility has been explained in Figure 4.6 for a standard

crystal. Therefore, comparing the mobility values of the crystals at high temperatures can explain if the lower conductivity of slow-cooled crystals is due to mobility or carrier concentration. As evident in Figure 4.28c, the mobility of electrons in the slow-cooled crystal is slightly higher than the standard crystal at high temperatures. Hence, the reduction in donor density of the slow-cooled crystal is the real reason behind its low conduction.

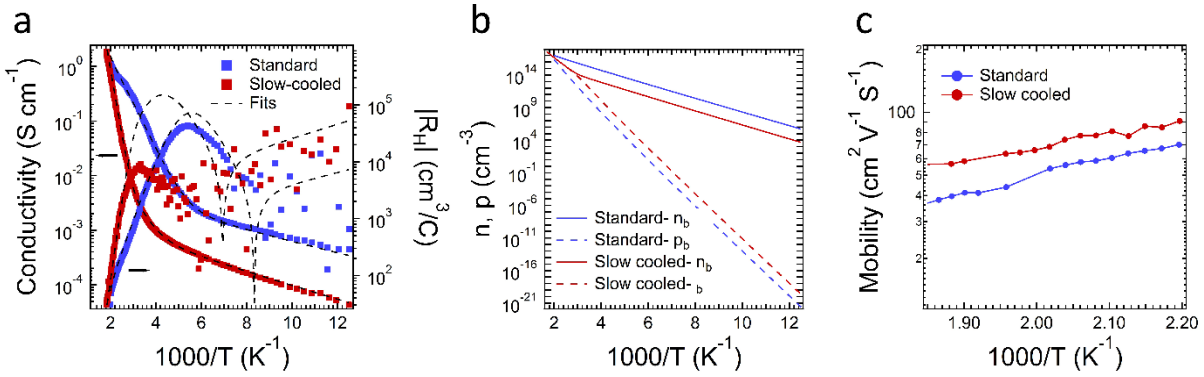

Figure 4.28: Electrical properties of a slow-cooled and a standard crystal. Both crystals were fine polished, and colloidal silver was used to make ohmic contacts to them. The slow-cooled crystal was grown in 10 days. (a) Temperature-dependent absolute Hall coefficient and conductivity data with their respective fits from the numerical Hall model (dotted lines). Due to small hall voltages at temperatures lower than 300 K for the slow-cooled crystal (mixed conduction region has extended to high temperatures), Hall coefficient cannot be trusted in this region and the experimental result is not accurate. (b) bulk electron (n_b) and hole (p_b) carrier concentration. (c) Mobility values based on the experimental data in the temperature region that the values can be trusted.

We used a numerical model (details in section 2.8.1) to predict the conductivity and Hall coefficient behavior of the crystal. Table 4.5 shows the fit parameters that were used to model the data in Figure 4.28a. The conductivity plot could have been modeled by either a decrease in the bulk donor density or a decrease in the mobility values. Therefore, the mobility values were input to the model and were taken from experimental results in the trusted region. The comparison between the fits implies that the bulk donor density is the only parameter that has

decreased substantially by the slow growing of the crystal. The Hall effect data in conjunction with the modeling results has justified our hypothesis that by the slow growing of the crystals, the density of bulk donor states will decrease substantially.

Table 4.5: Electrical properties of the slow-cooled and the standard crystal.

Parameter	**Standard Crystal**	**Slow cooled crystal**
N_D **(cm^{-3})**	5.62×10^{18}	1.94×10^{15}
E_C-E_D **(meV)**	0.4	0.41
N_A **(cm^{-3})**	5.22×10^{20}	2.29×10^{20}
E_A-E_V **(meV)**	0.028	0.036
$E_{g,\ 300\ K}$ **(meV)**	0.78	0.78
$\mu_{e,\ 300\ K}$ **(cm^{2}V^{-1}S^{-1})**	245	255
$\mu_{h,\ 300\ K}$ **(cm^{2}V^{-1}S^{-1})**	2.5	2.5
d_S ***(nm)***	5	5

The V_{OC} of pyrite devices can be improved substantially by lowering the thermionic-emission currents due to reduced number of bulk donors. Since there is an upward band bending on the surface of pyrite due to the surface states, the donors become ionized at the surface. The ionization causes extreme band bending, and enhances tunneling rate by increasing trap-assisted tunneling. Therefore, reduction of the number of donor states will result in less tunneling losses and boost the V_{OC}.

In Figure 4.29, the band diagram of the standard and the slow-cooled pyrite crystals is calculated with the parameters reported in Table 4.5. In regular pyrite crystals with $N_D \sim 6 \times 10^{18}$, about 192

meV is lost through tunneling (assuming 5nm as the tunneling limit), leaving maximum photovoltage of 265 meV for any pyrite devices. By lowering N_D to 1.9×10^{15}, the potential drop will be around 33 meV, and the photovoltage of such devices can be enhanced to 316 meV (These values are based on 0.78 eV as the bandgap of pyrite). It should be noted that the degree of band bending and the amount of tunneling current depends on the donor density. Although the reduction of bulk donor density will reduce the tunneling losses, at the same time it will reduce the total band bending as well.

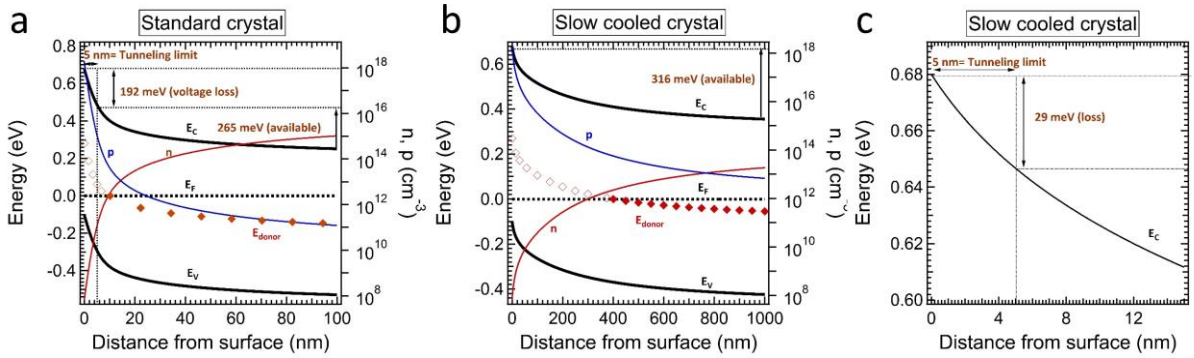

Figure 4.29: Calculated equilibrium band diagram of the pyrite crystals based on the reported values in Table 4.5. (a) Standard crystal, 192 meV of the barrier is lost through thermionic field emission (assuming 5 nm as the tunneling limit), leaving 265 meV as the available photovoltage for any pyrite junction. (b) and (c) Shows the same band diagram calculation for the slow-cooled crystal with different length scales (for clarity). (c) Shows the amount of voltage loss due to tunneling losses (29 meV). In the case of the slow-cooled crystal, 316 meV would be the available photovoltage for the potential pyrite junctions.

To understand the effect of lowering the bulk donor density on the thermionic-field emission (TFE) current, the JV curves of a metal/ semiconductor Schottky diode have been modeled based on the work of Padovani and Stratton (modeling has been done by Trenton Salk). [93] The reverse current density greatly decreases with a lower density of bulk donors (Figure 4.30).

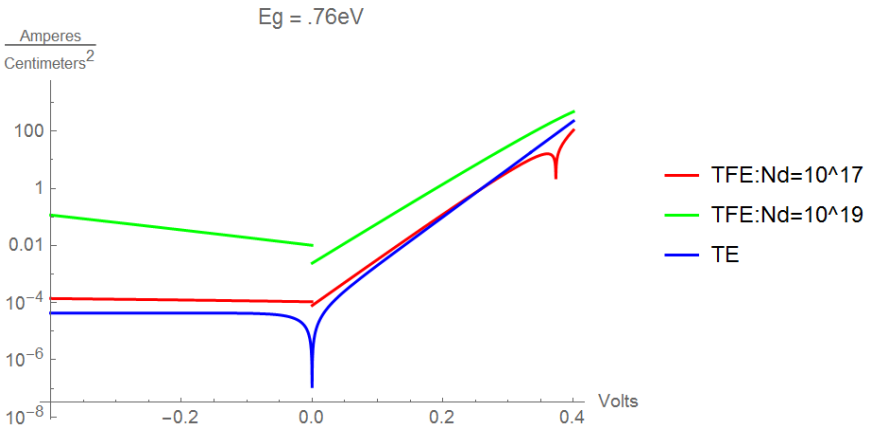

Figure 4.30: Effect of bulk donor density (Nd) on TFE current. The band gap of pyrite is assumed to be 0.76 eV at room temperature. TFE current density is modeled by assuming 10^{17} cm^{-3} and 10^{19} cm^{-3} donor density. Thermionic emission (TE) current depends only on the barrier height and is independent of the donor density. Figure is courtesy of Trenton Salk.

Making pyrite devices with high photovoltages would ultimately substantiate our findings. At the time of writing this dissertation, efforts were towards making Schottky and photo-electrochemical (PEC) devices with the standard and slow-cooled crystals. A summary of the outcome of pyrite single crystal solar devices is discussed in the next section.

4.3 Devices

As discussed in Section 1.2, single crystals of pyrite have been used in Schottky junctions and wet junctions. The presence of surface damages due to polishing and surface states has proved to be very detrimental to the performance of devices. [94] Cathodic etching (proton reduction) in acidic solutions (e.g. 0.5 M H_2SO_4 solution) has resulted in better device performances. Figure 4.31

shows the effect of proton reduction on the surface of CVT-grown pyrite single crystals in a Schottky junction and a wet junction. It was observed that a FeS_2/ Pt Schottky junction is not rectifying unless the pyrite surface goes under a cathodic etching before the Pt deposition. The evolution of H_2 on the surface of pyrite reduces the polishing damages, and potentially reduces the surface recombination velocity. The pyrite junction is rectifying after the cathodic etching, and exhibit a substantial photocurrent under illumination (~30 $mA.cm^{-2}$). [95] Cathodic etching has proved to be essential for the pyrite electrochemical cells as well. Alonso-Vante et al., [94] showed that pyrite electrochemical cells with 4 M HI + 2 M Cal2 + 0.05 M I2 as the electrolyte, will only show a substantial photocurrent under illumination after undergoing proton reduction (Figure 4.30b).

In this work, we have used our flux-grown pyrite crystals to make solar devices. As it was discussed in Section 4.2, using the slow-grown crystals in pyrite Schottky or wet junctions have the potential to boost the photovoltage of the devices. Lower bulk donor states should result in a reduction in the reverse current and boost the V_{OC}. Fabrication of solar devices with both standard and slow-grown crystals are currently in process, as the current dissertation is being written. Figure 4.32 shows flux-grown pyrite Schottky and electrochemical junctions. [65]

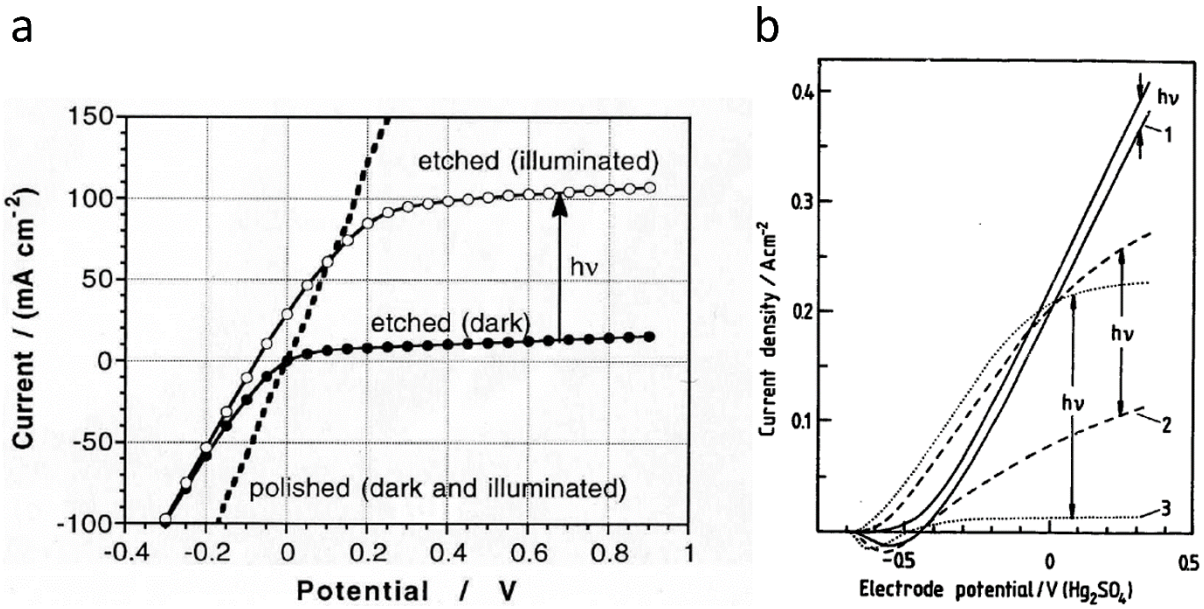

Figure 4.31: Effect of cathodic etching (proton reduction) on pyrite Schottky junctions and PEC devices. (a) Current/ voltage of a n-type (111)/ Pt contact in dark and under white light with and without cathodic etching (passing a constant current of -15 mA.cm^{-2} for several minutes in a 0.5 M H2SO4 solution) prior to Pt deposition (light intensity = 205 mW.cm^{-2}). No rectification and/or photoeffect was observed without any cathodic etching. In the etched case, photocurrent density of 30 mA.cm^{-2} was obtained under short circuit current condition with a photovoltage of 75 mV. (b) Current/ voltage characteristics of pyrite (100) electrode in 4 M HI + 2 M CaI_2 + 0.05 M I_2 solution under intermittent illumination (1.06 W.cm^{-2}). (1), (2) and (3) correspond to 0, 10 and 140 min of cathodic etching in a 0.5 M H2SO4 solution. Photocurrent is enhanced greatly after the proton reduction at the surface of pyrite. Figure is adapted from [94] and [95].

Both devices were fabricated and measured by Moritz Limpinsel. Au, W, and Pt has been tested in the Schottky junctions (the Pt junction was fabricated and tested by Trenton Salk). The Schottky metal has been evaporated on the surface of etched (piranha or Hf) polished pyrite slab (standard and slow-cooled) without any cathodic etching. JV characteristics of none of the Schottky junctions exhibited rectification. The representative JV curves of 3 FeS_2/ Au junction is shown in Figure 4.32a. Cathodic etching of pyrite before the metal deposition will most likely result in a rectification and a photo response. In the pyrite wet electrochemical junction, we experienced the same reported behavior. [94, 96] Piranha etched polished standard crystals were

mounted on a conductive wire, and were covered in an epoxy with only one facet showing. A conventional three-neck electrochemical cell was used, with Pt as the counter electrode, Ag/ AgCl as the reference electrode, and pyrite as the working electrode. A fresh aqueous solution of 0.7 M HI, 0.15 M CaI_2, and 0.03 M I_2 was used for the electrolyte. A potentiometer was used, and the JV response of the cell was measured in dark and light (AM1.5G). Little photoresponse was measured without any proton reduction. However, cathodic etching in a piranha solution (passed charge = 30 C/cm^{-2}) resulted in a substantial increase in the photocurrent density (> 13 A/cm^2). Slow-grown crystals are also in the process of being measured in this fashion. Observing a better device performance in the slow-cooled crystals will confirm that the bulk donor density has indeed reduced and is the reason for the improved device performance.

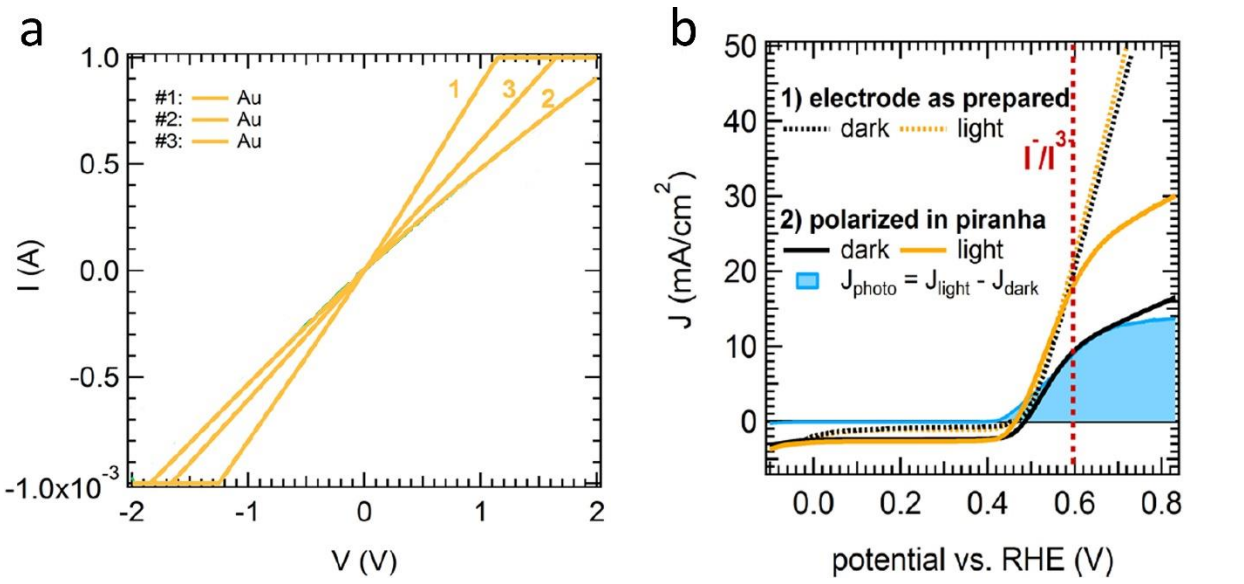

Figure 4.32: Pyrite solar devices with flux-grown single crystals. (a) JV curve of a pyrite Schottky junction with gold, with colloid silver as the top contact. All three devices showed no rectification. (b) JV curve of the PEC with pyrite as the working electrode, Pt as the counter electrode, and Ag/ AgCl as the reference electrode. Cathodic etching in a piranha solution (passed charge = 30 C cm^{-2}) was needed to enhance the photocurrent density (> 13 A cm^{-2}). The solar device fabrication and testing were done by Moritz Limpinsel. Figure is adapted from [65].

Chapter 5

Doped pyrite single crystals

5.1 Introduction

Flux-grown pyrite single crystals reported in this work are the purest pyrite single crystals reported to date (99.998% pure on a metals basis). Therefore, they can act as a great platform model to understand the effect of a variety of doped elements on the electronic and optical properties of pyrite. CVT-grown and natural pyrite crystals are reported to have a wide range of impurity elements in them (e.g. Cl, Br, Co, Cr, Ni). [46] Understanding the effect of these impurities on the electronic properties of pyrite is crucial for making high efficient pyrite solar devices. Controlling the Fermi level, tuning the carrier type and carrier concentration, manipulating the inversion layer, and gaining insight into the bulk defect chemistry of pyrite can be understood and studied by understanding the effect of doped elements on electronic, optical and magnetic properties of pyrite. Lastly, the insight from the study of doping on the single crystals can be implemented in pyrite thin films.

Different dopants (Cl, Br, P, As, Cr, Ni, and Co) were initially chosen as the dopants in this work. The effect of these elements on properties of pyrite is important due to several factors. Halogen

compounds are used as transport agents in CVT-grown pyrite single crystals and are speculated to be n-type dopants. [27] Arsenic and phosphorus are reported to be p-type dopants in pyrite. Hence they have a potential of changing pyrite single crystals from n-type to p-type (like the thin films). [57] Cobalt and nickel are present as impurities in most of the pyrite crystals. They are known to be n-type dopants, and it is important to understand their role on the properties of pyrite devices. Moreover, they can potentially change the charge transport from p-type to n-type in pyrite thin films. [97] Chromium is also present in most synthetic and natural pyrite crystals. A study by Yu et al., [98] identified Cr to be responsible for the unknown high energy optical transition (0.86 eV) present in the optical absorbance spectra of pyrite crystals (discussed in section 4.1.5). The dopants were added in an elemental or a compound form to the precursors (addition details will be discussed in each section separately).

The addition of As, P, Cl, and Br (0.2-4 weight% with respect to iron) didn't have any clear effect on optical and electronic properties of crystals measured by FTIR and Hall effect, respectively. Lack of incorporation of elements in the crystal by our flux crystal growth method is most likely the reason. Therefore, only the effect of Co, Cr, and Ni are presented in this work. They all had a clear sign of incorporation into the crystals and changed the properties of pyrite extensively (will be discussed in the following sections).

The effect of each dopant was measured by Synchrotron XRD (structural and phase purity), ICP-MS (elemental concentration and homogeneity of dopant), FTIR (optical properties), MPMS (magnetic properties), and temperature-dependent Hall effect and resistivity (electrical properties). Systematic spin-polarized density functional theory (DFT) calculations for each

dopant was also used to predict their influence on the electronic and optical properties of pyrite. The DFT calculation was done by Jeongwoo Kim (post-doctoral student in Prof. Wu's laboratory at UCI). The combined experimental measurements along with theoretical calculations can give a detailed picture of the effect of dopants on pyrite. Thickness and temperature dependent optical, electrical, and magnetic properties of undoped crystals (reported in Chapter 4) served as the reference point to identify the effect of doping.

5.2 Cobalt

Iron disulfide (pyrite) is a diamagnetic semiconductor and cobalt disulfide (with the same pyrite structure) is a half-metallic ferromagnet. It has been shown that FeS_2 and CoS_2 can form solid solutions in a wide range of cobalt concentrations. [99- 101] Doping of pyrite single crystals with cobalt ($Fe_{(1-x)}Co_xS_2$) with different concentrations has been studied before ($0 \leq x \leq 1$). [57, 102- 104] In almost all of the studies, CVT-grown or natural pyrite crystals were used that had a substantial concentration of unintentional dopants in them, which made them not the best host crystals for studying the effect of dopants. The conductivity of the doped crystals was reported to increase as the amount of cobalt was increased. Cobalt-doped pyrite showed to be a half-metal over a wide concentration range. [105- 108] Chandler et al., [103] proposed an energy-band scheme in which cobalt induces an energy state very close to the conduction band. Guo et al., [109] reported a magnetic ordering in $Fe_{(1-x)}Co_xS_2$ as x becomes greater than 0.01 due to the formation of Griffith

phases, Co substitution even in the most lightly doped cases ($x = 3 \times 10^{-4}$) caused metallic conductivity behavior (resistivity increases with increasing temperature). [104]

In this study, dicobalt octactacarbony (DOC) was used as the cobalt precursor. DOC was dissolved in hexane, and the small amount of the solution was added to the iron via a micropipette in the alumina crucible. The mixture of iron and DOC was heated at 200°C for 30 minutes to evaporate all the hexane. The flux and sulfur were added next to the crucible as it was discussed in Chapter 2. It has to be noted that solution addition of dopant was chosen despite powder addition of dopants. Solution addition will result in more homogeneous mixing and doping. It also enables adding dopants in minuscule amounts (< 1 mgr). DOC was chosen as the precursor instead of elemental Co to avoid dissolving the precursor in HNO_3. The presence of nitric acid might result in unintentional doping with nitrogen. Lastly, since alumina crucibles were more readily available, they were used for all of our doping studies including Co (instead of pBN crucibles). No apparent optical and electrical differences between the alumina-grown and pBN-grown undoped pyrite crystals were observed. Undoped pyrite crystals grown in alumina crucibles exhibited the same optical, electrical, and magnetic properties as crystals grown in pBN crucibles. Therefore, the reported properties in Chapter 4 can be taken as reference points for the doped crystals.

5.2.1 Elemental

ICP-MS was used to quantify the concentration of cobalt in the Co-doped crystals. Doped crystals were sectioned parallel to the top facet with a slow diamond saw; then each section was

dissolved in nitric acid, and measured with ICP-MS. The concentration of cobalt was measured in each section to investigate the possibility of any concentration gradient from a top facet of crystal to a bottom part of the crystal. Table 5.1 shows the measured concentration of cobalt in different crystals. It has to be noted that Co-doped crystals with a high concentration of Co (> 500 ppm) were not investigated in this work to avoid having a crystal with metallic electrical conduction properties.

Table 5.1: Concentration of cobalt in $Fe_{(1-x)}Co_{(x)}S_2$ crystals.

Sample	**Section**	**ppm.at**	**cm^{-3}**	**Composition**
Co_1	1a	244		
	1b	224	1.8×10^{19}	$Fe_{0.9993}Co_{0.0007}S_2$
	2a	300		
	2b	316		
Co_2	1a	253		
	1b	261		
	2a	330	2.17×10^{19}	$Fe_{0.99914}Co_{0.00086}S_2$
	2b	283		
	3a	309		
Co_3	Whole	149	1.12×10^{19}	$Fe_{0.9996}Co_{0.0004}S_2$
Co_4	Whole	352	2.66×10^{19}	$Fe_{0.999}Co_{0.001}S_2$
Co_5	Whole	334	2.5×10^{19}	$Fe_{0.999}Co_{0.001}S_2$
Co_6	Whole	70	2.3×10^{18}	$Fe_{0.9998}Co_{0.0002}S_2$

Whole = a whole small crystal was measured (no sectioning). Section 1 refers to the top of the crystal and section 3 to the bottom of the crystal (a and b refers to pieces of the crystal in the same z-section, they were measured to check for homogeneity in the xy plane.). The concentration (cm^{-3}) and the composition columns are average amounts considering the whole crystal. Each section is around 500 microns thick.

No significant concentration gradient in the crystals was observed. The differences between measured values are mostly due to errors in the ICP-MS measurements, which arose from polyatomic interferences, and small mass measurements errors in each sample. It has to be noted

that the concentration of cobalt in samples that didn't show any sign of doping in the optical measurements or showed a sign of complete metallic behavior in the electrical measurements were not measured. In the following sections, the characterization of the reported samples in Table 5.1 will be discussed. Crystals quoted with the same name in the following sections are from the same run of crystal growth (each run usually yielded several crystals with different sizes, and the smallest crystal was used for the ICP-MS measurements). Although differences in the amount of Co corporation in each crystal of the same run is possible, it is assumed that the concentration of the dopant is the same for all the yielded crystals in each batch (the same assumption has been made for the other doping cases as well). Co-doping did not result in any unintentional doping of other elements.

5.2.2 Structural

Cobalt doping produced highly-faceted crystals like undoped cases. No apparent differences were observed between Co-doped crystals and undoped crystals. High-resolution synchrotron powder XRD was used to check for phase purity. The XRD pattern showed no trace of other crystalline or amorphous phases. Figure 5.1 shows the XRD pattern of the Co-doped crystal with the highest concentration of cobalt (crystal Co_2) that was measured. All other measured crystals had less amount of cobalt in them and showed no sign of extra phases either. Lattice parameters of the doped and undoped crystals were obtained by Rietveld refinement of the XRD pattern. The diffraction peaks in the Co-doped crystals were shifted to the smaller 2theta degrees, which

is indicative of lattice expansion due to the incorporation of Co. The amount of expansion is expected by the Vegard's law by using the lattice constant of CoS_2 (5.524 Å). [100]

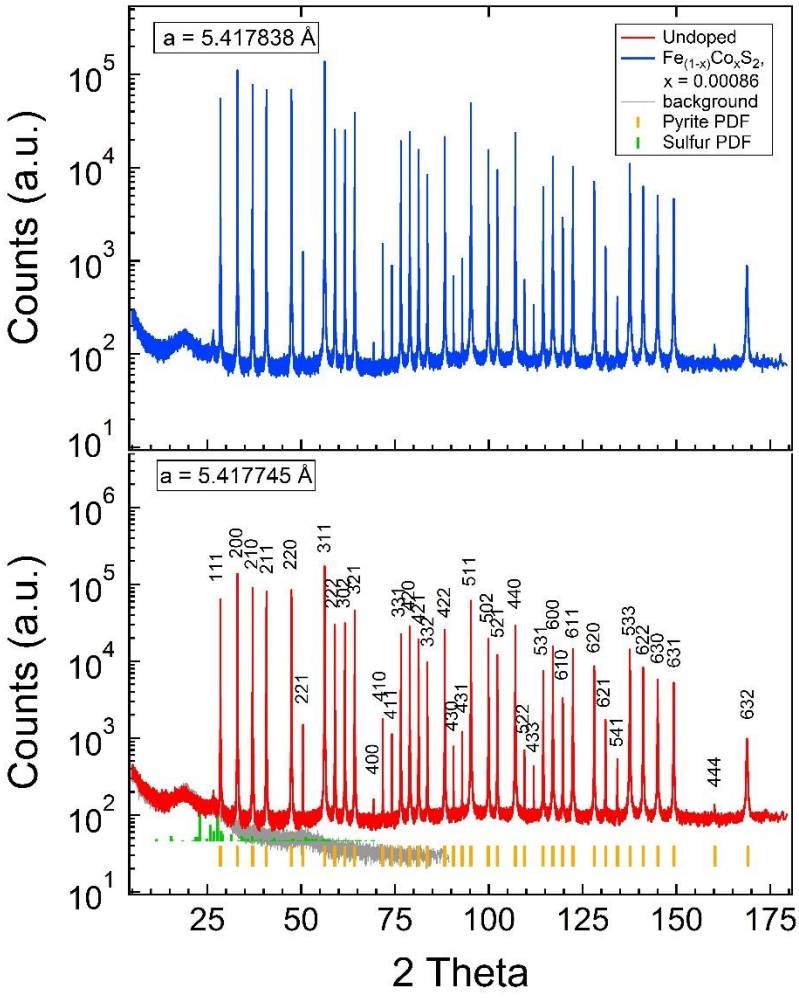

Figure 5.1: Synchrotron XRD pattern of a powdered undoped and a powdered Co-doped crystal on a log scale. Powders were made from the crystals of batch "Co_2" with expected concentration of cobalt to be ~287 ppm at. All 39 reflections index to pyrite and no other phases are detected. Lattice parameters were calculated by Rietveld refinement with PDXL2 software at room temperature. The background pattern is for an empty capillary tube. Small yellow bars near the x-axis denote the pyrite reference peaks.

5.2.3 Optical

The optical absorbance of the Co-doped crystals was measured by the FTIR and was compared with the undoped crystals (see Section 4.1.5 for details of undoped crystals). Figure 5.2 shows the optical absorption coefficient of the Co-doped crystals in the Mid-IR energy range.

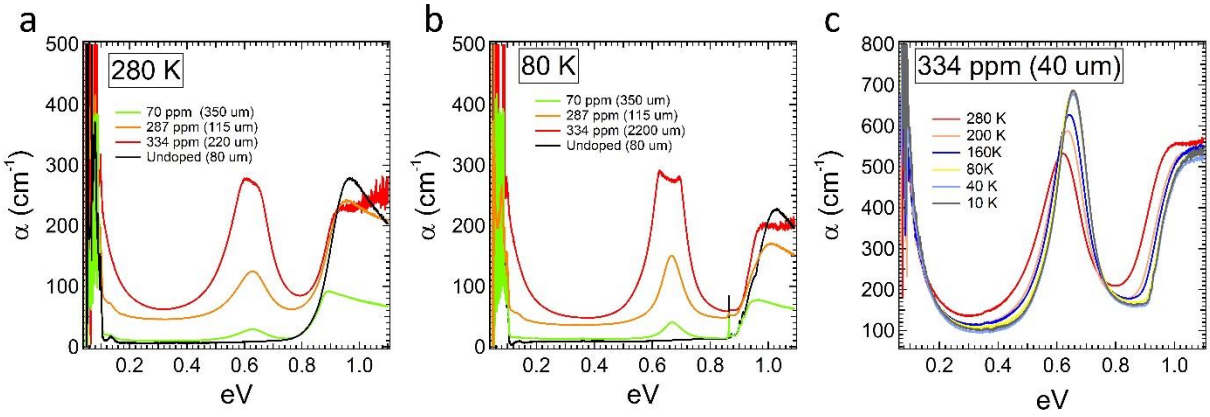

Figure 5.2: Optical absorption spectra of Co-doped pyrite single crystals. All crystals were DSP fine polished. The absorption coefficient for each slab is calculated based on their optical extinction measured by the FTIR. (a) and (b) Calculated absorption coefficient at 280 K and 80 K, respectively. The black curve represents an undoped crystal (Co < 1 ppm). The concentration of Co is in ppm atomic, as it was reported in Table 5.1. (c) Calculated absorption coefficient for Co_5 slab at different temperatures. The optical transition at ~0.6 eV becomes more intense and moves to higher energies as the temperature goes down.

Cobalt doping results in two absorbing optical transitions at energies blow the gap (~0.1 eV and ~0.6 eV). Both transitions are highly absorbing, and as the concentration of cobalt increases, they become more prominent. The transition at ~0.1 eV is very absorbing, and it overlaps partly with the low energy optical transitions for undoped pyrite crystals (discussed in section 4.1.5). Therefore it is not fully resolvable in the optical spectrum for low doped cases. The optical

transition becomes much wider and resolvable in the high doped case though (red curve in figure 5.2a). The optical transition at the 0.6 eV increases as the temperature decreases, and it also blue shifts in energy (figure 5.2.c). It follows the shift of the band edge, as the temperature decreases. It has to be noted that both features are believed to be due to bulk features based on their optical extinction thickness dependence (data not shown here). The optical features are similar to the reported features by Lehner et al., [57] although they measure crystal with higher cobalt concentrations.

5.2.4 Magnetic

To understand the spin state of our dopants (CO, Cr, and Ni) magnetic measurements can be very useful. The total angular momentum has a contribution from spin angular momentum (due to unpaired electrons) and orbital angular momentum. In the cases that the orbital angular momentum is quenched by the surrounding crystal field, it can be assumed that there is no spin-orbit coupling. In such cases, the number of unpaired electrons of an atom can be calculated based on its effective magnetic moment (μ_{eff}). Equation 5.1 explains how μ_{eff} is dependent on the number of unpaired electrons (n). [110]

$$\mu\text{eff} = \sqrt{n(n+2)} \quad \text{B.M.} \qquad 5.1$$

$$\mu\text{eff} = 2.828 \times \sqrt{\chi_m \times T}, \quad \text{T = temperature (K)} \qquad 5.2$$

The effective magnetic moment is dependent on the magnetic molar susceptibility (χ_m) as well. Equation 5.2 shows the relationship between μ_{eff} and χ_m. In this work, the induced magnetic

moment in each of doped crystals was measured by MPMS. Since undoped pyrite is diamagnetic by itself, any present paramagnetic susceptibility was associated with the doped elements. The χ_m was calculated based on the concentration of doped elements measured by ICP-MS. Figure 5.3 shows the measured magnetic moments associated with transition metal ions with an octahedral geometry. [110]

Metal Ion	d configuration	Number of Unpaired Electrons	Magnetic moment (B.M.)
Ti^{4+}, V^{5+}	d^0	0	0
Ti^{3+}, V^{4+}	d^1	1	1.7-1.8
V^{3+}	d^2	2	2.7-2.9
Cr^{3+}, Mn^{4+}	d^3	3	3.7-3.9
Cr^{2+}, Mn^{3+}	d^4	4 (high spin) 2 (low spin)	4.8-5.0 3.0-3.3
Fe^{3+}, Mn^{2+}	d^5	5 (high spin) 1 (low spin)	5.7-6.0 2.0-2.5
Fe^{2+}, Co^{3+}	d^6	4 (high spin) 0 (low spin)	5.6-5.9 0
Co^{2+}	d^7	3 (high spin) 1 (low spin)	4.3-5.2 2.0-2.7
Ni^{2+}	d^8	2	2.9-3.3
Cu^{2+}	d^9	1	1.8-2.1
Cu^{+}	d^{10}	0	0

Figure 5.3: Measure magnetic moments, d-configuration, and the number of unpaired electrons for transition metal ions with octahedral geometry. Figure is adapted from [110].

Figure 5.4 shows the measured magnetic moment and corresponding molar susceptibility for a Co-doped and an undoped crystal. The magnetic behavior of all the measured Co-doped crystals was the same as the undoped crystals. Like undoped crystals, the Co-doped crystals were diamagnetic at high temperatures, and become paramagnetic at low temperatures (details in section 4.1.4). No paramagnetic or ferromagnetic behavior was observed by Co doping in our doping range (70-352 ppm at, $0.0007 \leq x \leq 0.001$). This behavior suggests that Co is present in

the lattice of pyrite as Co^{3+} with a low spin configuration, which results in d^6 electron configuration, and zero effective magnetic moment. Like undoped crystals, the source of weak paramagnetism at low temperatures is associated with broken bonds at surface and surface oxidation.

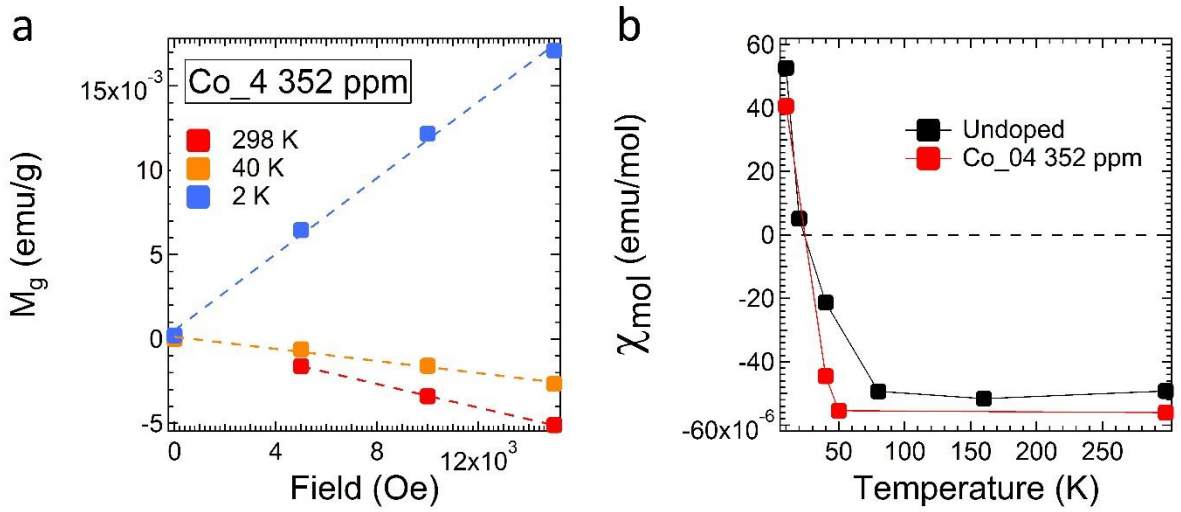

Figure 5.4: Magnetic properties of Co-doped crystals. (a) Induced mass magnetization (M_g) at different fields, showing negative diamagnetic behavior at high temperatures, and positive paramagnetic behavior at low temperatures. Crystal Co_4 with the highest concentration of cobalt is shown. The magnetic response was representative for other crystals with lower cobalt concentration as well. All the measured Co-doped crystals had the same response like the undoped crystals. The dotted lines are the fit to the data, which were used to calculate the molar susceptibility associated with the sample. (b) Molar susceptibility with respect to temperature for a representative Co-doped and an undoped crystal.

5.2.5 Electrical

Temperature dependent conductivity and Hall effect were used to study the electrical properties of Co-doped crystals. Making ohmic contacts to Co-doped crystals proved to be very challenging. Evaporating gold contacts or applying a colloidal silver paste on a smooth or a rough surface of

crystals did not result in perfect ohmic contacts. Although the contacts were not perfect for the Co-doped crystals, reported electrical behavior in Figure 5.5 is representative of the effect of cobalt incorporation in the lattice of pyrite. Based on the sign of the Hall coefficient, all the doped crystals were n-type, and they became more conductive as the concentration of cobalt increased. Increase in the bulk electron concentration is the reason behind the higher conductivity of Co-doped crystals (mobility values were in the same range as the mobility of undoped crystals). The increase in conductivity and semi-metallic conductivity behavior has been reported elsewhere as well. [57, 103, 104] However in all of those cases, the doped crystals did not retain a temperature conductivity dependence that is expected for a semiconductor (conductivity decreases as the temperature decreases). They showed a temperature dependence conductivity like the gray dashed line in figure 5.5, which shows a metallic conductive behavior.

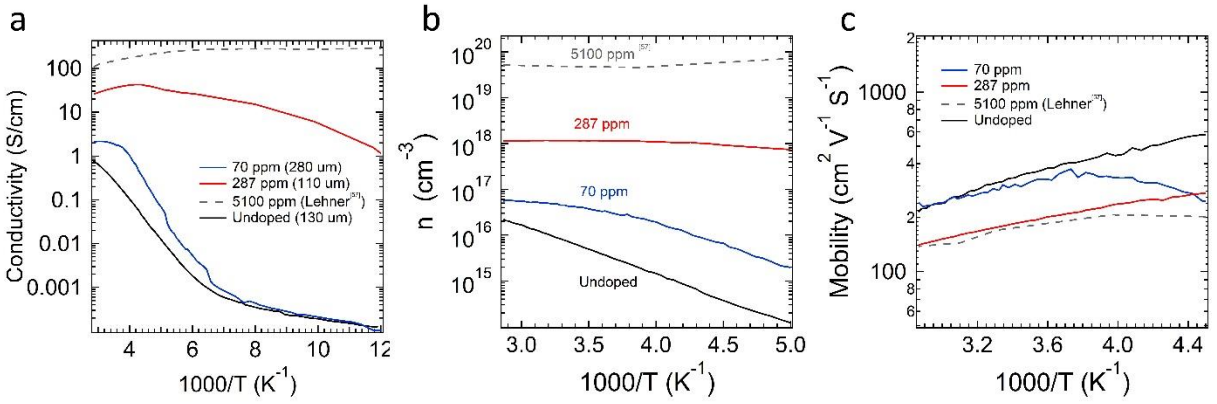

Figure 5.5: Electrical properties of Co-doped pyrite crystals. All reported crystals were fine polished, and colloidal silver was used to make ohmic contacts to them. Making ohmic contacts to Co-doped pyrite crystals proved to be challenging, which made data noisier. (a) Temperature-dependent conductivity data for Co-doped crystals and an undoped crystal (as a reference). The dashed gray line is taken from [57] for comparison. The conductivity of the 287 ppm Co sample has been corrected to reduce the bad contact issue associated with it. (b) bulk electron (n_b) carrier concentration calculated based on the Hall coefficient in the unipolar region. (c) Calculated mobility values based on the experimental data in the unipolar region.

The conductivity behavior of Co_2 (287 ppm) crystal could be qualitatively fitted by assuming the presence of an additional shallow donor (~0.1 eV) in the bulk of the crystals in addition to the bulk and surface states of the undoped crystals (explained in section 4.1.3). It was not possible to use our numerical Hall model to predict the conductivity behavior of the lighter doped crystals by just only assuming the introduction of a shallow donor state close to the conduction band due to cobalt. Having not perfect ohmic contact and the complexity of the electrical properties of the undoped crystals make it difficult to exactly predict and analyze the effect of Co on the electrical properties of doped crystals. In the next section, the combined experimental results (optical, magnetic, and electrical) in conjunction with DFT calculations have been used to understand the effect of cobalt doping on pyrite, and how it modifies the electrical band diagram of pyrite.

5.2.6 Summary

Based on the experimental data. Cobalt has been incorporated into the lattice of pyrite single crystals without forming any other phases. The oxidation state of the cobalt is +3 in pyrite, and it has a d^6 electron configuration (low spin) which results in almost zero effective magnetic moment. It has donated one electron to pyrite, which can explain the higher conductivity of co-doped crystals. Based on the optical data, two absorbing optical transitions are observed (at 0.1 eV and 0.6 eV). It is not apparent the source of the optical transitions. Cobalt can be introducing states in the gap that can be either donor or acceptor with optical transitions from VB or to CB equaling 0.1 eV and 0.6 eV. There are other possibilities that can explain the observed optical

and electronic data as well. Therefore, we used DFT to predict the effect of cobalt incorporation in pyrite and tie in its results to our experimental findings.

The DFT calculations were performed by Jeonwoo Kim (post-doctoral at prof. Wu's laboratory). Systematic spin-polarized DFT were performed to investigate the effect of dopants (Co, Cr, Ni) on the bulk electronic and optical properties of pyrite. A 3 × 3 × 3 supercell with 324 atoms total was used. The doping amount was set to 0.9%. All atoms were fully relaxed until the calculated force on each atom was smaller than 0.01 eV/Å. As a reference, the structural and electronic properties of pyrite was investigated first. Figure 5.6 shows the calculated electrical properties of undoped pyrite; that was measured in collaboration with our group in 2012. [52] It was found that regular GGA calculation would underestimate the band gap of pyrite, and a Hubbard U correction was needed to predict the bulk electronic properties of pyrite accurately (GGA + U). A U value of 2 eV was assigned to d-orbitals to describe the electronic properties of pyrite correctly.

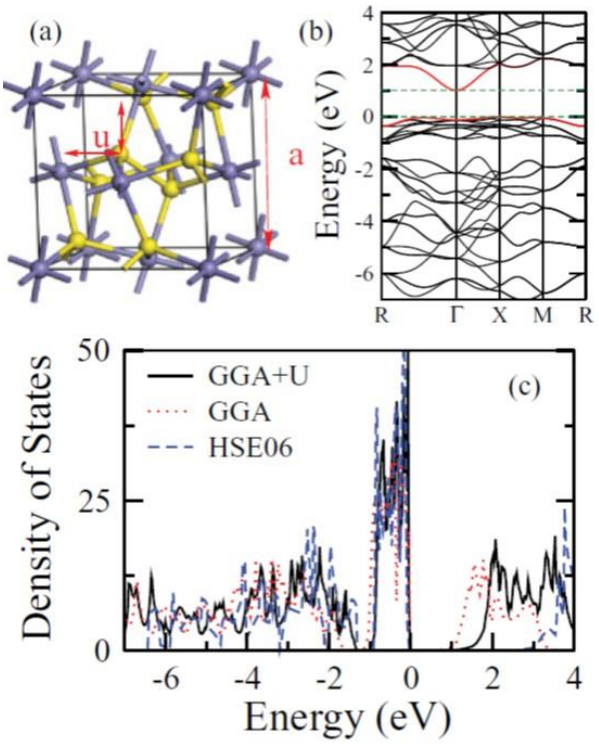

Figure 5.6: DFT calculations of an undoped crystal. (a) The bulk unit cell of pyrite (blue and yellow spheres are Fe and S atoms, respectively). (b) Band structure and (c) density of states (in states/eV.cell of pyrite). Hybridized Exchange Correlation function (HSE06) was another correction method that was applied. It overestimated the band gap. Therefore, GGA + U was used in this work. The graph is reproduced from [52].

To study the effect of doping, a 3 × 3 × 3 supercell was analyzed with the addition of Co atoms (0.9%). Figure 5.7 summarizes the calculation. Band structure, density of states (DOS) and the imaginary part of the dielectric constant (representative of the energy position of expected optical absorption) were calculated based on different values of U (0 eV, 2 eV, and 4 eV).

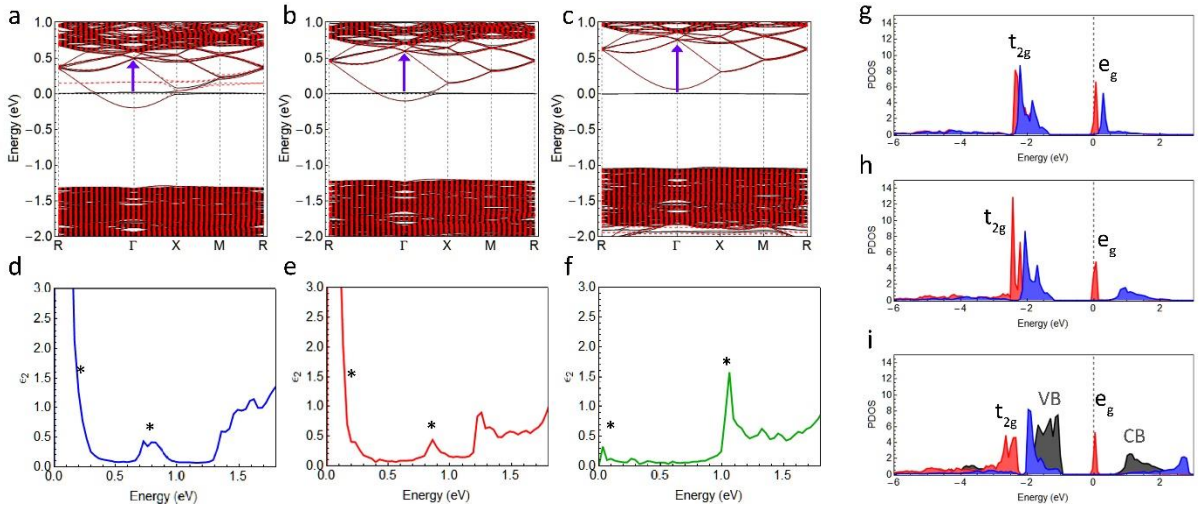

Figure 5.7: Effect of Co doping based on DFT calculations (GGA + U). (a), (b), and (c) band structures of a 3 × 3 × 3 supercell of pyrite doped with Co by assuming 0 eV, 2 eV, and 4 eV as the U value, respectively. The doping amount corresponds to Co concentration of 6.8×10^{20} cm^{-3}. The horizontal dotted lines at 0 eV indicate the Fermi level. The induced energy state due to Co is represented by the black solid line. The donor states are overlapping by the conduction band or just slightly below it in the U = 4 eV case. The blue vertical arrows point out the possible optical transitions (~0.6 eV) that are observed in the experimental optical spectra. (d), (e), and (f) imaginary part of the dielectric constant for U = 0 eV, U = 2 eV, and U = 4 eV, respectively. The stars indicate the energies that the optical absorptions should take place. (g), (h), and (i) DOS of a 2 × 2 × 2 supercell of pyrite doped with Co by assuming 0 eV, 2 eV, and 4 eV as the U value, respectively. CB and VB states (gray) are indicated in (i) and are representative in (g) and (h) as well. The vertical dotted lines show the location of the Fermi level. Red and blue corresponds to up and down spins.

Depending on the amount of U, Co incorporation introduces a state overlapping or slightly under the conduction band (e_g states at 0 eV in the DOS spectra). The effect of different U values was investigated to show how the position of the state can change. It seems like U values close to 2 eV can predict the experimental results more accurately. The introduced shallow donor state can account for the highly absorbing ~0.1 eV feature observed in Figure 5.2. At the same time, the 0.6 eV transition is also predicted by the model (stars and the blue arrows in Figure 5.7). The exact states responsible for these transitions can also be identified. It needs more computational works, which is undergoing as I am writing this dissertation, and it will be published shortly.

In conclusion, by combining all the experimental and theoretical results, the role of Co doping in pyrite can be explained. Cobalt introduces a very shallow donor under CB. The state is ionized at most temperatures and results in higher conductivity of the samples. This confirms the energy model proposed before on the role of Co on the bulk electronic properties of pyrite. [103] Unlike previous publications, [104, 109] it was found that doping pyrite with cobalt at low concentrations will not result in semi-metallic electrical and ferromagnetic properties. Doped pyrite crystals reported in this work were all diamagnetic (like undoped pyrite). They did have higher electrical conductivity than pyrite, but they did not show half-metallic properties. Finding out the exact amount of cobalt that will cause such transitions can be the subject of future work.

5.3 Nickel

Nickel sulfide (NiS_2) crystallizes in the pyrite structure (Vaesite). It has a slightly higher lattice constant than pyrite (a = 6.677 Å). Vaesite is reported to be a small band gap semiconductor with antiferromagnetic properties (Neel temperature = 40 K). [6, 78, 99, 100] Doping of pyrite with Ni has been looked at before as well. Ho et al., [111] reported that nickel introduces a donor state near the conduction band edge of pyrite, and as the concentration of it increases, the conductivity of the doped crystal increases as well. Others have proposed that nickel introduces a donor state in the middle of the pyrite gap. [57, 103] In all of the Ni doping studies, the host crystal contained significant amounts of other transition metal impurities that could influence the real effect of nickel on the optical and electronic properties of pyrite.

In this work, nickel (99.999% pure) was dissolved in hydrazine (with a small amount of sulfur). The solution containing minuscule amounts of Ni was then added to iron in alumina crucibles (in the same fashion as Co doping). Hydrazine was evaporated by heating at 200°C for 30 minutes. Na_2S and sulfur were added on the top of the iron and the dried nickel solution afterward. The rest of the crystal making was the same as the undoped crystals. The effect of nickel doping has been investigated like the Co case. ICP-MS and synchrotron XRD were used to calculate the amount of Ni incorporation and investigate the presence of any phase impurities. FTIR, MPMS, and temperature-dependent resistivity and Hall effect were used to understand the optical, magnetic, and electrical properties. Theoretical calculations (DFT) were used to connect the results of the experiment together and understand the full effect of Ni doping.

5.3.1 Elemental

Like the cobalt case, ICP-MS was used to quantify the concentration of Ni in the Ni-doped crystals. Doped crystals were sectioned parallel to the top facet with a slow diamond saw; then each section was dissolved in nitric acid, and measured with ICP-MS. The concentration of nickel was measured in each section to investigate the possibility of any concentration gradient from a top facet of crystal to a bottom part of the crystal. Table 5.2 shows the measured concentration of Ni in different crystals.

Table 5.2: Concentration of Ni in $Fe_{(1-x)}Ni_{(x)}S_2$ crystals.

Sample	Section	ppm at	cm^{-3}	Composition (x)
Ni_1	Whole	8	6×10^{17}	0.000024
Ni_2	1	29	2×10^{18}	0.000081
	2a	28		
	2b	24		
Ni_3	1	323	3.9×10^{19}	0.0016
	2a	623		
	2b	535		
	3	588		
Ni_4	1	1,187	8.2×10^{19}	0.0033
	2	989		
Ni_5	Whole	950	7.2×10^{19}	0.0028
Ni_6	Whole	4,763	3.6×10^{20}	0.014
Ni_7	Whole	17,942	1.35×10^{21}	0.054

Whole = a whole small crystal was measured (no sectioning). Section 1 refers to the top of the crystal and section 3 to the bottom of the crystal (a and b refers to pieces of the crystal in the same z-section, they were measured to check for homogeneity in the xy plane.). The concentration (cm^{-3}) and the composition columns are average amounts considering the whole crystal. Each section is around 500 μm.

Measuring the concentration of Ni with ICP-MS can be challenging due to the presence of polyatomic interferences. 5-10% error in the reported values is expected. Except for sample Ni_3, no apparent concentration gradient was observed in the measured samples. Ni doping did not result in any unintentional doping of other elements.

5.3.2 Structural

Nickel doping produced highly-faceted crystals like undoped cases in most cases. No apparent differences were observed between Ni-doped crystals and undoped crystals. High-resolution synchrotron powder XRD was used to check for phase purity. Unlike Co doping, it was found that impurity phases had formed when the concentration of the nickel have been high (Ni_6 and Ni_7

growth runs). The XRD pattern showed no trace of other crystalline or amorphous phases for the crystals with doping amounts below 1100 ppm at. Figure 5.8 shows the XRD pattern of the Ni-doped crystal with the highest concentration of Ni (crystal Ni_4) that was measured and no sign of phase impurity was observed. Nickel corporation in the lattice resulted in lattice constant expansion. The amount of expansion for both Ni_3 and Ni_4 samples (Ni_1 and Ni_2 crystals were not measured by the synchrotron XRD) matches the expected expansion by the Vegard's law.

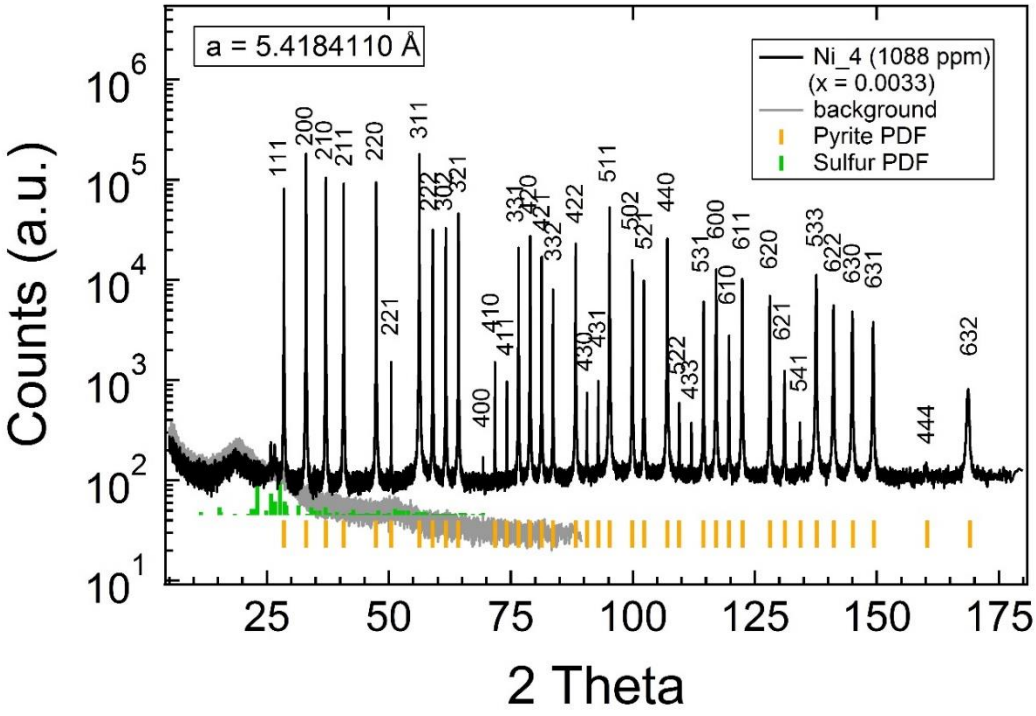

Figure 5.8: Synchrotron XRD pattern of a powdered Ni-doped crystal on a log scale. Powders were made from the crystals of batch "Ni_4" with expected concentration of nickel to be ~1088 ppm at. All 39 reflections index to pyrite and no other phases are detected. Lattice parameters were calculated by Rietveld refinement with PDXL2 software at room temperature. The background pattern is for an empty capillary tube. Small yellow bars near the x-axis denote the pyrite reference peaks.

Figure 5.9 shows the synchrotron of a powdered Ni-doped crystal (Ni_6), which indicated that impurity phases are present. The impurity peaks are identified by the blue asterisks in the figure. The peaks were indexed to iron nickel sulfide ($FeNiS_2$) phases, which suggest that nickel aggregations at certain parts of the crystals have resulted in the formation of these phases. The other highly doped crystal exhibited the same phase impurities as well.

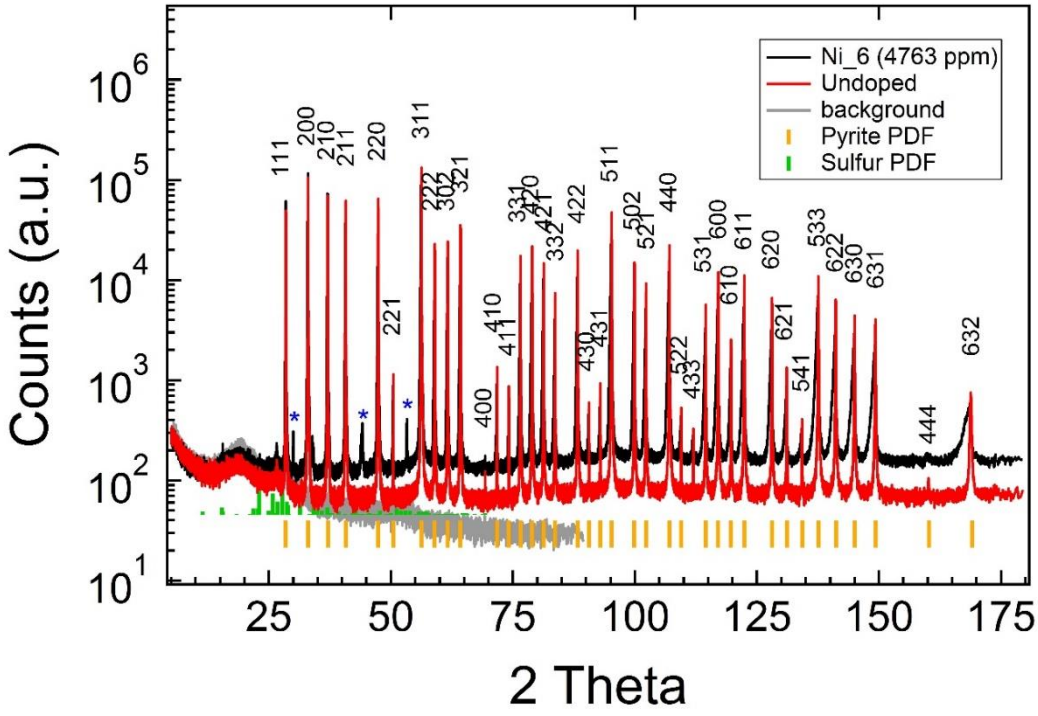

Figure 5.9: Synchrotron XRD pattern of an undoped crystal and crystal Ni_6 (4763 ppm Ni) on a log scale. The doped crystal had extra phases (blue asterisks) indicative of phase impurities. The background pattern is for an empty capillary tube. Small yellow bars near the x-axis denote the pyrite reference peaks.

The fact that high Ni concentration can result in the formation of phase impurities made it impossible to evaluate the effect of Ni on the properties of pyrite at concentrations greater than 1187 ppm.

5.3.3 Optical

The optical absorbance spectra of the Ni-doped crystals were measured by the FTIR in the transmission geometry. Figure 5.10 shows the calculated optical absorption coefficient of the Ni-doped crystals in the Mid-IR energy range.

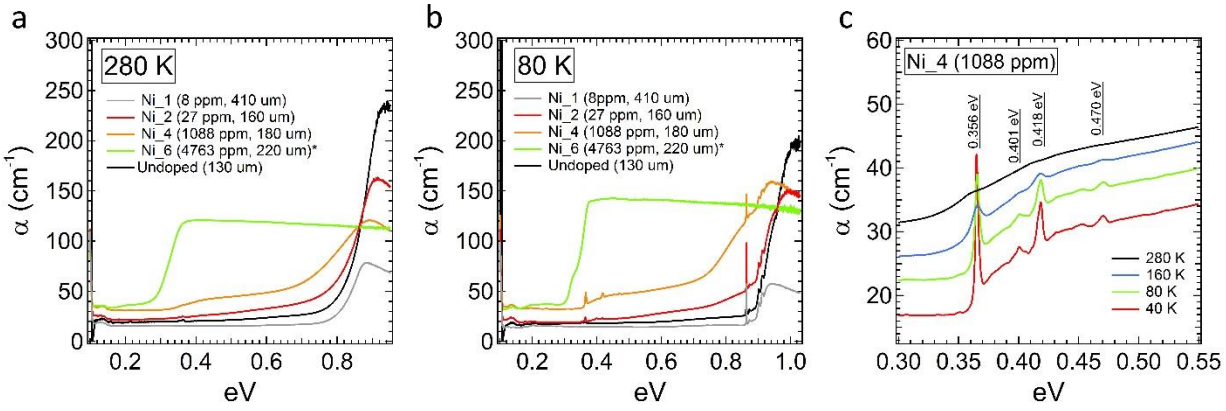

Figure 5.10: Optical absorption spectra of Ni-doped pyrite single crystals. All crystals are DSP fine polished. The absorption coefficient for each slab is calculated based on their optical extinction measured by the FTIR. (a) and (b) Calculated absorption coefficient at 280 K and 80 K, respectively. The black curve represents an undoped crystal (Ni < 1 ppm). The concentration of Ni is in ppm atomic, as it was reported in Table 5.2. It has to be noted that the yellow curve is the spectra of Ni_6 crystal which had phase impurities. It seems like that the band gap has become narrower for this crystal (E_g~0.3 eV, similar to the band gap of NiS_2) (c) Calculated absorption coefficient for Ni_4 slab at different temperatures. The optical transitions between 0.35-0.45 eV become more intense as the temperature goes down.

Ni incorporation has resulted in the formation of a set of absorption peaks around 0.4 eV. As the temperature decreases the peaks become sharp and can be distinguished from each other. At the same time, a broad absorption is visible at high energies. By comparing the absorption coefficient of the undoped crystal between 0.6 eV and 0.8 eV, the broad feature can be easily identified. The spectra of the Ni_6 sample is completely absorbing at energies above 0.3 eV. It

seems that the band gap of this sample has been reduced, and has become comparable to the reported band gap of NiS_2 due to the presence of impurity phases.

5.3.4 Magnetic

Induced magnetic moments at different fields for Ni-doped crystals have been measured to calculate the spin state of the incorporated nickel atoms in pyrite (like the cobalt case). Figure 5.11 shows induced mass magnetization and the corresponding molar susceptibility of Ni_5 crystal. Unlike undoped and Co- doped crystals, the Ni-doped crystals exhibited a paramagnetic response at higher temperatures, and the magnitude of the paramagnetic susceptibility was much larger than the paramagnetic susceptibility of the undoped crystals. The unpaired electrons of nickel are the reason behind the paramagnetic susceptibility. Table 5.3 shows the corresponding effective magnetic moment and oxidation state of nickel centers. Nickel has a d^8 electron configuration in pyrite (+2 oxidation state). Ni-doped crystals exhibit Curie-Weiss paramagnetism. Based on the figure 5.11b, the inverse of molar susceptibility increases linearly with increasing temperature, which is the characteristic of Curie-Weiss paramagnetism.

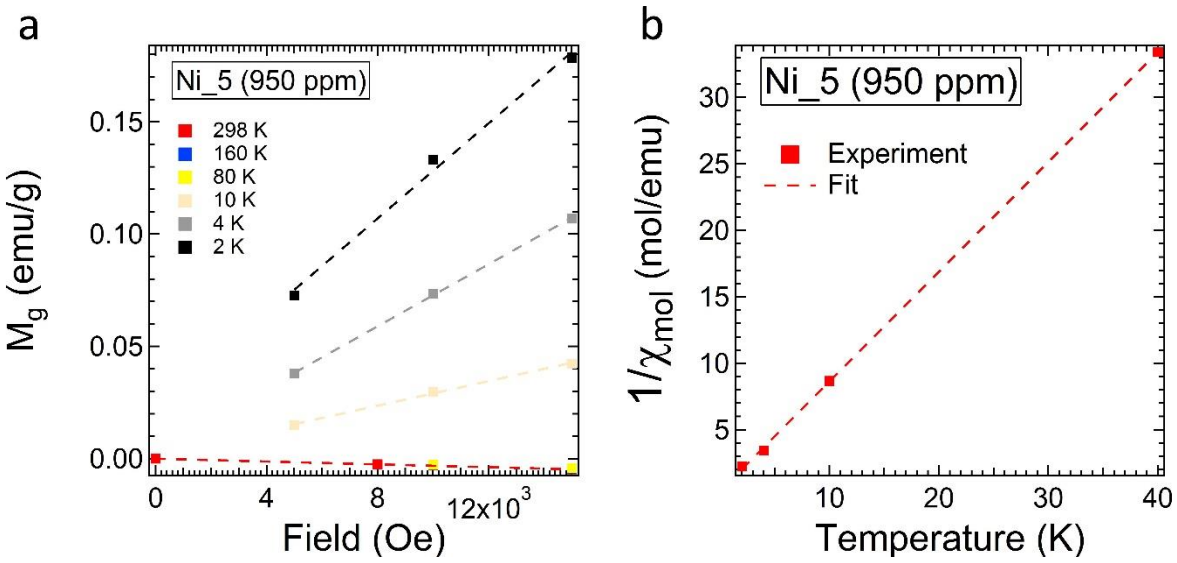

Figure 5.11: Magnetic properties of Ni-doped crystals. (a) Induced mass magnetization (M_g) at different fields, showing a positive paramagnetic behavior at temperatures below 80 K. The dotted lines are the fit to the magnetization. (b) Inverse molar susceptibility of Ni_5 crystal with respect to temperature. The linear fit suggests a Curie-Weiss paramagnetism (Fit equation = y =0.38055 + 0.82562x).

Table 5.3: Spin state of nickel in Ni-doped crystals.

Sample	Temp. (K)	Ni conc. (ppm wt)	χ_m (emu/mol)	μ_{eff} (B.M.)	e^- config.	Oxidation state
Ni_5	40	1390	0.03	3.09	d^8	2
	10		0.12	3.04		
	4		0.29	3.05		
	2		0.45	2.67		

5.3.5 Electrical

The electrical properties of the Ni-doped crystals were measured by temperature-dependent conductivity and Hall effect. The negative sign of the Hall coefficient indicated that nickel is a n-type dopant. The conductivity and the Hall coefficient of the doped crystals resemble the undoped crystals, and they can be fitted with the same fitting parameters (figure 5.12). The

conductivity at low temperatures is still dominant by the surface layer, and Ni doping has not had any effect on the surface inversion layer. The increase in the concentration of nickel has resulted in the slight increase in the conductivity in Ni_1 and Ni_3 crystals due to the increase of bulk electron concentration. However, Ni_4 shows a slightly different conductivity behavior (different activation energy at temperature > 180 K). The temperature-dependent conductivity of this crystal follows the temperature-dependent conductivity of Ni_5 and Ni_6 crystals which had phase impurities (graph not shown). Therefore, a possible reason for the different conductivity behavior of Ni_4 sample can be due to the presence of phase impurities which were below the detection limit of the synchrotron XRD.

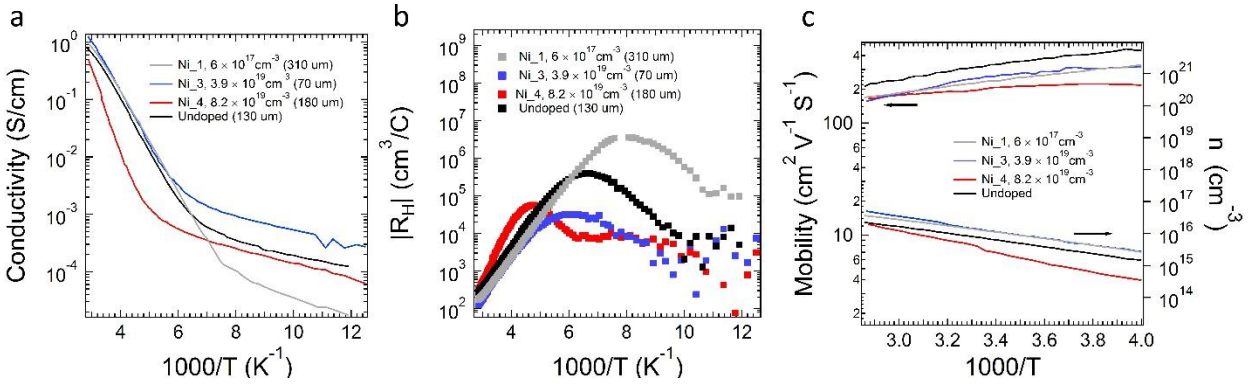

Figure 5.12: Electrical properties of Ni-doped crystals. All reported crystals were fine polished, and colloidal silver was used to make ohmic contacts to them. (a) Temperature-dependent conductivity data for Ni-doped crystals and an undoped crystal (as a reference). (b) Temperature dependent Hall coefficient of the Ni-doped crystals. Due to thickness variations and the surface quality of the crystals, the turn-over happens at different temperatures. (c) bulk electron (n_b) carrier concentration and mobility calculated based on the Hall coefficient and the conductivity in the unipolar region.

5.3.6 Summary

Systematic spin-polarized DFT were performed to investigate the effect of Ni on the bulk electronic and optical properties of pyrite and to complement the findings of the experiment. A 3 × 3 × 3 supercell was analyzed with the addition of Ni atoms (0.9%).

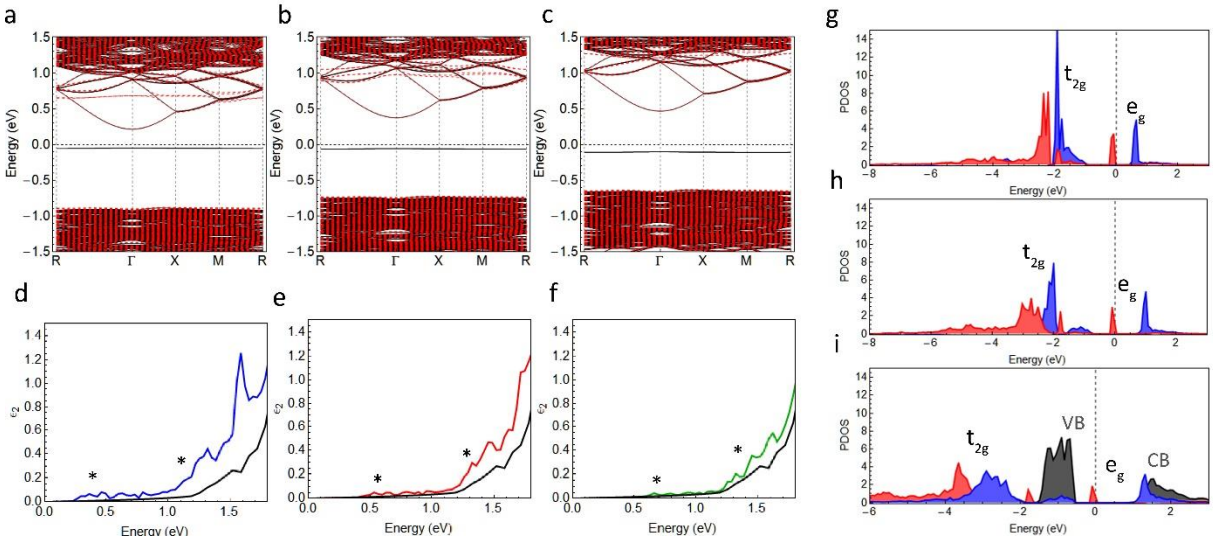

Figure 5.13: Effect of Ni doping based on DFT calculations (GGA + U). (a), (b), and (c) band structures of a 3 × 3 × 3 supercell of pyrite doped with Ni by assuming 0 eV, 2 eV, and 4 eV as the U value, respectively. The doping amount corresponds to Co concentration of 6.8×10^{20} cm^{-3}. The horizontal dotted lines at 0 eV indicate the position of the Fermi level. The induced energy state due to Ni is represented by the black solid line. The donor states are located in the middle of the gap. (d), (e), and (f) imaginary part of the dielectric constant for U = 0 eV, U = 2 eV, and U = 4 eV, respectively. The stars indicate the energies that the optical absorptions should take place. (g), (h), and (i) DOS of a 2 × 2 × 2 supercell of pyrite doped with Ni by assuming 0 eV, 2 eV, and 4 eV as the U value, respectively. CB and VB states (gray)are indicated in (i) and are representative in (g) and (h) as well. The vertical dotted lines show the location of the Fermi level. Red and blue corresponds to up and down spins.

Figure 5.13 summarizes the calculation. Band structure, density of states (DOS) and the imaginary part of the dielectric constant (representative of the energy position of expected optical absorption transitions) were calculated based on different values of U (0 eV, 2 eV, and 4 eV).

U values equal to 0 and 2 eV can predict the experimental results more accurately. Nickel introduces a state around 0.4 eV below the CB. The state is below the Fermi level and is partially filled. The observed optical transitions observed in figure 5.10 are from this state to the conduction band. The broad absorption feature at higher energies is also predicted by the calculations (figure 5.13e).

In conclusion, by combining all the experimental and theoretical results, the role of Ni doping in pyrite can be explained. Ni introduces a deep donor state about 0.4 eV under the CB. Since it is a deep donor, it is not ionized at most of the temperatures and does not contribute to the conductivity. That's why the electronic properties of Ni-doped and undoped crystals were very similar. The states are observable with optical transmission measurements. Electrons in these states get excited to the conduction band by absorbing energies ~0.4 eV. Future photoconductivity measurements can confirm our findings. The conductivity of the crystal should be increased by photoexciting the electrons in these states.

5.4 Chromium

Chromium sulfide compounds do not crystallize in the pyrite structure. $CrSb_2$ is one of the few chromium compounds in which chromium senses an octahedral anion coordination and has

marcasite structure. [99] CrS_x compounds depending on their composition exhibit varying structures with unique electrical and magnetic properties. As an example, $CrS_{1.5}$ is reported to be ferrimagnetic with a semiconducting electrical property. [112- 114] Cr has been present in most of synthetic and natural pyrite crystals as an impurity (Cr is present as an impurity along most iron precursors). Therefore, understanding the effect of it on the electronic properties of pyrite is important. Siebert et al., [115] has reported that Cr^{+3} and Cr^{+1} paramagnetic centers are present as substitutional dopants in CVT-grown pyrite. The observed paramagnetism of pyrite crystals was attributed to these impurity centers. At the same time, Cr^{+3} centers in pyrite have been identified as the source of observed high energy (0.86 eV) optical transitions in pyrite. [98] Since Cr is present in our flux-grown crystals (its concentration depends on the concentration of Cr in the iron precursor), and the high energy optical transitions is also observed in our crystals (see Section 4.1.5 for details), the effect of Cr doping was studied in this work with the same approach of the other two dopants (Co and Ni).

Dissolving elemental chromium in hydrazine or other solvents proved to be challenging. Therefore, Chromium (III) nitrate nonahydrate (99.99%) was dissolved in semiconducting grade methanol. The solution containing minuscule amounts of Cr was then added to iron in alumina crucibles (in the same way as Co and Ni doping). Sulfur and sodium sulfide were added to the crucible after evaporating the solvent in a furnace. The rest of the crystal making characterization methods were the same as the other doped (Co and Ni) crystals.

5.4.1 Elemental

ICP-MS was used to quantify the concentration of Cr in the Cr-doped crystals. Doped crystals were sectioned parallel to the top facet with a slow diamond saw; then each section was dissolved in nitric acid, and measured with ICP-MS. The concentration of Cr was measured in each section to investigate the possibility of any concentration gradient from a top facet of crystal to a bottom part of the crystal. Table 5.4 shows the measured concentration of chromium in different crystals.

Table 5.4: Concentration of Cr in $Fe_{(1-x)}Cr_{(x)}S_2$ crystals

Sample	Section	ppm at	cm^{-3}	Composition (x)
Cr_1	Center slab	39.4	2.97×10^{18}	0.00012
Cr_2	1a	410.6	3.11×10^{19}	0.00123
	1b	465.1		
	2a	293.8		
	2b	438.3		
	3a	436.3		
	3c	423.8		
Cr_3	Whole	552	4.17×10^{19}	0.0016
Cr_4	Whole	869	6.5×10^{19}	0.002
Cr_5	Whole	5187	3.91×10^{20}	0.015

Whole = a whole small crystal was measured (no sectioning). Center = a section in the middle of the crystal. Section 1 refers to the top of the crystal and section 3 to the bottom of the crystal (a and b refers to pieces of the crystal in the same z-section, they were measured to check for homogeneity in the xy plane.). The concentration (cm^{-3}) and the composition columns are average amounts considering the whole crystal. Each section is around 500 microns thick.

Measuring the concentration of Cr with ICP-MS can be challenging due to the presence of polyatomic interferences. 5-10% error in the reported values is expected. No apparent

concentration gradient was observed in the measured samples. Cr doping did not result in any unintentional doping of other elements.

5.4.2 Structural

Chromium doping produced highly-faceted crystals like undoped cases in most cases. No apparent differences were observed between Cr-doped crystals and undoped crystals. High-resolution synchrotron powder XRD was used to check for phase purity. Cr_1, Cr_2, and Cr_5 crystals were measured with synchrotron XRD. The XRD pattern showed no trace of other crystalline or amorphous phases for any of them. Figure 5.14 shows the XRD pattern of the Cr_5 which had the highest concentration of Cr. All the peaks are indexed to pyrite. Shifting of the diffraction peaks to smaller 2θ angles as the Cr concentration increases suggests that Cr incorporation in the lattice results in lattice constant expansion (Figure 5.14b).

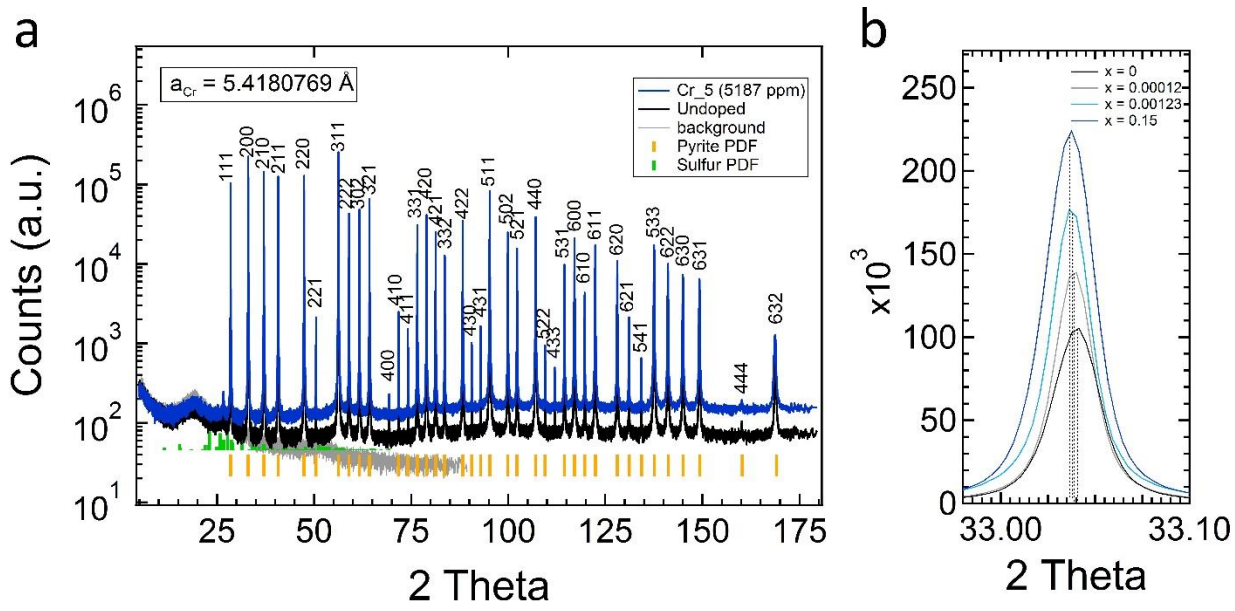

Figure 5.14: Synchrotron XRD pattern of a powdered Cr-doped crystal on a log scale. (a) Powders were made from the crystals of batch "Cr_5" with expected concentration of Cr to be ~5187 ppm atomic. All 39 reflections index to pyrite and no other phases are detected. The Lattice parameter was calculated by Rietveld refinement with PDXL2 software at room temperature. The pattern for an undoped crystal (black) is shown for comparison. The background pattern is for an empty capillary tube. Small yellow bars near the x-axis denote the pyrite reference peaks. (b) Peak shift (to the left) of the (200) planes as the concentration of Cr increases in $Fe_{(1-x)}Cr_{(x)}S_2$. The vertical dotted lines show the center of the peaks.

5.4.3 Optical

The optical absorbance spectra of the Cr-doped crystals were measured by the FTIR in the transmission geometry. Figure 5.15 shows the calculated optical absorption coefficient of the Cr-doped crystals in the Mid-IR energy range.

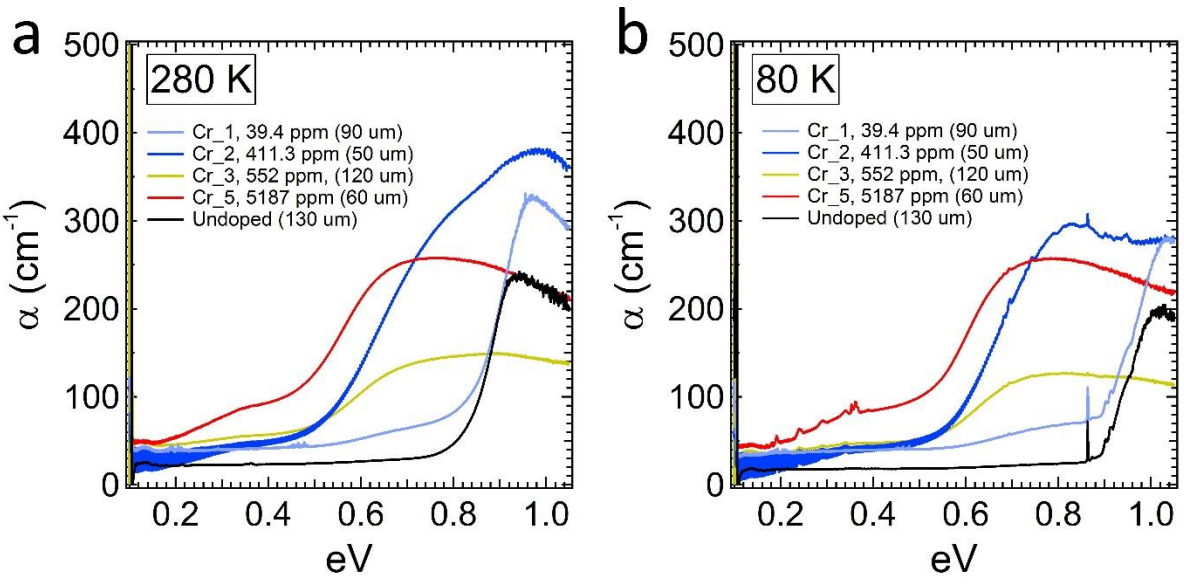

Figure 5.15: Optical absorption spectra of Cr-doped pyrite single crystals. All crystals are DSP fine polished. The absorption coefficient for each slab is calculated based on their optical extinction measured by the FTIR. (a) and (b) Calculated absorption coefficient at 280 K and 80 K, respectively. The black curve represents an undoped crystal. Elemental Cr in the powder form was used as the source of Cr in the growth process for Cr_3 instead of Chromium (III) nitrate nonahydrate, to make sure that the observed features are not due to nitrogen or oxygen.

Cr addition mainly introduces a broad absorption feature at high energies below the band edge. As the concentration of Cr increases, this feature becomes more absorbing and broader. Set of peaks also starts to appear at between 0.2 eV and 0.4 eV in the highly doped crystals. Unlike the claim of Yu et al., [98] the peak at 0.86 eV is not related to the concentration of Cr. The peak intensity should have been increased if chromium centers were the cause of it. The peak at 0.86 eV is not easily observable in the heavily doped crystals since the crystals are highly absorbing at energies above 0.6 eV in these crystals, which results in the saturation of the FTIR's detector.

5.4.4 Magnetic

Induced magnetic moments at different fields for Cr-doped crystals have been measured to calculate the spin state of the incorporated Cr atoms in pyrite (like the Ni case). Like the Ni-doped crystals, Cr incorporation in pyrite results in a positive molar susceptibility indicative of paramagnetism. The unpaired electrons of Cr are the reason behind this paramagnetic susceptibility. Table 5.5 shows the corresponding effective magnetic moment and oxidation state of Cr centers in the measured crystals.

Table 5.5: The Spin state of Cr in Cr-doped crystals.

Sample	Temperature (K)	Cr conc. (ppm wt)	χ_m (emu/mol)	μ_{eff} (B.M.)	e^- config.	Oxidation state
Cr_5	40	6780	0.0417	3.65	d^3	3
Cr_4	40	1130	0.0460	3.84	d^3	3
Cr_3	40	718	0.0301	3.11	d^4	2
Cr_2	2	610	0.8897	3.77	d^3	3

In all of the measured samples (except Cr_3), Cr has the oxidation state of +3 in pyrite. However, the effective magnetic moment in Cr_3 sample is smaller and corresponds to a low-spin d^4 electron configuration. Cr_3 crystal is the one that Cr was added as elemental Cr to the flux instead of Chromium (III) nitrate nonahydrate. A Different source for Cr or errors in measuring the concentration of Cr might be the cause of the discrepancy. Measuring the exact concentration of Cr in the Cr_3 crystal that has been measured for the magnetic properties

should give us a definitive answer. Based on the reported results in Table 5.5, it is not possible to definitively know if the the oxidation state of Cr in pyrite is 2, 3, or a combination of both.

5.4.5 Electrical

The electrical properties of the Cr-doped crystals were measured by temperature-dependent conductivity and Hall effect (Figure 5.16).

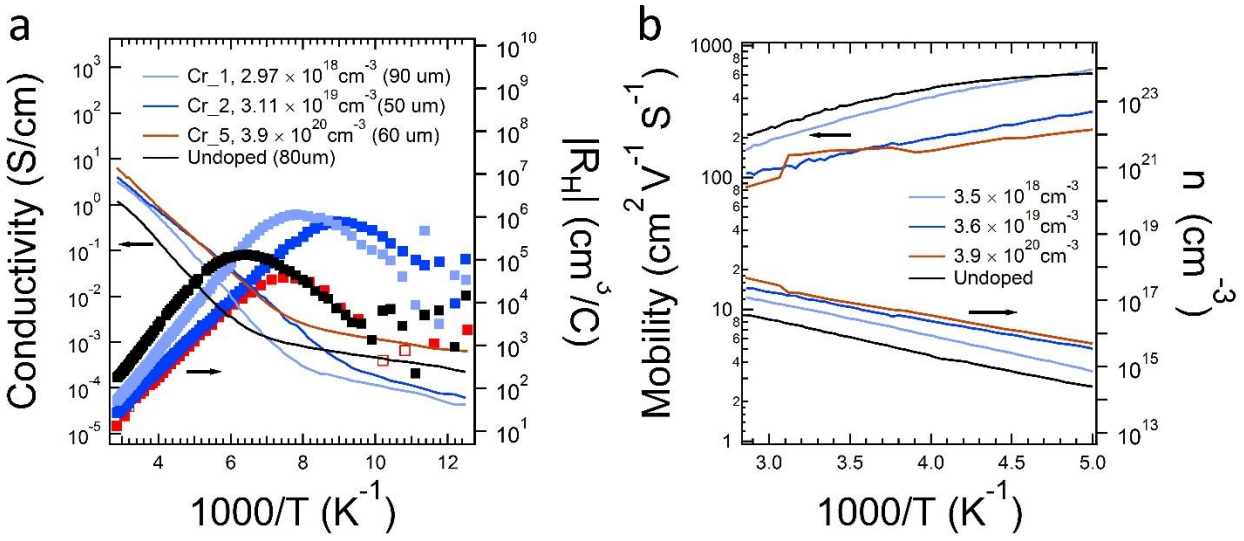

Figure 5.16: Electrical properties of Cr-doped crystals. All reported crystals were fine polished, and colloidal silver was used to make ohmic contacts to them. (a) Temperature-dependent conductivity and Hall effect data. (b) bulk electron (n) carrier concentration and mobility calculated based on the Hall coefficient and the conductivity in the unipolar region.

The doped crystals are remained n-type by Cr doping. The conductivity and the Hall coefficient of the doped crystals resemble the undoped crystals, and they can be fitted with the same fitting parameters (figure 5.16). Even having chromium with a high density in pyrite (3.9×10^{20} cm^{-3}) has

not resulted in drastic changes in the electrical behavior of the crystals. The bulk electron concentration of the crystals has increased as the amount of chromium has increased while the Hall electron mobility has remained fairly the same.

5.4.6 Summary

It is concluded that Cr cannot be responsible for the high energy optical transitions observed around 0.86 eV. The real reason responsible for that optical transition still remains unknown. Understanding the real effect of Cr on pyrite still cannot be fully described by the current experiments. Based on the discussed results several possibilities of the actual role of Cr in pyrite can be proposed.

It has been shown that Cr can dope pyrite without causing any phase segregation. Cr-doped pyrite crystals are paramagnetic due to the presence of Cr^{2+} or Cr^{3+} centers. Although clear sub-gap optical absorption features are formed due to Cr, no significant effect is observed on the electrical properties of the doped crystals. Scenarios that can explain such a situation are as follow. First, Cr might be introducing deep donor states (0.7-0.8 eV below the CB). The presence of such donor states cannot change the conductivity of the sample, but optical transitions from those states to the CB can take place, and cause the formation of broad optical features at high energies. Photoconductivity measurements can test this hypothesis. If the hypothesis is correct, the conductivity of the doped crystal should increase by shining light on the crystal with the energies below the band gap of pyrite. Second, Cr might be narrowing the band gap by

introducing states that overlap with the CB and extends to the gap of pyrite. Lastly, the observed optical features might be only due to d-transitions, which in that case no effect on the conductivity would be expected. Investigating the effect of Cr with DFT can be very beneficial (like the Co and Ni case), and give the clear answer.

Chapter 6

Summary and Future Work

Pyrite thin films were made by CVD for application in solid-state p-n junctions. Annealing in a sulfur atmosphere was needed to convert the mixed phase films (pyrite and marcasite) to phase pure pyrite films. The effect of marcasite impurity on the band gap of pyrite was investigated through careful optical absorption experiments and DFT calculations. The band gap of films with a substantial amount of marcasite (> 50%) was comparable to the band gap of phase pure pyrite films, indicating that contrary to the general belief, the band gap of marcasite is not smaller than pyrite.

Thin films were p-type (unlike n-type single crystals), highly conductive, and had low hole mobilities based on temperature-dependent Hall effect and conductivity measurements. The CVD-grown thin films were used as absorber layers in solid-state p-n junctions. Despite challenging fabrication steps and reproducibility problems, FeS_2/ ZnS junctions with high rectifications were made. The solid-state junctions had high photo-voltage with small photo-currents. The low currents were attributed to the high recombination velocities at the interface and/or conduction band offset between the FeS_2 and the ZnS layers. To enhance the device performance of the p-n junctions, the surface of pyrite needs to be passivated. A proper

passivation treatment could potentially passivate the surface states, unpin the Fermi level at the surface, and reduce surface recombnation velocities.

Pyrite single crystals were grown by using Na_2S as the flux. The flux-grown pyrite single crystals are the purest synthetic pyrite crystals reported to date. They were used as a model system to understand optical, electronic, and magnetic properties of pyrite. Pyrite crystals were diamagnetic, and the optical band gap of pyrite was measured to be ~0.95 eV. Based on the temperature-dependent Hall effect and conductivity measurements, it was concluded that pyrite has an n-type bulk with a p-type surface. The charge transport is dominated by the ionization of bulk donors at most temperatures (> 120 K) before the surface holes start to dominate the transport at low temperatures. The Fermi level has been pinned ~100 meV from the valence band edge at the surface (based on the UPS results). Surface states (most likely uncoordinated iron at the surface) are responsible for the Fermi level pinning and causing a formation of an inversion layer on the surface. Proper passivation can eliminate the inversion layer by passivating the states that have caused the pinning of the Fermi level. A comparative study involving an XPS/ UP, Hall effect and DFT calculations on the effect of various passivation treatments on the properties of the surface layer is essential in the future. The most effective passivation treatment can then be applied to the thin films.

Low photo-voltage of the reported pyrite devices are attributed to the trap-assisted tunneling at the surface. Ionization of the bulk donors at the surface (due to the band bending caused by the surface inversion layer) will result in the generation of a narrow triangular potential barrier. Majority carriers can easily tunnel through this barrier and thereby lose part of the built-in

potential. To increase the photo-voltage, the density of the bulk defects (responsible for the formation of the triangular barrier) should be reduced. The lower density of bulk defect states will result in a more gradual band bending at the surface, which will reduce the amount of the tunneling losses.

Growing the crystals with a lower cooling rate (slow-cooled crystals) resulted in obtaining pyrite single crystals with lower conductivity due to the reduction in the density of the bulk native defects while retaining the same structural quality and elemental purity of the standard crystals. Band diagram calculation proved that such a reduction in the bulk donor density could indeed boost the photo-voltage accessible to pyrite devices above 250 meV.

Making Schottky metal junctions and wet-junctions with the slow-cooled crystals is an important step that should be pursued in the future. A comparative study of two identical solar devices, one made with a standard and the other made with a slow-cooled pyrite single crystal, can confirm the expected boost in the photo-voltage based on the theoretical calculations.

A detailed picture of the crystallographic defects in pyrite can be beneficial as well. Crystallographic defects (e.g., dislocations, stacking faults) can be the source of some of the observed electrical and optical properties in pyrites (e.g., the native bulk donors or the high energy optical transition peaks). High-resolution TEM imaging and diffraction studies could be used in the future to quantify the existence of any 1D, 2D, and 3D defects in the single crystals.

Controlling the Fermi level, tuning the carrier type and carrier concentration, manipulating the inversion layer, and gaining insight into the bulk defect chemistry of pyrite can be understood and studied by doping. Co, Cr, and Ni were selected as dopants due to their presence as an

impurity in most of the synthetic crystals. A comparative study involving ICP-MS, XRD, FTIR, Hall effect, MPMS, and theoretical DFT calculations was used to understand the effect of each dopant. While the role of Co and Ni is understood, a more detailed DFT calculations combined with photoconductivity measurements is needed to understand the effect of Cr on the optical and electronic properties of pyrite.

Overall, this work, while pointing out the challenges and problems associated with pyrite, shows a clear path forward to achieve high efficient pyrite solar devices. Passivation of the problematic surface states and reduction of native bulk defects can result in making pyrite solar devices with high photo-voltage.

References

[1] J. Conti, "International Energy Outlook 2016," U.S. Energy Information Administration, 2016.

[2] R. M. Nault, "Basic Research Needs for Solar Energy Utilization," Department of Energy, 2005.

[3] A. Gerlach, D. Schafer and J. Schmid, *Energy Conference and Exhibition (EnergyCon), 2010 IEEE International,* pp. 406-4011, 2010.

[4] C. Wadia, P. Alivisatos and D. Kammen, *Environ. Sci. Technol.,* vol. 43, no. 6, pp. 2072-2077, 2009.

[5] E. K. Li, K. H. Johnson, D. E. Eastman and J. L. Freeouf, *Physical Review Letters,* vol. 32, p. 470, 1974.

[6] A. Fujimori, K. Mamiya, T. Mizokawa, T. Miyadai, T. Sekiguchi, H. Takahashi, N. Môri and S. Suga, *Physical Review B,* vol. 54, p. 16329, 1996.

[7] H. W. Nesbitt, A. G. Berlich, S. L. Harmer, I. Uhlig, G. M. Bancroft and R. Szargan, *American Mineralogist,* vol. 89, p. 382, 2004.

[8] J. F. W. Mosselmans, R. A. D. Pattrick, G. Laan, J. M. Charnock, D. J. Vaughan, C. M. B. Henderson and C. D. Garner, *Physics and Chemistry of Minerals,* vol. 22, p. 311, 1995.

[9] K. C. Prince, M. Matteucci, K. Kuepper, S. G. Chiuzbaian, S. Bartkowski and M. Neumann, *Physical Review B,* p. 085102, 2005.

[10] K. M. Rosso, U. Becker and M. F. Hochella, *American Mineralogist,* vol. 84, p. 1535, 1999.

[11] T. A. Bither, R. J. Bouchard, W. H. Cloud, P. C. Donohue and W. J. Siemons, *Inorganic Chemistry,* vol. 7, p. 2208, 1968.

[12] W. Folkerts, G. A. Sawatzky, C. Haas, R. A. d. Groot and F. U. Hillebrecht, *Journal of Physics C: Solid State Physics,* vol. 20, p. 4135, 1987.

[13] P. Raybaud, G. Kresse, J. Hafner and H. Toulhoat, *Journal of Physics: Condensed Matter,* vol. 9, p. 11085, 1997.

[14] V. Eyert, K. H. Hock, S. Fiechter and H. Tributsch, *Physical Review B,* vol. 57, p. 6350, 1998.

[15] G. U. v. Oertzen, W. M. Skinner and H. W. Nesbitt, *Physical Review B,* p. 235427, 2005.

[16] A. Ennaoui, S. Fiechter, W. Jaegermann and H. Tributsch., *Journal of The Electrochemical,* vol. 133, no. 1, p. 97, 1986.

[17] P. P. Altermatt, T. Kiesewetter, K. Ellmer and H. Tributsch, *Solar Energy Materials and Solar Cells,* vol. 71, p. 181, 2002.

[18] A. Ennaoui and H. Tributsch, *Journal of Electroanalytical Chemistry,* vol. 204, p. 185, 1986.

[19] G. Smestad, A. Ennaoui, S. Fiechter, H. Tributsch, W. K. Hofmann, M. Birkholz and W. Kautek, *Solar Energy Materials,* vol. 20, p. 149, 1990.

[20] A. Ennaoui, G. Smestad and H. Tributsch, in *World Renewable Energy Congress. Energy and the Environment, Pergamon Press*, Oxford, 1990.

[21] A. Ennaoui, G. Schlichthörl, S. Fiechter and H. Tributsch, *Solar Energy Materials and Solar Cells,* vol. 25, p. 169, 1992.

[22] G. Chatzitheodorou, S. Fiechter, R. Könenkamp, M. Kunst, W. Jaegermann and H. Tributsch, *Materials Research Bulletin,* vol. 21, p. 1481, 1986.

[23] G. Smestad, A. d. Silva, H. Tributsch, S. Fiechter, M. Kunst, N. Meziani and M. Birkholz, *Solar Energy Materials,* vol. 18, p. 299, 1999.

[24] Y. Lin, D. Y. Wang, H. C. Yen, H. L. Chen, C. C. Chen, C. M. Chen, C. Y. Tang and C. W. Chen, *Nanotechnology,* vol. 20, p. 405207, 2009.

[25] C. Steinhagen, T. B. Harvey, C. J. Stolle, J. Harris and B. A. Korgel, *The Journal of Physical Chemistry Letters,* vol. 3, p. 2352, 2012.

[26] A. Ennaoui and H. Tributsch, *Solar Energy Materials,* vol. 14, p. 461, 1986.

[27] B. Thomas, C. Hoepfner, K. Ellmer, S. Fiechter and H. Tributsch, *Journal of Crystal Growth,* vol. 146, pp. 630-635, 1995.

[28] Y. Tomm, R. Schieck, K. Ellmer and S. Fiechter, *Journal of Crystal Growth,* vol. 146, pp. 271-276, 1995.

[29] M. Limpinsel, N. Farhi, N. Berry, J. Lindemuth, C. L. Perkins, Q. Lin and M. Law, *Energy and Environmental Science,* vol. 7, pp. 1974-1989, 2014.

[30] M. Bronold, C. Pettenkofer and W. Jaegermann, *J. Appl. Phys,* vol. 76, p. 5800, 1994.

[31] I. J. Ferrer and C. Sanchez, *Journal of Applied Physics,* vol. 170, p. 2641, 1991.

[32] C. d. l. Heras, J. L. d. Vidales, I. J. Ferrer and C. Snchez, *Journal of Materials Research,* vol. 11, p. 211, 1996.

[33] L. Meng, J. P. Tu and M. S. Liu, *Materials Letters,* vol. 38, p. 103, 1999.

[34] D. Y. Wan, Y. T. Wang, B. Y. Wang, C. X. Ma, H. Sun and L. Wei, *Journal of Crystal Growth,* vol. 253, p. 230, 2003.

[35] A. Pascual, J. R. Ares, I. J. Ferrer and C. R. Sanchez, *Applied Surface Science,* vol. 234, p. 355, 2004.

[36] D. Lichtenberger, K. Ellmer, R. Schieck, S. Fiechter and H. Tributsch, *Thin Solid Films,* vol. 246, pp. 6- 12, 1994.

[37] A. Baruth, M. Manno, D. Narasimhan, A. Shankar, X. Zhang, M. Johnson, E. S. Aydil and C. Leighton, *Journal of Applied Physics,* vol. 112, p. 54328, 2012.

[38] D. Lichtenberger, K. Ellmer, R. Schieck and S. Fiechter, *Applied Surface Science,* Vols. 70-71 (part 2), p. 583, 1993.

[39] G. Willeke, R. Dasbach, B. Sailer and E. Bucher, *Thin Solid Films,* vol. 213, p. 271, 1992.

[40] M. Birkholz, D. Lichtenberger, C. Hopfner and S. Fiechter, *Solar Energy Materials and Solar Cells,* vol. 27, p. 243, 1992.

[41] D. Susac, L. Zhu, M. Teo, A. Sode, K. C. Wong, P. C. Wong, R. R. Parsons, D. Bizzotto, K. A. R. Mitchell and S. A. Campbell, *Journal of Physical Chemistry,* vol. C 111, p. 18715, 2007.

[42] A. Yamamoto, M. Nakamura, A. Seki, E. L. Li, A. Hashimoto and S. Nakamura, *Solar Energy Materials and Solar Cells,* vol. 75, p. 451, 2003.

[43] C. Delasheras, I. J. Ferrer and C. Sanchez, *Journal of Physics-Condensed Matter,* vol. 6, p. 10177, 1994.

[44] E. L. Li, S. Seki and A. Yamamoto, *Semiconductor Photonics and Technology,* vol. 7, p. 89, 2001.

[45] D. M. Schleich and H. S. W. Chang, *Journal of Crystal Growth,* vol. 112, p. 737, 1991.

[46] K. Ellmer, D. Lichtenberger, A. Ennaoui, C. Hopfner, S. Fiechter and H. Tributsch, *In Photovoltaic Specialists Conference, Conference Record of the Twenty Third IEEE,* p. 535, 1993.

[47] C. Hopfner, K. Ellmer, A. Ennaoui, C. Pettenkofer, S. Fiechter and H. Tributsch, *Journal of Crystal Growth,* vol. 151, p. 325, 1995.

[48] B. Thomas, K. Ellmer, M. Mller, C. Hpfner, S. Fiechter and H. Tributsch, *Journal of Crystal Growth,* vol. 170, p. 808, 1997.

[49] B. Thomas, T. Cibik, C. Hopfner, K. Diesner, G. Ehlers, S. Fiechter and K. Ellmer, *Journal of Materials Science-Materials in Electronics,* vol. 9, p. 61, 1998.

[50] N. Takahashi, T. Sawada and T. Nakamura, *Journal of Materials Chemistry,* vol. 10, p. 2346, 2000.

[51] N. Takahashi, Y. Nakatani, T. Yatomi and T. Nakamura, *Chemistry of Materials,* vol. 15, p. 1763, 2003.

[52] J. Hu, Y. Zhang, M. Law and R. Wu, *Physical Review B,* vol. 85, p. 085203, 2012.

[53] K. T. Wilke, D. Schultze and K. Tpfer, *Journal of Crystal Growth,* vol. 1, p. 141, 1967.

[54] J. G. Fleming, *Journal of Crystal Growth,* vol. 92, p. 287, 1988.

[55] S. W. Lehner, K. S. Savage and J. Ayers, *Journal of Crystal Growth,* vol. 286, p. 306, 2006.

[56] G. Willeke, O. Blenk, C. Kloc and E. Bucher, *Journal of Alloys and Compounds,* vol. 178, p. 181, 1992.

[57] S. W. Lehner, N. Newman, M. v. Schilfgaarde, S. Bandyopadhyay, K. Savage and P. R. Buseck, *J. Appl. Phys.,* vol. 111, p. 083717, 2012.

[58] R. Schieck, A. Hartmann, S. Fiechter, R. Konenkamp and H. Wetzel, *Journal of Materials Research,* vol. 5, p. 1567, 1990.

[59] C. Kloc, G. Willeke and E. Bucher, *Journal of Crystal Growth,* vol. 131, p. 448, 1993.

[60] C. H. Ho, M. H. Hsieh and Y. S. Huang, *Journal of the Electrochemical Society,* vol. 155, p. H254, 2008.

[61] N. Berry, M. Cheng, C. L. Perkins, M. Limpinsel, J. C. Hemminge and M. Law, *Adv. Energy Mater.,* vol. 2, p. 1124, 2012.

[62] H. Scheel, *Journal of crystal growth,* vol. 24, p. 669, 1974.

[63] J. Sangster and A. D. Pelton, *Journal of phase equilibria,* vol. 189, p. 89, 1997.

[64] "Magnetron Sputtering," [Online]. Available: http://www.hauzertechnocoating.com/en/plasma-coating-explained/magnetron-sputtering/. [Accessed 09 11 2016].

[65] M. Limpinsel, "Iron pyrite absorber for solar photovoltaic energy conversion," 2015.

[66] R. L. Petritz, *Phys. Rev,* vol. 110, p. 1254, 1958.

[67] S. M. Sze and K. K. Ng, Physics of Semiconductor Devices, New York: Wiley, 2007.

[68] W. W. Kou and M. S. Seehra, *Phys. Rev. B: Condens. Matter Mater. Phys.,* vol. 18, p. 7062, 1978.

[69] A. M. Karguppikar and A. G. Vedeshwar, *Phys. Status Solidi A,* vol. 109, p. 549, 1998.

[70] B. Thomas, K. Diesner, T. Cibik and K. Ellmer, *Solid State Phenomena,* vol. 51, p. 301, 1996.

[71] R. Sun, M. Chan and G. Ceder, *Physical Review B,* vol. 83, p. 235311, 2011.

[72] S. Seefeld, M. Limpinsel, Y. Liu, N. Farhi, Y. N. Zhang, N. Berry, Y. J. Kwon, C. L. Perkins, J. C. Hemminger, R. Q. Wu and M. Law, *Journal of the american chemical society,* vol. 135, p. 4412, 2013.

[73] J. Sangster and P. A.D., *J. Phase Equilib.,* vol. 18, p. 82, 1997.

[74] C. Jacoboni, C. Canali, G. Ottaviani and A. A. Quaranta, *Sold State Electron,* vol. 20, p. 77, 1997.

[75] M. Bronold, K. Büker, S. Kubala, C. Pettenkofer and H. Tributsch, *Phys. Status Solidi A,* vol. 135, p. 231, 1993.

[76] M. Bronold, Y. Tomm and W. Jaegermann, *Surf. Sci.,* vol. 314, p. L931, 1994.

[77] L. P. Yu, S. Lany, R. Kykyneshi, V. Jieratum, R. Ravichandran, B. Pelatt, E. Altschul, H. A. S. Platt, J. F. Wager, D. A. Keszler and A. Zunger, *Adv. Energy Mater.,* vol. 1, p. 748, 2011.

[78] T. Thio and J. W. Bennett, *Phys. Rev. B: Condens. Matter Mater. Phys.,* vol. 50, p. 10574, 1994.

[79] R. E. Jones, K. M. Yu, S. X. Li, W. Walukiewicz, J. W. Ager, E. E. Haller, H. Lu and W. J. Schaff, *Phys. Rev. Lett., 2006, 96, 125505,* vol. 96, p. 125505, 2006.

[80] P. D. C. King, T. D. Veal and C. F. McConville, *J. Phys.: Condens. Matter,* vol. 21, p. 174201, 2009.

[81] Y. N. Zhang, J. Hu, M. Law and R. Q. Wu, *Phys. Rev. B: Condens. Matter Mater. Phys.,* vol. 85, p. 085314, 2012.

[82] F. W. Herbert, A. Krishnamoorthy, K. J. V. Vliet and B. Yildiz, *Surf. Sci.,* vol. 618, p. 53, 2013.

[83] K. Waters, N. Rowson, R. Greenwood and A. Williams, *Separation and Purification Technology,* vol. 56, p. 9, 2007.

[84] P. Burgardt and M. Seehra, *Solid State Communications,* vol. 22, p. 153, 1977.

[85] H. Jarrett, W. Cloud, R. Bouchard, S. Butler, C. Frederick and J. Gillson, *Phys. Rev. Lett.,* vol. 21, p. 617, 1968.

[86] K. Waters, N. Rowson, R. Greenwood and A. Williams, *Minerals Engineering,* vol. 21, p. 679, 2008.

[87] P. Montano and M. Seehra, *Solid State Commun.,* vol. 20, p. 897, 1976.

[88] S. Choi, J. Hu, L. Abdallah, M. Limpinsel, Y. Zhang, S. Zollner, R. Wu and M. Law, *Physical Review B,* vol. 86, p. 115207, 2012.

[89] J. I. Pankove, Optical processes in semiconductors, Ney York: Dover publication, Inc., 1971.

[90] T.-R. Yang, J.-T. Yu, J.-K. Huang, S.-H. Chen, M.-Y. Tsay and Y.-S. Huang, *J. Appl. Phys.,* vol. 77, p. 1710, 1995.

[91] A. Schlegel and P. Wachter, *J. Phys. C: Solid State Phys.,* vol. 9, p. 3363, 1976.

[92] D. G. Thomas, J. J. Hopfield and C. J. Frosch, *Phys. Rev. Letters,* vol. 15, p. 857, 1965.

[93] F. A. Padovani and R. Stratton, *Solid-State Electron,* vol. 9, p. 695, 1966.

[94] N. Alonso-Vante, G. Chatzitheodrous, S. F. N. Mgoduka and H. T. I. Poulios, *Solar Energy Materials,* vol. 18, p. 9, 1988.

[95] K. Buker, N. Alonso-Vante and H. T. R. Scheer, *Ber. Bunsenges. Pys. Chem.,* vol. 98, p. 674, 1994.

[96] M. Cabán-Acevedo, N. S. Kaiser, C. R. English, D. Liang, B. J, Thompson, H.-E. Chen, K. J. Czech, J. C. Wright, R. J. Hamers and S. Jin, *J. Am. Chem. Soc.,* vol. 136, p. 17163, 2014.

[97] T. Kinner, K. P. Bhandari, E. Bastola, B. M. Monahan, N. O. Haugen, P. J. Roland, T. P. Bigioni and R. J. Ellingson, *J. Phys. Chem. C,* vol. 120, p. 5706, 2016.

[98] J. T. Yu, Y. S. Huang and M. Y. Tsay, *Journal of Applied Physics,* vol. 75, p. 5282, 1994.

[99] S. Ogawa, "J. Appl. Phys.," vol. 50, p. 2308, 1979.

[100] K. Sato, *Prog. Cryst. Growth Charact.,* vol. 11, p. 109, 1985.

[101] G. L. Zhao, J. Callaway and M. Hayashibara, *Phys. Rev. B,* vol. 48, p. 15781, 1993.

[102] S. R. Butler and R. J. Bouchard, *J. Cryst. Growth,* vol. 10, p. 163, 1971.

[103] R. N. Chandler and R. W. Bene, *Phys. Rev. B.,* vol. 8, p. 4979, 1973.

[104] S. Guo, D. P. Young, R. T. Macaluso, D. A. Browne, N. L. Henderson, J. Y. Chan, L. L. Henry and J. F. DiTusa, *Phys. Rev. B,* vol. 81, p. 144424, 2010.

[105] I. I. Mazin, *Appl. Phys. Lett.,* vol. 77, p. 3000, 2000.

[106] S. F. Cheng, G. T. Woods, K. Bussmann, I. I. Mazin, R. J. S. Jr., E. E. Carpenter, B. N. Das and P. Lubitz, *J. Appl. Phys.,* vol. 92, p. 6847, 2003.

[107] K. Ramesha, R. Seshadri, C. Ederer, T. Hes and M. A. Subramaniani, *Phys. Rev. B,* vol. 70, p. 214409, 2004.

[108] L. Wang, K. Umemoto, R. M. Wentzcovitch, T. Chen, C. L. Chien, J. G. Checkelsky, J. C. Eckert, E. D. Dahlberg and C. Leighton, *Phys. Rev. Lett.,* vol. 94, p. 056602, 2005.

[109] S. Guo, D. P. Young, R. T. Macaluso, D. A. Browne, N. L. Henderson, J. Y. Chan, L. L. Henry and J. F. DiTusa, *Phys. Rev. Lett.,* vol. 100, p. 017209, 2008.

[110] C. E. Housecroft and A. G. S. Chemistry, Inorganic Chemistry, Harlow: Prentice Hall, 2007.

[111] C. H. Ho, C. E. Huang and C. C. Wu, *J. Cryst. Growth,* vol. 270, p. 535, 2004.

[112] M. Mikami, K. Igahi and N. Ohashi, *J. Phys. Soc. Japan,* vol. 32, p. 1217, 1972.

[113] A. W. Sleight and T. A. Bither, *Inorganic Chemistry,* vol. 8, p. 566, 1969.

[114] M. Yuzuri and Y. Nakamura, *J. Phys. Soc. Japan,* vol. 19, p. 1350, 1964.

[115] D. Siebert, J. Dahlem, S. Fiechter and R. Miller, *phys. stat. sol. (b),* vol. 171, p. K93, 1992.